InSb nanostructures: growth, morphology control and transport properties

DISSERTATION

Submitted for the partial fulfillment of the requirement

for the degree of
DOCTOR OF PHILOSOPHY

by

Isha Verma

under the supervision of
Prof. Lucia Sorba

Scuola Normale Superiore di Pisa, Italy
Pisa, 2022

Abstract

Indium antimonide (InSb) offers a narrow band gap, high carrier mobility, and a small effective mass, and has attracted tremendous attention in recent years for the implementation of topological superconducting states. However, high-quality heteroepitaxial two-dimensional (2D) InSb layers are difficult to realize owing to the large lattice mismatch with other widespread semiconductor substrates. A solution to this problem is to grow free-standing single-crystalline 2D InSb nanostructures, so-called nanoflags (NFs). This contribution shows the growth of free-standing InSb NFs on InP nanowire (NW) stems using Au-assisted chemical beam epitaxy. By employing tapered NW stems and precisely orienting the substrate with the help of reflection high-energy electron diffraction (RHEED) patterns, we could maximize length and width, and minimize the thickness of the NFs. The InSb shape evolution is a result of the interplay between the axial vapor-liquid-solid growth and directional vapor-solid radial growth. By employing regular arrays of Au islands deposited on pre-patterned substrates covered with a SiO_2 mask, we could also analyze and model the growth mechanisms in detail. The optimized InSb NFs have been used to make Hall-bar devices from which we measured electron mobility of 29,500 cm^2/Vs and a mean free path of 500 nm at 4.2 K, which is the highest value reported for free-standing 2D InSb NFs in literature. We have also successfully fabricated ballistic Josephson junction devices with 10/150 nm Ti/Nb contacts that show gate-tunable proximity-induced supercurrent ($\sim$ 50 nA at 250 mK at 30 V_{bg}). The devices also show clear signatures of subharmonic gap structures, indicating phase-coherent transport in the junction and high transparency of the interfaces. Our study places InSb NFs in the spotlight as a versatile and convenient 2D platform for advanced quantum technologies.

Acknowledgments

A PhD thesis always represents the joint effort of many researchers to add some drops in the ocean of scientific knowledge. This particular work was possible by the indispensable coordinated collaboration of three research groups, so on a side, I am glad for the interaction with so many brilliant people and on the other, it means that I am indebted to all of them.

My most profound and warm acknowledgment goes to my everyday supervisor, Prof. Lucia Sorba, who taught me a plethora of things in these four years of intense work, from the experimental tools for carrying out my research, to the precious skills of efficiently interacting with other people and groups in a multidisciplinary and busy scientific environment. Her continuous encouragement, her elegance of approach to problems, her clear and open-mindedness were reference points during these years and I would not be writing this thesis without her input and support from the very beginning up to the very end.

Many thanks to Prof. Fabio Beltram, for his continuous support and his confidence in me during my PhD project.

Special thanks to Dr. Valentina Zannier, for providing me with both scientific and technical training in NW growth and characterization. From attending EuroMBE 2019 (my first conference experience) at Lenggries, Germany to organizing NW week in Pisa, Italy, I have learned a lot from her, not only academically but also a lot about Italian traditions and culture. Her creative ideas have helped me tremendously to design well-planned experiments, analyze the data accordingly and write articles clearly and concisely that completely changed and increased the impact of the publication.

This cleanroom-heavy dissertation could not have been completed if there were no Cleanroom@NEST technologists that did a great job: Dr. Daniele Ercolani and Dr. Franco Carillo, thank you for all the help to solve the practical problems related to the CBE system, lithography procedure, sputtering technology and other instrument related difficulties. I am deeply indebted to them for knowledge transfer of the fundamentals and operations. Their bright ideas played a fundamental role in the progress of this thesis.

Our work has been good to better and better to best, all thanks to our collaborators. Their valuable and constructive feedback gave fresh vision and ideas to the project. I am grateful to Dr. Francesca Rossi for the amazing TEM images and geometrical phase analysis. She has been our eyes for the nanostructure growth.

Our progress in the understanding of the complex growth mechanism of InSb NFs would not be possible without the precious insights and experience of Prof. Vladimir G. Dubrovskii. His contribution has paved a way for promising growth protocol also for future studies.

A benchmark of our work was not only to grow these InSb NFs but also to prove that they can serve in quantum technology. Thanks to Prof. Stefan Heun and Dr. Sedighe Salimian for putting my babies "InSb NFs" in the spotlight by fabricating delicate InSb-based devices and performing electrical measurements. In particular, Prof. Heun is a fun person to work with and so down to earth person. I admire him so much!

I spent these intense, but pleasant and formative, four years in the NEST laboratory and the Scuola Normale Superiore. The international, interactive environment that I encountered in both institutions was a great stimulus that opened my mind and helped me grow not only professionally, but also personally.

It is virtually impossible to mention all the colleagues with whom I interacted inside and outside of the SNS and to whom I am thankful: Elisa, Luca, Francesca (Titti), Kat, Tonio, Maria Paola, Ilir, Umesh, Rashmish, Omer, Neeraj, Francesca Telesio and many more, from SNS, my great office mates like Domenico/a, Giulia P., Simone, and the supporting Magnetotransport group at NEST, including Francesco Rosella, Valeria, and Domenic, but really, the list is much longer. It was great to spontaneously exchange so much feedback and to have so much fun with all the colleagues from NEST in these years.

Last, but not least, I cannot avoid mentioning the indirect, but crucial role of my family, my boyfriend Federico, and friends from all around the world. Their love and kindness allowed me to recover from the frequent failures and disappointments of the PhD work. I am glad to give the satisfaction for this achievement to them since they shared the experience with me and never stopped believing in me. A final, deep and special acknowledgment to my closest friends in these years: Anshika, Divyata, Nirmal, Aoife, Irene, Meghna, Rosario, Giacomo, Harpreet, Neha, Hellen, Silvio, Nadia, Alkhazur, Anjum, Aditi, Nazir and Akie. The continuous affection of the latter was a vital driving force for the intense thesis-writing times.

List of Publications

1. **<u>I. Verma</u>**, V. Zannier, F. Rossi, D. Ercolani, F. Beltram, and L. Sorba, "Morphology control of single-crystal InSb nanostructures by tuning the growth parameters," *Nanotechnology*, vol. 31, no. 38, 2020, DOI: 10.1088/1361-6528/ab9aee.

2. **<u>I. Verma</u>**, S. Salimian, V. Zannier, S. Heun, F. Rossi, D. Ercolani, F. Beltram, and L. Sorba, "High-Mobility Free-Standing InSb Nanoflags Grown on InP Nanowire Stems for Quantum Devices," *ACS Appl. Nano Mater.*, vol. 4, no. 6, pp. 5825–5833, 2021, DOI: 10.1021/acsanm.1c00734.

3. S. Salimian, M. Carrega, **<u>I. Verma</u>**, V. Zannier, M. P. Nowak, F. Beltram, L. Sorba and S. Heun, "Gate-controlled supercurrent in ballistic InSb nanoflag Josephson junctions," *Appl. Phys. Lett.*, vol. 119, no. 21, 2021, DOI: 10.1063/5.0071218.

4. **<u>I. Verma</u>**, V. Zannier, V. G. Dubrovskii, F. Beltram, and L. Sorba, "Growth modeling of InSb nanoflags synthesized in regular arrays by chemical beam epitaxy," submitted to MDPI Nanomaterials.

Contents

Introduction

Background

Electronics has become an integral part of our daily lives. It has radically changed how we communicate and access information. This explosive growth has largely been fueled by the high performance, low cost, and small form factor of the underlying integrated circuits.

In 1965, Gordon Moore, one of the founders of Intel, forecast an exponential growth in the number of components per integrated circuit (Moore's law), which was realized by decreasing device size. As an implication, the number of components in an integrated circuit (IC) had doubled every year since the invention of the IC, and this trend was predicted to continue for at least ten years [1]. For decades, this scaling of classical semiconductor technologies based on complementary metal-oxide semiconductor (CMOS) devices has led to an exponential growth of computing power on a chip. But as we scale down these devices further, more elaborate fabrication methods with increasing complexity, increment of tunneling and leakage currents, larger power consumption, and higher thermal dissipation are observed, increasing the cost and time needed for the fabrication of higher-density chips. Therefore, to keep Moore's trend on the roadmap, new device architectures and materials are being exploited, which are usually termed revolutionary CMOS or "beyond-CMOS" technologies. Some of the examples of beyond-CMOS devices include carbon-based nanoelectronics, spin-based devices, ferromagnetic logic, atomic switches, nanoelectromechanical switches (NEMS), etc. Figure 0.1 shows the official technology roadmap, which was originally established in the early 1970s, as the semiconductor industries began to scale down the transistors [2]. But these devices might result in one or two generations of smaller transistors and then Moore's law "hits the wall".
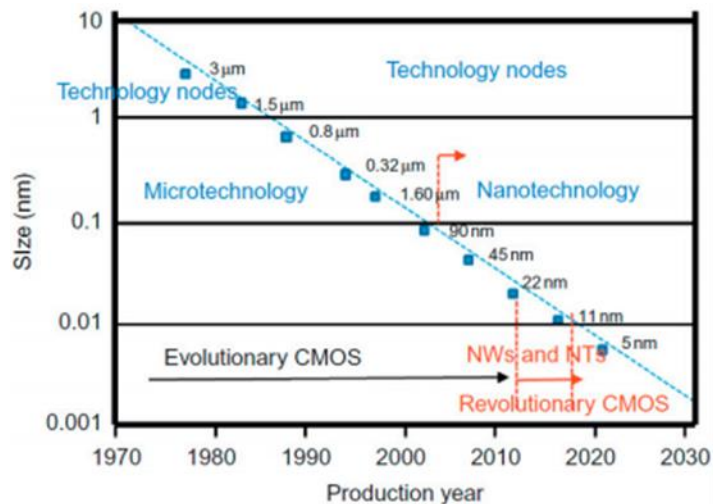

Figure 0.1: Miniaturization of the transistor gate length in different technology nodes and production years.

Nevertheless, beyond-CMOS technology has presented potential solutions for future logic and memory devices, front end processing, interconnects, assembly and package, lithography, metrology, and life-cycle assessment of Environment, Safety, and Health (ESH)-related issues [3]. But there are still some problems that cannot be solved efficiently by classical computing, as the famous example of factorization of large composite integers. The computational effort grows exponentially with the size of the integer to be factored. Other problems include precise molecular simulations, optimization problems (problems that tackle finding the best solution from all feasible solutions), and searching through big databases. The solution to these problems will require a fundamentally different approach, a new information process technology in the field of computing, called quantum computing.

The pioneering work on quantum computers was originated in 1979 by Paul Benioff and in 1982 by Richard Feynmann [4, 5], which attracted huge amounts of attention. Corporations including Microsoft, Google, IBM, Intel, DWave, IonQ, Baidu, Tencent, Alibaba, and many more, are developing different quantum technologies based on semiconductor-based platforms, superconducting circuits, adiabatic spin states of the coupled single-electron quantum dot, and single atoms in ion traps [6-13]. The first and strongest example of the out-performance of quantum computers was found in 1994 by Peter Shor from MIT. On a quantum computer, to factor an integer N, Shor's algorithm runs in polynomial time, meaning the time taken is polynomial in log N, compared with the most efficient algorithm on classical computers that can do the same job only exponentially in time. The second major quantum algorithm was discovered in 1996 by Lov Grover from Bell Labs [14]. He designed a quantum algorithm for searching through big databases. When searching through a database with a million entries, a classical computer checking it one by one would get an answer on average in 500,000 trials. Lov Grover showed that on a quantum computer, one would, on average, need only about 1,000 trials (quantum parallelism). Quantum systems are hard to model on classical computers, while they would be very natural for quantum computers. Quantum modeling includes simulations of particles in large accelerators or modeling chemical reactions. Besides uses for fundamental science research, molecular simulations would be very applicable for drug development. Quantum computing is believed to be the key to tackling important challenges of the 21st century by being complementary to classical computing. Even though quantum computers are still mostly laboratory experiments, we should never forget that just five decades ago a computer was the size of a full room, an unprecedented 1 trillion-fold increase in computing power is embodied in the typical 6-inch smartphone [15].

Quantum computing

A classical computer uses transistors that can be turned on or off, representing either |0> or |1>. A quantum computer employs the principles of quantum physics to create a system where |0> and |1> are represented by two states of a quantum mechanical system. These states, the quantum bit (qubit), serve as a building block of a quantum computer harnessing the laws of quantum mechanics enabling the massive parallelism of quantum algorithms. It is possible to

put quantum bits or qubits, in a superposition that can be represented not only by |0> or |1>, but also intermediate (as shown in figure 0.2). This superposition state can be combined with another quantum mechanical effect, entanglement, in which two entangled particles are affected by each other's state and operations on it, even if the particles are spatially separated. When employed on qubits the amount of entangled space grows exponentially with the number of qubits, in turn exponentially increasing the computational power of the system.
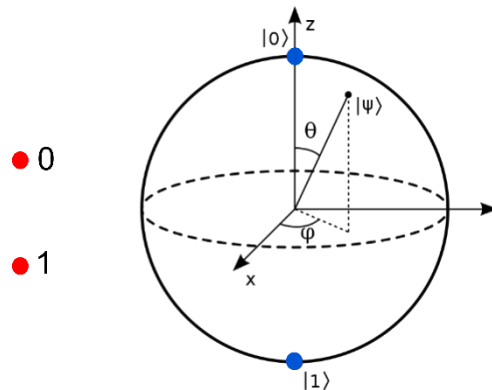
Figure 0.2: Representation of a classical bit on the left (in red) and a qubit (Bloch sphere) on the right.

Any system with two possible quantum mechanical states such as the oscillations in a superconducting loop or energy levels of an ion-could form a qubit. The biggest hindrances to the realization of a working quantum computer are noise and decoherence [16- 18].

Decoherence arises from undesired interactions between the qubits and the environment. Light, sound, vibrations, heat, etc., as well as the act of measuring the qubit, the readout, can all be affected by decoherence. Because of decoherence, qubits are fragile and their ability to remain in superposition or entanglement is compromised. Decoherence leads to multiple errors in the process of quantum computation resulting in information loss. To allow for successful quantum computation, the qubit must be robust and have enough coherence time to run and evolve a calculation of quantum states.

Trapped ion qubit platforms [19] have been a promising technology, in particular in terms of the quality of the qubits (with two-qubit gate errors of 10^{-3}). However, they are limited in scalability and by their relatively slow, μs-scale gate times. In the last years, superconducting qubits [20] underwent a tremendous evolution and are currently at the forefront of industrial efforts. However, they yield shorter characteristic coherence times since collective degrees of freedom are coupled to the environment more effectively. Another viable platform constitutes spins in semiconductor quantum dots [21]. While this platform typically enables qubits with long coherence times, this also comes at the expense of more challenging state readout, weaker qubit-qubit coupling, and slow multi-qubit gates.

Scope and outline of this thesis

Today a great interest revolves around the possibility to create and manipulate new states of matter with topological properties. This stems mostly from the intrinsic robustness of topological states against local perturbation and the ensuing relevance for quantum computing architectures [22, 23]. However, most physical systems have only local degrees of freedom that are sensitive to local perturbations. Hybrid superconductor-semiconductor heterostructures represent a promising platform in which topological properties can emerge [18, 24-26]. Of course, parameters like crystal quality of the semiconductor, superconductor-semiconductor interface, choice of materials, and thickness of contacts are very crucial for high-performing quantum devices. In this context, the main objective of this thesis is to provide a potential quantum system, which is 2D free-standing indium antimonide (InSb) nanostructures, for topological superconductivity. New strategies are developed with the required appropriate choice of growth parameters to realize these 2D InSb nanostructures, called InSb NFs, in a catalyst-assisted growth regime. The growth is performed by chemical beam epitaxy (CBE) on InAs(111)B and InP(111)B substrates and the growth mechanisms are studied by tuning the growth parameters and conditions. Detailed morphological, structural, and evaluation of the electrical properties have been performed.

The thesis is outlined as follows:

Chapter 1: This chapter reviews the different bottom-up growth mechanisms of nanowires (NWs) relevant to the thesis. The materials of choice are listed with the suitable requirement for high-performance quantum devices.

Chapter 2: The sample preparation, growth technique, and characterization techniques used for the experiments within this thesis are introduced in this chapter.

Chapter 3: The growth of InSb nanostructures on InAs NW stems is reported. The growth parameter dependence and crystal structure of these nanostructures, specifically 2D InSb NFs are studied.

Chapter 4: The objective of this chapter is to demonstrate the growth of larger InSb NF by carefully choosing a robust supportive stem, tapered InP NWs, and aligning the samples with the aid of reflection high-energy electron diffraction (RHEED). Furthermore, electronic transport of NFs is studied to extract carrier mobility, density and electron mean free path. We report the highest value of carrier mobility for free-standing 2D InSb NFs in literature.

Chapter 5: In this chapter, the growth modeling of 2D InSb NF grown on lithographically patterned substrates with a combined selective area (SA) and vapor-liquid-solid (VLS) growth is discussed. This gives an in-depth understanding of the growth mechanism and shapes the evolution of InSb NFs, which is crucial for the desired device properties and scalability.

Chapter 6: Electronic transport of ballistic Josephson junction devices with Ti/Nb contacts are explored. We show gate-tunable proximity-induced supercurrent and signatures of subharmonic gap structures, indicating phase-coherent transport in the junction and high transparency of the interfaces. Our study places InSb NFs in the spotlight as a versatile and convenient 2D platform for advanced quantum technologies.

Finally, a **summary** of the achieved results together with an **outlook for future work**.

Chapter 1: Nanowire growth mechanisms

Low-dimensional III-V materials, because of their superior properties as size effects, and large surface to bulk ratio, have a wide range of applications in electronics and optoelectronics, such as lasing, sensing, logic, and detection [27-29]. InSb nanostructures have attracted tremendous interest due to their high electron mobility, narrow bandgap, and small electron effective mass among III-V materials.

To develop nanostructure-based devices with high performance, it is necessary to precisely control the nanostructures, especially the crystal quality and structural properties, growth direction, and morphology. A variety of methods have been developed in the last decade to engineer nanostructures by tuning growth parameters [30-33]. This chapter introduces the relevant methods of III-V nanostructure growth. The materials of choice are listed with the requirements for a high-performance quantum device.

1.1 Nanostructure growth mechanisms

The synthesis of III-V nanostructures can be accomplished in two main ways: "Bottom-up" and "Top-down" approaches [34]. "Top-down" methods involve etching bulk materials to create low-dimensional structures. From a bulk substrate, various lithography and etching steps are used to carve out the designed structures. Despite its development, there have been problems with its resolution and crystal quality. Conversely, "Bottom-up" is a fabrication method in which atoms and molecules are used to build up the desired nanostructures with few defects, homogeneous chemical compositions, and a large aspect ratio. Different concepts refer to the bottom-up fabrication of nanomaterials, most applied ones are metal-catalyst assisted VLS and vapor-solid-solid (VSS), SA growth, and the cleave edge overgrowth (CEO). For the synthesis of crystalline nanomaterials, different epitaxial growth methods, such as chemical vapor deposition (CVD), metal-organic vapor phase epitaxy (MOVPE), CBE, molecular beam epitaxy (MBE), etc., are employed. CBE is used in this study to grow bottom-up nanostructures. The samples discussed within this thesis are catalyst-assisted grown III-V nanostructures.

1.1.1 Vapor-liquid-solid mechanism

In the 1960s, Wagner et al. [35] proposed the VLS mechanism to describe Si whiskers or NW growth, which was induced in the gas phase with liquid gold droplets on a silicon substrate. The VLS mechanism is widely accepted as a basis for explaining various 1D growths. The following steps describe the general process of VLS driven growth: (1) Liquid droplets form and collect gas-phase molecules when growth temperature is higher than eutectic temperature; (2) After absorbing reactant into the catalysts, they become supersaturated; (3) With the continuous supply of reactant, crystals grow at the liquid/solid interfaces, leading to nanostructure growth. According to the conventional VLS growth theory, the growth temperature should be high enough to ensure that the alloy particles are in a liquid state. The

supersaturation (decided by the chemical potential difference between solid nanostructures and liquid droplets) is the dominant driving force in the oriented NW growth. NW diameter is determined by the catalyst size. These samples were all grown with gold (Au) catalyst. The schematic diagram of the VLS growth mechanism is shown in figure 1.1.
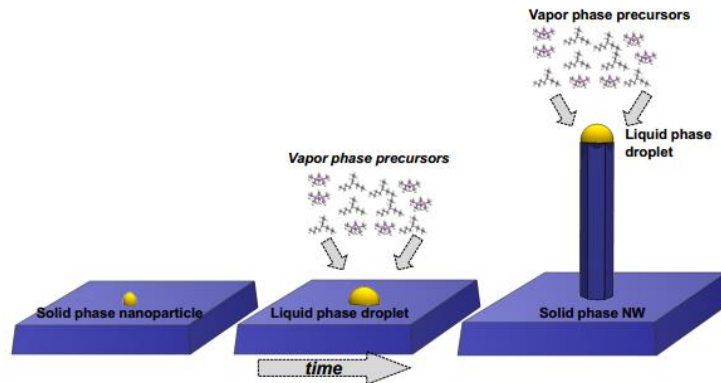
Figure 1.1: Scheme of VLS growth mechanism.

During catalyst-assisted growth of III-V NWs, the vapor phase of group-III and group-V precursors serves as the suppliers and the alloy droplets serve as the collectors [36]. Because the group-V materials have a short diffusion length on the surface [37], they contribute primarily through direct impingement on the catalyst droplets to the growth of NWs. In CBE, NWs are generally grown under group-V-rich conditions. As a result, the group-V molecules adsorbing on the substrate surface only contribute to the planar 2D growth and rarely limit the axial growth of NWs. In particular, it has been demonstrated that As is insoluble in Au [38] and several post-growth measurements proved that no As is observed in the particles [39, 40]. On the contrary, the group-III molecules usually have long diffusion lengths and are present in the NPs.
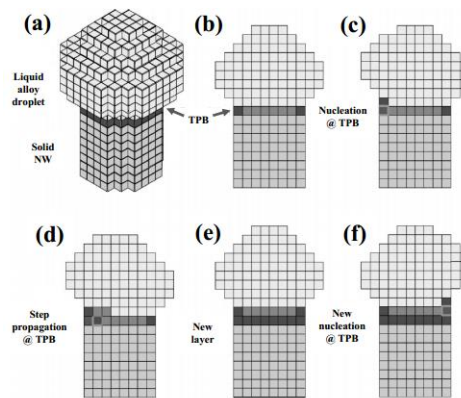
Figure 1.2: Illustration of preferential interface nucleation, birth, and spread the growth of a NW. (a) 3D depiction of a NW illustrating the TPB as a dark line on the circumference of the droplet/NW interface. (b) Cross-section of the wire depicted in (a). (c) Nucleation of a new layer at the TPB with the TPB being displaced in the growth direction. (d) Step

propagation at the droplet/NW interface. (e) A new layer is completely formed. (f) Nucleation at a different site.

Wacaser et al. developed a model of preferential interface nucleation to explain catalyst-assisted NW growth. This model has completed the general VLS theory [36] in the sense of explaining why the crystal prefers to grow along 1D instead of planar growth (2D). Calculating the energy barriers for nuclei located at different sites, the researchers found that the energy barrier is smallest when nucleation occurs at the three-phase boundary (TPB). The TPB is the boundary between vapor, liquid, and solid phases. So, the nucleation is more likely at the TPB than at the substrate, which leads to the growth of NWs. Once nucleation occurs, a monolayer rapidly spreads to cover the entire liquid/solid interface, forming a new layer of the NW. Another nucleation occurs at the TPB after these processes, and then a new monolayer is formed. The crystal will grow in a 1D fashion as long as this process is repeated. The illustration of preferential interface nucleation, birth, and spread growth of a NW is shown in figure 1.2.

1.1.2 Selective area growth mechanism

Although crystals prefer to grow in 1D rather than planar growth on the substrate, parasitic growth in the VLS mechanism is inevitable. The growth of III-V crystals can be restricted to the unmasked areas of a substrate by partially masking it with dielectrics such as SiO_2 or SiN_X. The selective area epitaxy (SAE) is the most obvious aspect of surface selective growth in the metalorganic deposition system [41] and is the basis for applications in III-V device structures using lateral material modulation or structural quenching. When one transitions from growth to non-growth areas, a new set of transition facets is formed. These higher index planes exhibit different growth kinetics due to individual equilibrium conditions and molecule surface diffusion [41]. Moreover, the gradient of molecule concentration between these crystal facets determine surface communication, and therefore the growth rate and composition of the surface. Another crucial point is the lateral modulation of growth to non-growth that causes disturbed gas phase diffusion and adsorption flux shadowing. The schematic of SAE growth is shown in figure 1.3.
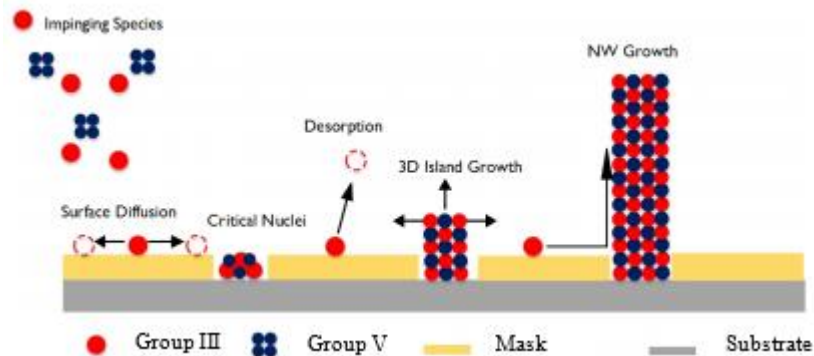

Figure 1.3: Illustration of SAE growth of NWs.

Combining SAE growth with the VLS mechanism, we analyze the shape evolution of Au-catalyzed InSb NFs on regular arrays of InP NWs grown on lithographically patterned InP(111)B substrates described in chapter 5. Chapter 2 describes in detail how the substrates are prepared.

1.2 Materials

The proximitized semiconductor channel is the core of a topological quantum device. According to Lutchyn et al. [42] and Oreg et al. [43], semiconductor channels must meet strict material requirements. In particular: a semiconductor with strong Rashba spin-orbit interactions with proximity-induced superconductivity placed in a magnetic field. A defect-free crystalline phase is also preferred for coherent and ballistic transport in most quantum devices. In the end, the ability to fabricate and synthesize nanomaterials with the desired size, thickness, composition, crystal phase, etc., is crucial to accessing the unique electronic and quantum properties of these nanomaterials. In this regard, the heavy-element semiconductors InAs and InSb have received extensive attention due to their material properties with strong spin-orbit coupling and large Landé g-factor [44]. Throughout this thesis, the focus is on the growth of InSb nanostructures and Nb/Ti-InSb quantum devices.

1.2.1 InSb for quantum technologies

InSb has a narrow bandgap ($\sim$ 0.23 eV) [26, 45, 46]. It also has a very high bulk electron mobility (7.7×10^4 cm^2/ (Vs)) [47, 48] and a small effective mass (m* = 0.018 me) [46, 47, 48-52] which are both important requirements for high-speed and low-power electronic devices [48, 53]. Finally, it also exhibits a strong spin-orbit interaction and a large Landé g-factor (|g*| $\sim$ 50) [47, 52] and thus it is useful for spintronics applications [46, 53]. The InSb hybrid system has attracted tremendous attention in recent years, both theoretically [16, 17] and experimentally [54-57], for the implementation of topological superconducting states supporting Majorana zero modes (MZMs) which have triggered strong efforts to improve the quality of these hybrid systems [57-64]. The effective development of InSb-based devices has been hindered because of a large lattice mismatch between InSb and other widespread semiconductor systems, as shown in figure 1.4. The growth of high-quality heteroepitaxial 2D InSb layers becomes complicated and demands stacks of buffer layers.

On the other hand, thanks to the capability of NWs to efficiently relax elastic strain along the sidewalls when lattice-mismatched semiconductor systems are integrated, one can grow free-standing InSb nanostructures free from structural defects on NW stems of mismatched materials [66, 67]. In particular, high-quality InSb NWs have opened new research arenas in quantum transport, since their geometry leads to carrier confinement and their electron energy levels are electrostatically tunable. However, the challenge remains as NW morphology does not provide enough flexibility to fabricate multi-contact Hall-bar devices. An alternative geometry that would allow a high degree of freedom in device fabrication and allow exploring new material properties is represented by 2D InSb nanostructures on NW stems.
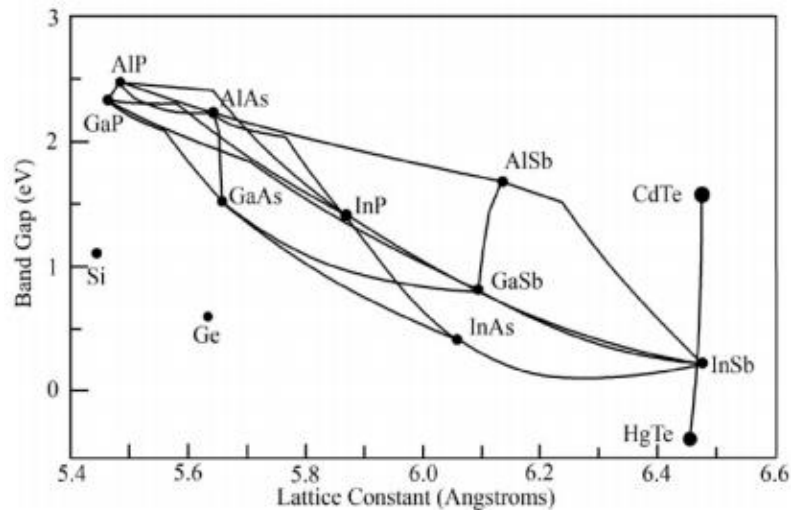
Figure 1.4: Band gap plotted against lattice constant for common semiconductor materials [65].

Nevertheless, controlling the aspect ratio of free-standing InSb nanostructures is challenging, due to the low vapor pressure of Sb and the surfactant effect [68]. In general, the narrower growth window of III−Sb in comparison to other III−Vs (III−P and III−As) is due to the surfactant effect of Sb atoms, as the atoms tend to segregate to the surface, thereby modifying the surface energy [68, 69]. For this reason, it is essential to investigate the growth mechanisms and the morphology of InSb free-standing nanostructures. In this thesis, we will address morphology control and electrical characterization of Au-catalyzed InSb nanostructures using Au-assisted CBE.

1.2.2 Superconductor

Several experimental routes with the universal goal to reduce the superconductor-semiconductor interface disorder are explored [56, 57, 61, 69, 70]. As a first consideration, the film should remain thin enough to withstand high parallel magnetic fields, as well as uniform along with and across the NW to ensure long coherence length, and disorder-free interfaces. Secondly, superconductor materials that are compatible with standard fabrication techniques are favored.

In addition, material science dictates consideration of the following requirements and uncertainties:

- The thickness of a superconducting thin film should be uniform.
- Thin films of superconducting materials should not oxidize within a short period (typical fabrication time); a suitable capping layer should be utilized.

- A superconducting material whose lattice constant value is close to that of InSb is desirable. Strain from the superconductor should not lead to changes in the electronic band structure.

- Superconductors should be able to withstand the typical device processing temperatures (~100 - 200 °C).

To fabricate quantum devices, Ti/Nb superconducting contacts are sputtered ex-situ on an InSb nanostructure, and the electrical characterization is discussed in chapter 6.

Chapter 2: Experimental methods

A significant part of my experimental work consisted in the design and patterning of substrates before the epitaxial growth. The correct implementation and optimization of reproducible fabrication protocols are the key to a successful outcome of semiconductor growth and the observation of subtle and fundamental physics phenomena.

The protocols used in this work start with the colloidal dispersion method to seed NW growth on the substrate of choice, in this case, InAs(111)B and InP(111)B. The other growth approach, i.e. SAE, requires meticulous substrate preparation and consists mostly of a combination of lithography, etching, and thin film deposition. I will briefly describe the working principle of each fabrication process and the corresponding equipment used.

Semiconductor nanostructure growth involves the use of epitaxy to provide uniformity in composition, controlled growth parameters, and a better understanding of the growth itself. CBE has been employed for the growth of semiconductors in this work. *In-situ* and *ex-situ* characterization techniques are also fundamental methods to acquire information on the samples. I will briefly list the main tools used for the morphological, structural, and electric investigation of the as-grown semiconductor nanostructures. Namely, RHEED, scanning electron microscopy (SEM), transmission electron microscopy (TEM), geometrical phase analysis (GPA), device fabrication, cryostat for low-temperature measurements, and electronic devices for electrical measurement are described in this chapter.

2.1 Substrate preparation

2.1.1 Colloidal dispersion

The seeding of NW growth on InAs(111)B and InP(111)B substrates has been achieved by colloidal dispersion. Using this method, a 0.1% Poly-l-lysine solution is drop cast onto the substrate for 30 seconds, then rinsed with deionized (DI) water and dried. Using poly-L-lysine as a pre-treatment of the substrate surface prevents agglomeration due to Van der Waals forces and other surface interactions while the poly-L-lysine molecules adhere to net negative charges on the surface of colloidal nanoparticles (NPs). Skipping the pre-treatment step leads to extremely low densities of Au NPs and not reproducible NP deposition. A commercially available Au colloidal solution of nanoparticles with 30 nm in diameter was then dispersed onto the substrate for a few seconds, followed by rinsing in DI water and blow-drying. The latter step is repeated until the desired density of Au NPs is achieved. The plot in Figure 2.1 shows the effect on Au NP density when the Au drop-casting step is repeated. We found (6 ± 2) μm^{-2} to be the most preferred density for our experiments.
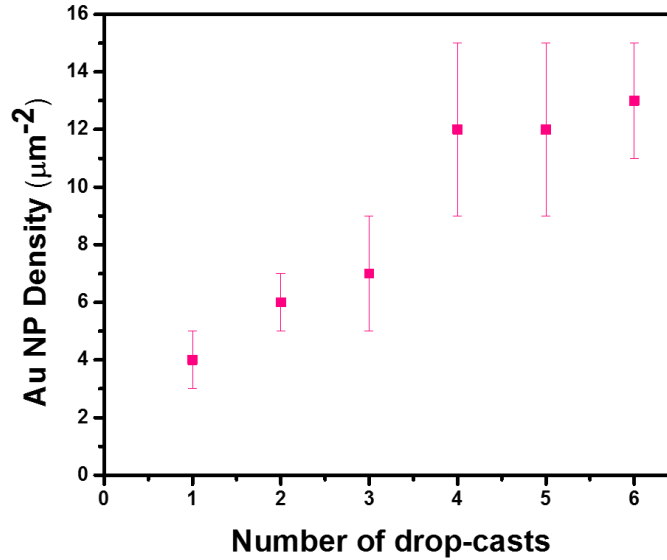
Figure 2.1: Plot of Au nanoparticle density versus several drop-casts.

2.1.2 Lithographically defined Au disc arrays

A technique widely employed to realize NWs with highly controlled position and dimension is lithography, which is, the transfer of the desired pattern on a substrate [71]. Typically, the pattern information is recorded in a thin film of an energy-sensitive polymer called resist. The solution containing the resist is uniformly spin-coated on the clean substrate and then selectively exposed to an energy pattern, consisting of a focused beam of electrons for electron-beam lithography (EBL). The development of the resist film into some specific solution selectively removes either the exposed or the unexposed areas, according to whether the employed resist is a positive or negative one, respectively. The remaining pattern is usually used as a mask for the following processing, consisting of etching and lift-off deposition as schematically demonstrated in Figure 2.2(a-g). For fabrication of InP(111)B substrates for SAE growth, the substrates were covered with 20 nm-thick sputtered SiO_2 film. The SiO_2 film acts as a mask and prohibits parasitic growth on the underlying substrate. The InP substrate was transferred to a radiofrequency (RF) magnetron sputtering unit and pumped for 1 hour to obtain a chamber pressure of 9×10^{-6} Torr. Argon gas was used to obtain ionized energetic particles with an Argon (Ar) flow of 25 sccm (standard cubic centimeter per minute). The sputtering process is controlled by mainly two parameters, RF sputtering power and deposition time. The RF power of 150 Watt for 66 sec was optimized to achieve 20 nm-thick SiO_2 film. A schematic diagram of the RF magnetron sputtering system is shown in Figure 2.3(a).

The substrates used for EBL in this thesis are always cleaned by acetone and isopropanol and with pre-baking at 120°C for 10 min before spin coating. The e-beam resist used is a positive working resists AR-P 679.02 manufactured by ALLRESIST. It is ethyl lactate dissolved poly-methyl-meth-acrylate (PMMA) with a molecular weight of 950K. After spin-coating the substrate with a speed of 5000 rpm (rotations per minute), the resist will uniformly cover the

surface of the substrate with a thickness between 200 and 300 nm. After the sample is baked at 120°C for 15 min to remove the solvent, it is ready to be transferred into the electron-beam system.
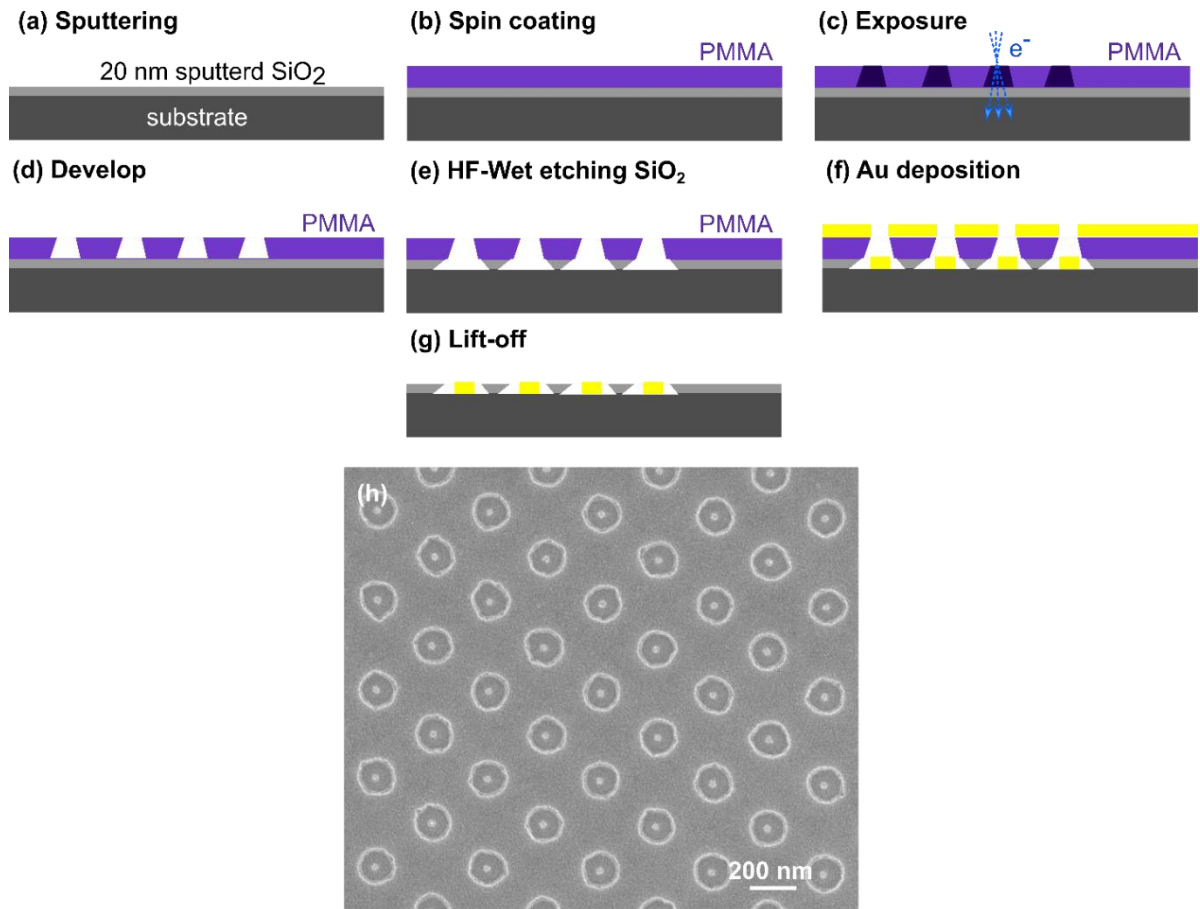
Figure 2.2: (a-g) Sketch of the steps employed for the realization of nanoparticles with the EBL procedure. (h) The resulting ready-for-growth substrate after following a-g steps.

The resist is exposed by a focused beam of energetic electrons (20 keV), enabling a feature resolution down to a few tens of nm, and the pattern can be edited through a computer-aided design (CAD) file, providing full design freedom. The lithographic system unblanks the electron beam in correspondence to the areas of the CAD pattern to be exposed and blanks (blocks) it in the rest of the surface. In this work, EBL was used for patterning the array of nucleation sites for NW growth. The electron-beam system used in this work was based on the Gemini electron optics columns from Zeiss, namely UltraPlus. A schematic design of the complex electron optics of these systems is shown in Figure 2.3(b). The UltraPlus model is supplied with a motorized stage, whose position is monitored by laser interferometry and can be controlled with nm precision. The system was integrated with Raith's Elphy hardware (Multibeam for the UltraPlus columns), mainly consisting in the beam blanking system, sample

stage control system, a picoammeter measuring the beam flux, and the user interface hardware and software used to align the stage, the sample and the electron beam, as well as to translate the input CAD pattern.

The minimum time to expose a fixed area for a fixed dose is given by the following formula:

$$D{\cdot}A \ = \ T{\cdot}I \qquad\qquad (2.1)$$

where T is the time to expose the object (can be divided into exposure time (s) /step size (nm)), I is the beam current, D is the dose, and A is the exposed area. In this thesis, the exposure was always carried out with an acceleration voltage of 20 kV and a probe current of 19 ± 2 pA. Both the exposed area and the dose can be controlled from the Multibeam software as a CAD drawing, while the software will calculate the exposure time and feed it to the machine.
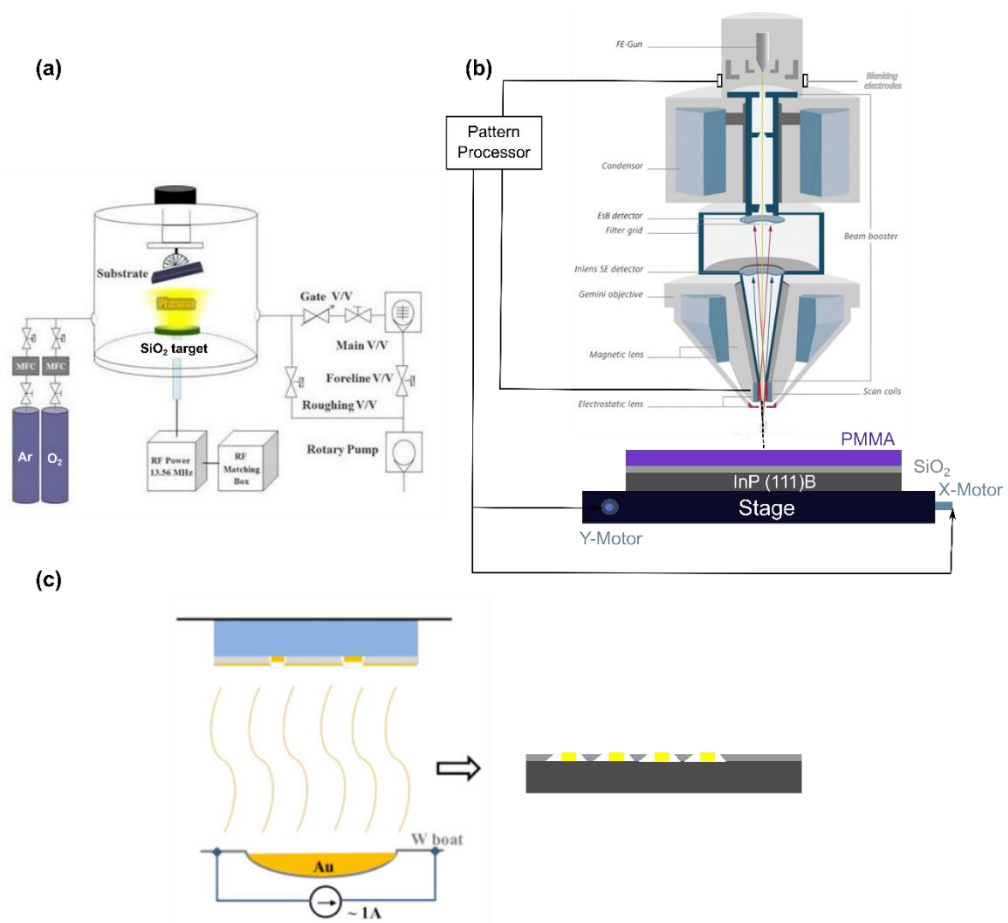
Figure 2.3: (a) Schematic diagram of RF magnetron sputtering system. (b) Schematic design illustrating the working principle of EBL: the pattern contained in the CAD file controls the displacements of the sample stage, the deflection of the electron beam, and the beam blanking so that the resist is exposed to electrons according to the desired pattern. An example of a thermal evaporation process, typically used for metal depositions, is shown in (c).

After exposing the resist, the exposed area will be selectively removed by the developer. The temperature of the developer and the development time are the parameters to be optimized. Slight changes of these two parameters will modify the profile of the resist and significantly change the result of lithography. For example, longer development times or developing the exposed pattern at higher temperatures will lead to an enlargement of the defined pattern. A similar effect will be obtained by increasing the dose during exposure. An optimal development should lead to open holes with undercut profiles in exposed PMMA, as shown in Figure 2.2. The developed samples are then transferred into the Diener plasma asher, which decomposes organic residuals of the resist, whose ashes are pumped away. It consists of two parallel plates, where the samples are maintained in the lower plate, whereas the charged oxygen species generated by the RF radiation are accelerated towards the upper plate. Therefore, the plasma species do not drift towards the sample surface and the cleaning effect is based on the diffusion of the reactive neutral species along the sample surface. This fact makes ashing quite suitable for cleaning delicate substrates.

Further, the developed and oxygen plasma-treated substrates are wet etch in buffered hydrofluoric acid (HF) solution for 4 min to selectively remove the oxide mask and rinsed in deionized water for 1 min. This step produces hole openings of (153 ± 7) nm in the SiO_2 film. The next step is the metal deposition, for which Kurt J. Lesker thermal evaporator was employed, whose schematic design is shown in Fig. 2.3(c). It consists of a high-vacuum chamber (10^{-6} Torr) with different metal sources, a quartz crystal thickness monitor for evaporation rate, and film thickness feedback. A small amount of 99.9% pure Au metal wire was placed on a conductive tungsten resistive boat located in a high vacuum chamber. The substrate, covered with a patterned resist mask, is placed on the substrate holder and the Au in the tungsten resistive boat is Joule-heated until it reaches the evaporation point; the vapors travel ballistically to the substrate surface, where a thin film is deposited. With the high precision mass measurement provided by the quartz balance, the Au mass per unit area is controllable to much more than a monolayer average thickness, providing good control for the amount of gold evaporated on the samples. The nominal Au thickness employed is 6 nm, which was chosen after the growth feedback. The application of a resist remover will lift off the metal which is on top of the resist while leaving the metal that is in direct contact with the substrate. The successful outcome of the process critically relies on the presence of an undercut in the profile of the patterned resist. For EBL patterned positive resists, such as PMMA, the backscattering of electrons from the substrate results in a greater exposure at the bottom of the resist film than at the top, thus yielding a natural undercut profile after the development. The resulting ready-for-growth substrate is shown in Figure 2.2(h). The resulting Au discs are (30 ± 3) nm in diameter with a film thickness of 6 nm.

2.2 Growth technique

2.2.1 Chemical beam epitaxy

CBE is an epitaxial technique to grow high-quality materials in an ultra-high vacuum (UHV) environment [72]. This technique was first developed at the Bell Labs in the early 80s to realize the epitaxial growth of InP and GaAs films and their related compounds [73]. It is a hybrid technique combining MOCVD and MBE that utilizes the advantage of both techniques. Similar to MOCVD, the precursors used in the CBE system are metal-organics (MO) but without carrier gas [74]. Using tertiary-butyl phosphine (TBP), tertiarybutylarsine (TBAs) as group-V precursors in the CBE system, results in more stable beam fluxes with respect to MOCVD and better control of the As/P ratio than MBE. Additionally, the use of MO sources of group-III materials is motivated by their long-term stability and easy handling when changing sources. Due to its slow growth rate, CBE is the proper technique when some particular requirements are needed, such as control of interfaces abruptness and doping profiles. Furthermore, in the CBE system as in MBE, the growth is always carried out inside a UHV environment. At such low pressures, the mean free path L of a molecule is given by:

$$L = \frac{K_B T}{\sqrt{2}\pi d^2 p} \qquad (2.2)$$

where K_B is the Boltzmann constant, T is the temperature, p is pressure, and d is the diameter of the gas particles. Thanks to the UHV environment, L in a CBE system is of the order of 10^5 meters. Therefore, molecular transport occurs ballistically. Another advantage of the use of the UHV chamber is its compatibility with electron diffraction probes such as RHEED, which can provide fundamental *in situ* information on growth mechanism and crystal structure [75]. The CBE technique has a growth rate comparable to MBE and similar wafer capability. Such characteristics allow to carry out high-quality and uniformly epitaxial growth on wafers with a large area.

The CBE system employed in this thesis is a Riber Compact-21 located at NEST Laboratory of Scuola Normale Superiore in Pisa (Italy). The schematics of the system are shown in Figure 2.4. A UHV stainless-steel growth chamber is kept pumped with a turbo pump and an ion pump providing a base pressure of 10^{-10} mbar. During the growth, only turbo pump employed and the pressure is $10^{-6} - 10^{-5}$ mbar, strongly due to the group-V precursors. A platen manipulator allows the use of one single wafer (up to 3 inches in diameter), and it is capable of continuous rotation (up to 60 rpm) while heating up to 700°C. Additionally, the inside walls of the growth chamber are surrounded by a cryo panel filled with liquid nitrogen as shown in Figure 2.4, which allows reducing the background pressure. Moreover, the cryo panel ensures that all the stainless-steel parts of the CBE chamber are cold during the growth to avoid the so-called "memory effect" when switching materials. The growth chamber is connected to a preparation chamber, which is pumped by an ion pump. The substrates are degassed before the growth

inside the preparation chamber to remove moisture from the substrate surface. There is a load-lock module, connected to the preparation chamber, which is pumped by a small turbo pump to transfer the sample from air into the system.
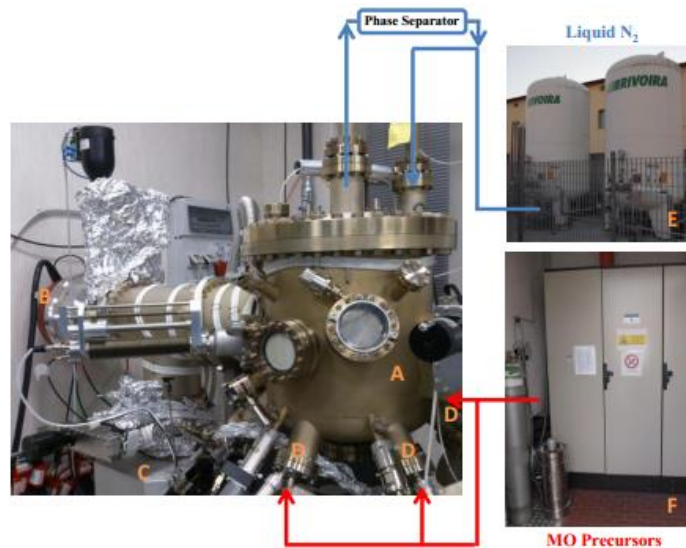
Figure 2.4: Picture of the Riber Compact 21 CBE system. A: Growth chamber; B: Turbo pump; C: Ion pump; D: Precursor injectors; E: liquid nitrogen vessels, and F: gas cabinet.

All UHV components can resist a bake-out temperature of 200°C which is necessary to remove the water condensation from the walls and the cryo panels inside the growth chamber after closing the system.
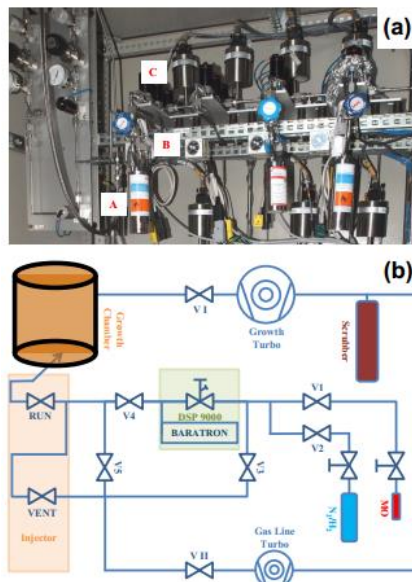
Figure 2.5: (a) Photograph of the MO cabinet including A: MO cylinder; B: Heater; C: Baratron. (b) Schematic drawing of the precursor gas line.

Our CBE system contains the following MO precursors for group III: trimethylindium (TMIn), triethylgallium (TEGa), and trimethylaluminum (TMAl), and for group V: TBAs, TBP, trimethylantimony (TMSb), and tris(dimethylamino)antimony (TDMASb). The ditertiarybutyl selenide (DtBSe) precursor is used as a source for n-type doping. The MO sources are stored in stainless-steel bottles with individual heaters in the gas cabinet room, as shown in Figure 2.5(a). The environmental temperature of the gas cabinet is kept at around 30°C. Before the precursors enter into the gas lines, they pass a needle valve and a Baratron manometer. The measured pressure is fed back to the pressure control unit which can regulate the needle valve. A schematic sketch of the gas lines is shown in Figure 2.5(b). These precursors are carried from bottles to the gas injectors through dedicated gas lines as the gas lines are connected to the growth chamber and pumped by a turbo pump, see Figure 2.5(b). The MOs are fed into the growth chamber via line injectors: two low temperature (LT) and two high temperature (HT) gas injectors.

In the HT injector, a hot filament is mounted to reach about 1000°C, mainly for thermal pre-cracking of TBAs, TMSb, and TBP, while the other MO precursors are injected directly into the growth chamber and cracked on the hot substrate surface due to thermal pyrolysis. As a most important growth parameter, the substrate temperature is measured by a thermocouple and an external pyrometer with an accuracy of ± 5°C.

The Fluke- Endurance^{TM} series pyrometer is a 2-Color (ratio) infrared non-contact temperature measurement system with variable focus, through-the-lens sighting, and parallax-free optics. It is an energy transducer designed to measure accurately and repeatedly the amount of heat energy emitted from an object, and then convert that energy into a measurable electrical signal. The temperatures are determined from the ratio of two separate and overlapping infrared bands and it is the optimal instrument for measuring the temperature of targets that are partially obscured (either intermittently or permanently) by other objects, openings, screens, or viewing windows that reduce energy. Another benefit is that the 2-color sensor measures closer to the highest temperature within the measured spot (spatial peak picking) instead of an average temperature, provided the background is much cooler than the target. A 2-color sensor can be mounted farther away, even if the target does not fill the resulting spot size. The convenience is that one is not forced to install the sensor at some specific distance based upon target size and the sensor's optical resolution.

2.3 Crystal quality and morphological characterization

2.3.1 Reflection High-Energy Electron Diffraction (RHEED)

RHEED is an in situ technique used to analyze surface crystal structure at atomic scales and to monitor the growth of thin films. It uses a finely collimated electron beam with 10–100 kV energy. The beam irradiates a sample surface with grazing incidence to obtain forward scattered diffraction patterns [76-78]. Thanks to its rapid feedback and the capability of providing crystal structure information, RHEED is a powerful *in situ* characterization tool employed in this

thesis. A RHEED system used in this thesis is manufactured by STAIB INSTRUMENTS with remote controls for adjusting the beam x- and y-position and for beam blanking to minimize damage to the substrate. Despite the ability of the electron gun contained in the growth chamber to accelerate electrons up to 20 kV, it is usually operated at a maximum acceleration voltage of 12.5 kV to prevent sample damage. The electrons emitted from the electron gun have kinetic energy $E = \frac{1}{2}mv^2$. The wavelength of the electrons λ is given by, $\lambda = \frac{h}{\sqrt{(2m_e E)}}$ where h is Planck's constant. Simple calculation leads to the wavelength of the electron of the order of 10^{-2} Å, which is two orders of magnitude smaller than the lattice parameter of III-V materials. Grazing incidence angles of less than 5 degrees allow the electron beam to focus directly on the surface of the sample. In this case, the electron beam passes through the NWs that are grown vertically from the substrate surface. In this geometrical configuration, diffraction is primarily caused by the three-dimensional volume diffraction inside the NWs. Figure 2.6(a) schematically shows a schematic drawing of the RHEED configuration. In our case, the diffraction patterns projected on the fluorescent screen window were photographed.
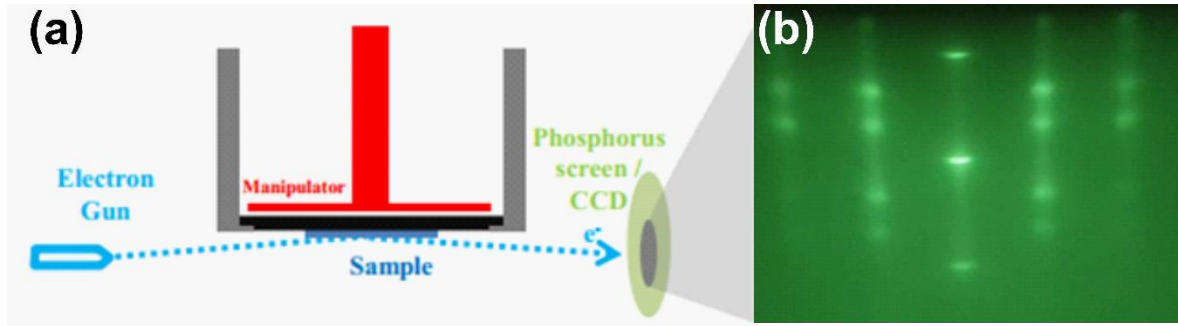
Figure 2.6: (a) Schematic drawing of RHEED and (b) a typical diffraction pattern of InP NWs grown on InP (111)B substrate along <100>.

The principles of the RHEED transmission mode are shown in Figure 2.7 [79]. A high-energy collimated electron beam from the RHEED gun passes through and interacts with the nanostructures, i.e. NWs, which stand vertically on a substrate. Electrons with an energy of a few tens of keV from the RHEED gun are transmitted through the NWs. The electrons travel to the screen and produce diffraction patterns without significant transmittance loss. These diffraction spots appear in the positions in which the Bragg condition is satisfied, analogous to the typical diffraction methods such as X-ray diffraction or electron diffraction in TEM. The diffraction pattern changes with the alignment of the beam direction with respect to the crystallographic orientation of the substrate. Indeed, we exploited this feature to align the substrate in a preferential crystallographic direction to realize asymmetric InSb NFs (details described in 4.3.4 section of chapter 4).
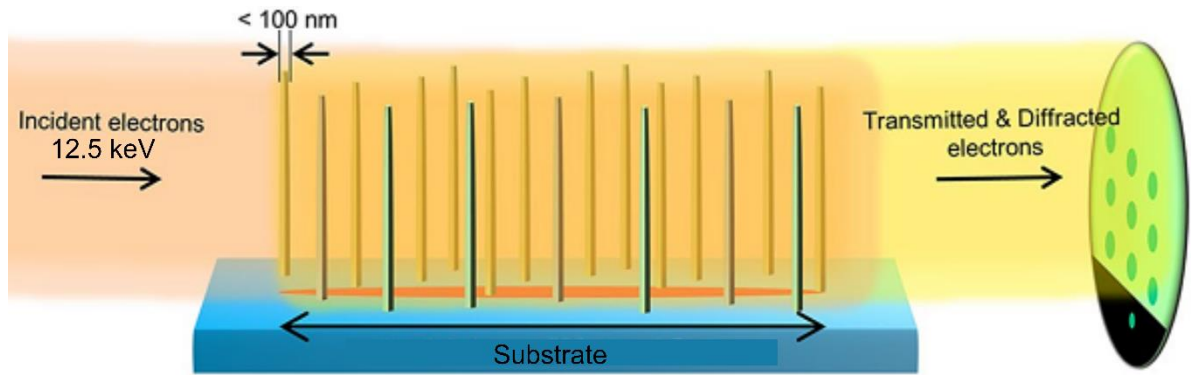
Figure 2.7: Schematic illustration of electron diffraction in RHEED transmission mode. The RHEED electron beam glances at the surface of the substrate at a grazing incidence angle.

2.3.2 Scanning Electron Microscopy (SEM)

SEM is one of the most widely used techniques in the field of material science for studying and analyzing micro-and nanoscale structures. A SEM produces images by scanning a rectangular area of the specimen with a focused electron beam (raster scanning). The SEM offers several unique advantages, including simple sample preparation, rapid feedback of as-grown sample morphology, and reduced sample damage. The electron beam is produced by thermionic or field emission. Anode and cathode are subjected to high potential differences to accelerate electrons. With the help of three electromagnetic lenses, the beam is focused on the specimen surface. The primary beam produces different kinds of signals when it strikes the sample surface, such as secondary and backscattered electrons, Auger electrons, X-ray photons, and cathodoluminescence as shown in Figure 2.8 [80]. Suitable detectors collect these signals and convert them into electric signals. One of these signals consists of secondary electrons, which are low-energy electrons produced by inelastic interactions between the electron beam and the sample. They escaped from a few nanometers of the surface of the sample. Secondary electrons generate a signal that serves as a basis for imaging sample topography. The morphology of grown NWs can be studied through this characterization technique.

A conductive adhesive such as carbon tape is usually used to attach samples to sample holders. Sample holders must be grounded to avoid the accumulation of electrical charges. Insulator samples are made conductive by a deposition of a thin conducting layer. SEM imaging of our grown array of NWs does not require sample preparation since their semiconducting nature, as well as their semiconductor substrates, make them directly image-able. To analyze the density, homogeneity, and kinks of NWs, top-view imaging was performed. 45°-tilted SEM images were used to measure the diameter and length of NWs, and the morphology of 2D and island growth.

Zeiss MERLIN and Zeiss Ultra Plus field emission SEMs operated at 5 keV were used in this study. The SEM Zeiss MERLIN is equipped with a GEMINI II column, a 5-axis motorized stage (X, Y, Z, tilt, and rotation) as well as a semi-automatic airlock. The stage and specimen surface are located at the eccentric point, which means that all rotation axes intersect at the

same point. It ensures that the specimen remains in focus when tilted at a certain working distance.
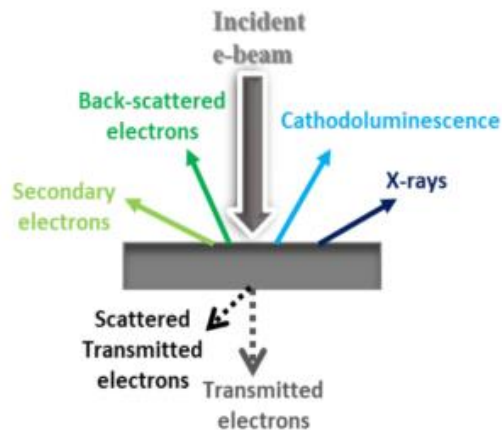

Figure 2.8: Different kinds of signals produced by the interaction of electron beam with the sample, which provide information, related to the morphology, chemical composition, and optical properties of the sample.

A resolution of 0.8 nm is possible. In addition to such high resolution, the MERLIN is equipped with Angle Selective Backscatter (AsB) and Energy Selective Backscatter (EsB) detectors that help to provide better contrast between materials during imaging. To differentiate between the InP-InSb interfaces or to examine the 2D film growth onto the substrate, a collective signal for these detectors was employed. MERLIN's airlock allows the sample to be mounted and dismounted rapidly within a few minutes. The ULTRA Plus is another high-resolution FE-SEM having AsB and EsB detectors that are mainly used for lithography.

2.3.3 Transmission Electron Microscopy (TEM)

While SEM images are good for studying the morphology of the NWs, they cannot provide any information about the crystal structure since the acceleration voltage isn't high enough to penetrate the NW. On the other hand, TEM is a more powerful and complex technique, employing accelerating voltages up to 300 kV. TEM involves measuring the transmitted electron beam and reconstructing an image of the sample from that. High-resolution TEM (HRTEM) allows for the resolution of individual atomic rows within a crystal. This technique relies on the fact that electrons are diffracted by the atomic lattice of a crystal. By inversely Fourier-transforming the diffraction pattern with the imaging lens, a high-resolution image is produced in the image plane, which allows the crystal structure of the NWs to be studied. Various detectors are used to collect different types of information, including backscattered and secondary electron detectors, electron energy loss and X-ray detectors, and bright-field (BF) and dark-field (DF) transmitted electron detectors. Furthermore, it gives details on the crystal structure, quality, and size of different kinds of materials, structural defects, grain boundaries, dislocations, strains, and chemical compositions of different materials.

Another extraordinary feature of HR-TEM is scanning TEM (STEM) mode which has become a valuable tool for the characterization of nanostructures. Similar to ordinary SEM, STEM works by focusing an electron beam on a point over the specimen and collecting the desired signal to generate an image. A BF detector is positioned below the sample to collect transmitted beams, whereas an annular DF (ADF) detector collects scattered electrons at small angles, and a high angle ADF (HAADF) detector collects electrons scattered at greater angles. Each detector gives a unique and compactable view of specimens. HAADF images are also called Z-contrast images since the contrast is based on the atomic number Z of the chemical element [81]. Energy dispersive X-ray (EDX) can also be used in STEM mode to determine the chemical composition of the specimen spatially. An energy dispersive spectrometer measures the X-ray spectrum produced by a focused electron beam incident on the sample. This spectrum is a fingerprint of each chemical element and its analysis gives the chemical composition of the sample. In the present work, the crystal structure, the elemental composition, and the chemical phase distribution of NWs were measured with a JEOL JEM-2200FS microscope operated at 200 keV, equipped with an in-column Ω filter and a detector for EDX spectroscopy located at the IMEM-CNR institute in Parma, Italy. Image analysis was performed either in HR-TEM mode coupled with zero-loss energy filtering or using STEM mode using a HAADF that yields atomic number Z contrast. For TEM observation, the NWs were mechanically transferred onto carbon-coated copper grids.

2.3.4 Geometric phase analysis (GPA)

The GPA is a simple and efficient method to measure strain and local lattice displacements in nearly periodic images with nanoscale resolution. In a few steps, GPA averages and fits the best lattice parameter in a given region. This method was first reported by Hytch et al. in 1998 [82]. The basic algorithm of this method is related to the Fourier transform of HRTEM images. The Bragg reflections (BR) are obtained from Fourier transmission. These BR spots represent the 2D unit cell of the corresponding crystal structure of the HRTEM image. A sharp BR spot gives perfect crystal, while diffused BR spot represents variation in lattice planes of the crystal. An image is formed by choosing these two BR reflection spots, which help to determine the local variation of the corresponding crystal structure. The image is considered to be composed of a reduced set of major image periodicities. Each periodicity has an associated Fourier component which is allowed to vary as a function of position. The local amplitude and geometric phase of lattice fringes can be determined in this way by filtering in Fourier space. A direct relationship is then established between the phase and the displacement of lattice fringes, and between the gradient of the phase and the local reciprocal lattice vector.

In our case GPA maps of InAs-InSb and InP-InSb nanostructures were performed by using STEM cell software [83] to quantify the strain field at InAs-InSb and InP-InSb heterointerfaces as well as to directly observe the lattice mismatch.

2.4 Device fabrication

To fabricate the devices, the as-grown InSb NFs were dry transferred on a pre-patterned p-type Si(100) substrate, covered with 285 nm-thick SiO_2 layer, which serves as a global back gate. During the mechanical transfer, the InSb NFs are detached from the InP NW stems, so that well isolated InSb NFs were found lying randomly distributed on the substrate. Then the position of selected InSb NFs was determined relative to predefined alignment markers using SEM images. Considering the thickness and the edge geometry of the InSb NFs, electrodes were patterned on a 400 nm thick layer of AR-P 679.04 resist with standard EBL. Before metal deposition, the samples were chemically etched for 1 min in a 1:9 $(NH_4)_2S_x$ DI water-diluted solution at 40°C, to remove the thick native oxide layer from the exposed NF areas and then rinsed for the 30s in DI water. Next, a 10/190 nm Ti/Au film was deposited using thermal evaporation, followed by lift-off. Figure 2.9 shows a device fabricated following the explained procedure.
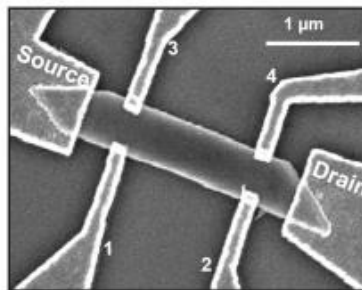
Figure 2.9: SEM image of an InSb NF Hall-bar device with corresponding numbers for Hall-bar contacts.

After fabrication, the chip was attached to the die pad of a Dual In-Line (DIL) chip carrier, using silver conductive paste. The oxide on the back of the Si chip is previously reduced by scratching it with a diamond scriber, to ensure good electrical contact between the DIL die pad and the backside of the sample. Therefore, we can apply voltage to the device's backside and operate backgating. We also connect frame pads to DIL pads, so that we can electrically contact specific leads. To create these connections, we use the so-called bonder machine, shown in figure 2.10, which melts thin gold wire extremities using ultrasound pulses. In figure 2.10 an example of a device ready for measurement is also shown.

Figure 2.10: Ultrasonic wedge bonder machine and final bonded device.

2.5 Electrical characterization

The measurement setup required for InSb-based NF devices (four-probe, and hall-bar measurements in chapter 4 and Josephson field-effect transistor (JoFET) measurements in chapter 6) is briefly described. We will first describe how we can obtain low temperature regimes in which we need to perform electrical characterization using cryogenic systems. Afterward, we will list and briefly describe the electrical measurement equipment we used at the NEST laboratory to electrically characterize InSb-based devices.

2.5.1 Cryogenics

Low temperature measurements were performed in a HelioxVL cryostat by Oxford instruments. The system consists of a vacuum loaded ^3He cryostat, which allows us to perform measurements at temperature down to a lower limit of 250mK and magnetic fields up to 12T. The sample under test is placed in a sample socket located at the bottom of the insert. During operation the cryostat is inserted in a liquid helium storage dewar, consisting of several chambers, as represented in figure 2.11:
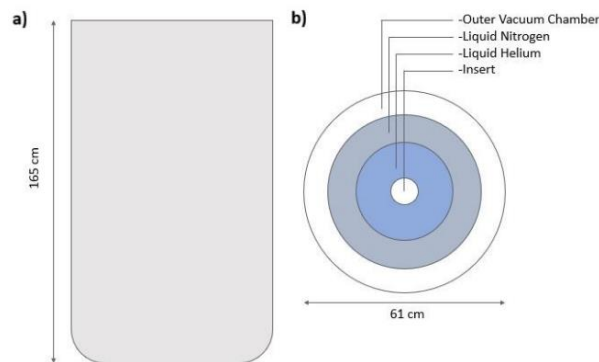
Figure 2.11: Schematic representation of the dewar hosting the insert (a) front view and (b) top view.

The outer vacuum chamber (OVC) serves as thermal isolation for internal chambers, to avoid having liquid nitrogen in thermal contact with the external environment, thus causing huge gas evaporation and consequent loss. Furthermore, the chamber containing liquid nitrogen isolates the area containing liquid helium, which is our main thermal bath (4.2 K temperature), by minimizing radiative heating. This means that, without following any additional step, we can achieve sample temperatures down to 4.2 K by simply dipping the insert (which is represented in Figure 2.12) in the dewar.

Moreover, it is possible to achieve temperatures down to 250mK in our system by proceeding with the so-called condensation procedure. This mainly relies on the fact that by pumping over vapor in thermodynamic equilibrium with a liquid we are basically removing "hot" particles and thus cooling down our system. Here, this is implemented using ^3He vapor and a sorption pump, as shown in figure 2.12. Pumping on ^4He vapor here is needed to condensate ^3He, whose condensation temperature is 3.3 K, lower than liquid ^4He temperature.

Figure 2.12: Picture showing helioxVL insert at NEST laboratory.

The sorption pump (referred as sorb) will absorb gas when cooled below 40 K; moreover, the amount of gas that it absorbs depends on its temperature. It is cooled by drawing out some liquid helium from the main bath, while a local heater is fitted near the sorb so that its temperature can be precisely controlled during the operation. The 1K pot is used to condense the ^{3}He gas; it is fed from the liquid helium bath thanks to the capillar shown in figure 2.12 and a needle valve which allows us to regulate how m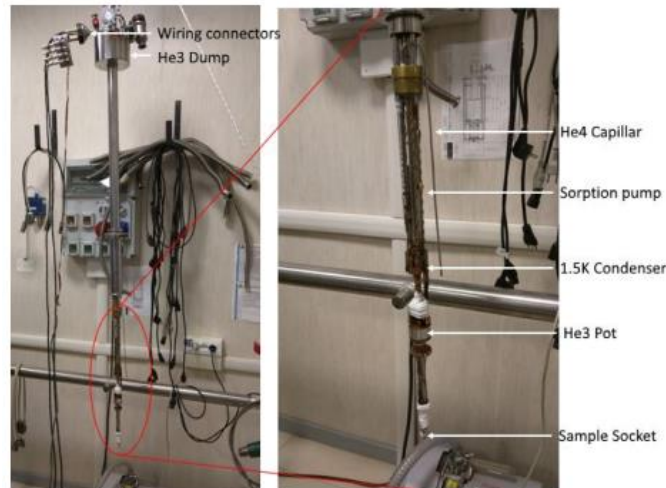uch liquid helium is drawn. When preparing for condensation, the sorb is warmed above 40 K, so that it won't absorb ^{3}He: it will instead desorb any residual ^{3}He.

We cool down the 1K pot pumping ^{4}He out of it using a scroll pump so that ^{3}He condenses and falls to cool the sample and ^{3}He pot to the temperature of the 1 K pot. When most of the gas has condensed, the 1K pot needle valve is closed so as ^{4}He from the main bath is not needed anymore. Now the ^{3}He pot is full of liquid ^{3}He at approximately 1.2 K (figure 2.13a). We now cool down the sorb, so that it reduces vapor pressure above the liquid ^{3}He in the pot and consequently sample temperature drops. As the limit pressure is approached, the temperature of the liquid ^{3}He and thus our sample temperature can be reduced down to 250 mK the lowest operating temperature of the system.

An important feature of this system is that sample temperature can be controlled by adjusting the temperature of the sorb. Setting it between 10K and 40K (and thus not working in the total absorption or total desorption regime) makes it possible to control the pressure of the ^{3}He vapor and thus the temperature of the liquid ^{3}He. To obtain this control in a precise way, we use a temperature controller (Intelligent Temperature Control 503 -ITC 503- by Oxford Instruments) which monitors temperatures of the sample, sorption pump, and 1K pot. Moreover, ITC503 is linked to local heaters near these areas. This allows us to achieve great and stable control on our system working temperature, allowing us to carry on long measurements also at higher sample temperatures.
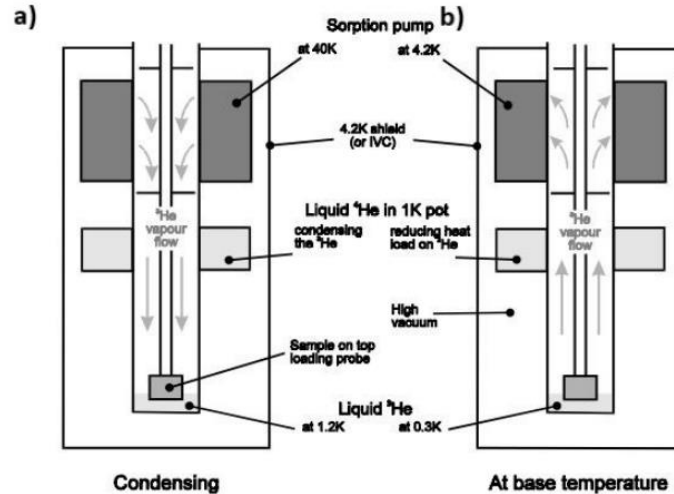
Figure 2.13: Schematics of the Oxford Instruments, Heliox system, illustrating the inner workings of the cryostat at base temperature and during condensation.

2.5.2 Measurement equipment

The setup consisted of different types of equipment for voltage and current supply and detection. In particular, we used the following instruments:

- Yokogawa 7651 Programmable DC Source:
- HP 4142B Modular DC Source/Monitor:
- Keithley 2400 SourceMeter:
- Agilent 34410A Multimeter:
- SR830 DSP Lock-In Amplifier:

These equipment have been used to measure IV characteristic (DC), 2 probe measurement (DC), 4 probe measurement (DC and AC configuration), Hall-bar measurements, and JoFET measurements in chapters 4 and 6, respectively.

Chapter 3: InSb nanostructures on InAs stems

3.1 Introduction

The growth of InSb nanostructures with controlled morphology is challenging owing to the low vapor pressure of Sb and its properties as a surfactant [68]. In general, the narrower growth window of III−Sb in comparison to other III−Vs (III−P and III−As) is due to the surfactant effect of Sb atoms, as the atoms tend to segregate to the surface, thereby modifying the surface energy [68, 69]. For this reason, it is essential to investigate the growth mechanisms and the morphology of free-standing InSb nanostructures. Various research groups reported studies on free-standing 2D InSb nanostructures, which are referred as nanosheets [84] or nanosails [47] via Ag- or Au-assisted epitaxial growth. However, these nanosheets/nanosails are occasionally formed within a "forest" of NWs, and subsequently, the yield is rather low. A recent study combines SAE growth with the VLS mechanism in MOVPE, leading to the formation of InSb nanoflakes thanks to the development of a twin-plane boundary [85]. Similar results are reported in the case of nanosails grown on InAs stems using MBE, where the instability of the catalyst nanoparticle triggers the formation of the twin plane, essential for the development of the 2D shape [47]. Other studies realized 3D morphologies like InSb nanocubes (NCs) [86] and nanocrosses [87]. The evolution from NWs to NCs was explained in terms of the V/III ratio and the NW-to-NW distance, both having the same influence. The missing link in all studies so far is rational control of the InSb morphology transition from 1D to 2D and 3D.

In this chapter, we first discuss the growth of InSb nanostructures such as NWs (1D), NFs (2D), and NCs (3D) with different morphologies on InAs NW stems without any pre-growth step (substrate patterning). The following section of the chapter proceeds by discussion of general growth protocol details followed by the realization of InSb NWs, NCs, and NFs by tailoring the growth parameters like growth temperature, sample rotation substrate orientation, and precursor fluxes. The later section of the chapter focuses on the analysis and characterization of as-grown InSb NFs. The transmission electron microscopy measurements and the atomic model were performed in collaboration with Dr. Francesca Rossi (IMEM-CNR, Parma, Italy). The results presented in this chapter are published in Ref. 88.

3.2 Growth protocol of InAs-InSb heterostructures

3.2.1 General experimental details

The InAs-InSb axial heterostructures of the present study were grown by CBE on InAs (111)B substrates by the Au-assisted growth [89, 90]. The substrate was prepared by using 30 nm Au colloids drop-casted onto the bare substrate as seeds to catalyze the growth using MO precursors as TMIn, TBAs, and TMSb. Further information on the substrate preparation is given in chapter 2 subsection 2.1.1. The grown heterostructures consist, from bottom to top, of an InAs stem followed by the InSb segment. The InAs stems were grown for 45 min at the growth temperature

(T_{InAs}) of 385°C using 0.6 Torr and 1.5 Torr of TMIn and TBAs line pressures, respectively. Then the group V flux was abruptly switched from TBAs to TMSb, with no variation in the TMIn flux. The InAs stems were always grown rotating the substrate at 5 rpm to have a uniform distribution of precursor fluxes during the growth. The sample rotation during the growth of the InSb segment will be specified explicitly case by case. The InSb growth temperature (T_{InAs} + ΔT, where ΔT is negative) and the TMSb line pressure were varied to obtain the different InSb morphologies like NWs, NFs, and NCs. All the samples were cooled down to room temperature in a UHV environment, without group V precursor flux, to prevent the accumulation of Sb on the heterostructure sidewalls.

3.2.2 Growth protocol of InSb NWs and NCs

To study the effect of each growth parameter on the nanostructure morphology, we changed only one parameter at a time, keeping all others fixed.

First, we studied the effect of the InSb growth temperature, T_{InAs} + ΔT.
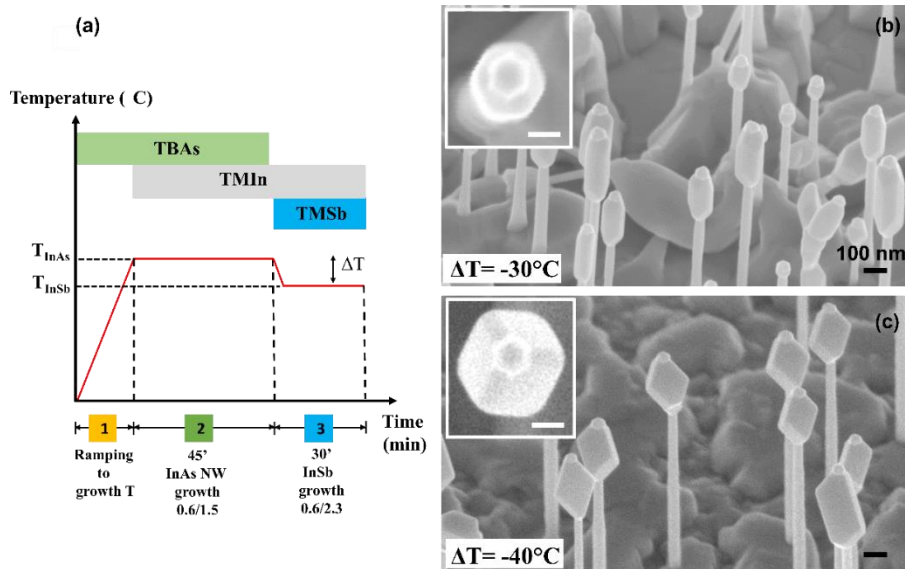
Figure 3.1: InSb NWs and NCs. (a) Schematic of the growth process developed for obtaining InSb NWs and NCs. 45°-tilted SEM images of InSb NWs (b) and NCs (c) obtained at ΔT = -30°C and ΔT = -40°C, respectively. High magnification top-view SEM images are shown in the insets (scale bar corresponds to 50 nm).

Figure 3.1 shows the growth processes developed and the nanostructures obtained at different ΔTs. Panel (a) is the schematics of the growth protocol: the growth of InAs NW stems was followed by InSb growth for 30 min using 0.6 Torr of TMIn and 2.3 Torr of TMSb at the growth temperature, T_{InAs} + ΔT. The substrates were rotated at 5 rpm for the whole process. Interestingly, we obtained different InSb morphologies at different ΔTs: NWs (1D) at -30°C and NCs (3D) at -40°C. Panel (b) shows 45°-tilted and top view (inset) SEM images of InSb NWs with an average length of (291 ± 46) nm and diameter of (94 ± 12) nm with a hexagonal cross-section comprising of six equivalent {110} oriented sidewalls. Panel (c) shows instead of

the 45°-tilted and top view (inset) SEM images of InSb NCs still having a hexagonal cross-section with sides parallels to the equivalent {110} directions, but with average length and diameter of (314 ± 32) nm and (148 ± 14) nm, respectively. In both samples, the InAs stems have a hexagonal cross-section with six equivalent {112} sidewalls, which are 30° rotated with respect to {110} facets of the InSb segment, consistent with our previously reported results [91]. Accordingly, we expect the InAs NW stems to crystallize in the wurtzite phase (WZ), while the InSb NW segment has a zinc blend (ZB) structure. These results show that a morphological transition from NWs to NCs is achieved by decreasing the ΔT by 10°C while keeping the other growth parameters (time and fluxes) fixed. This suggests that the InSb radial growth rate is enhanced at lower growth temperatures and hence a 3D morphology is favored.

3.2.3 Effect of substrate rotation and orientation

Following the same growth protocol that for InAs-InSb heterostructured NWs, but before initiating the growth of InSb segments the substrate rotation was stopped. By stopping the rotation, we trigger asymmetric growth, and as a result, we obtain elongated InSb NWs, which we refer to as, asymmetric InSb NWs. Indeed, all the NWs show a radial elongation in the same direction i.e. [-12-1] (denoted by yellow arrow), as visible from top-view SEM images in Figure 3.2.
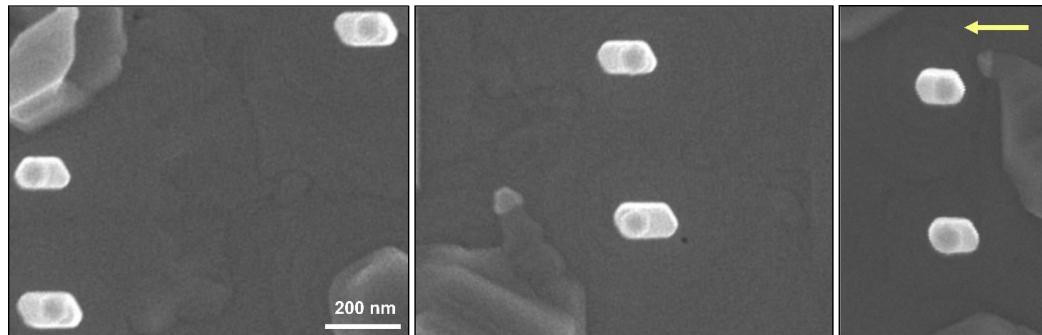
Figure 3.2: Top view SEM images of asymmetric InAs/InSb NWs recorded from different parts of the substrate. The substrate orientation is [-12-1] (denoted by yellow arrow) in all images. The scale bar is 200 nm for all images.

To analyze and understand the asymmetric InSb growth, we aligned the cleaved edge surface {110} of the substrate facing the TMSb injector, so that the projection of the Sb beam impingement direction on the substrate surface is perpendicular to one of the six {110} sidewalls of the InSb NW. The geometry of the CBE C-21 system is such that the TMSb and TMIn injectors are at 60° apart so that the projections of the two impinging beams are perpendicular to two adjacent InSb sidewalls. To explain the configuration of the experiment, in Figure 3.3 (a) we schematically show a top view image of the InSb NW, with the position of the TMSb and TMIn injectors indicated by grey arrows. The substrate cleaved edge projection is denoted by the orange dashed line and the other crystallographic directions are indicated by the arrows at the top of the panel.
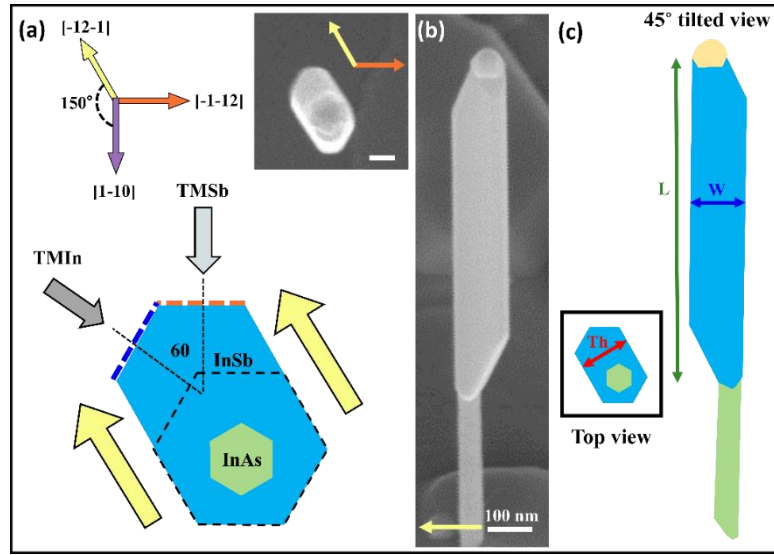
Figure 3.3: Asymmetric InSb NWs growth. (a) Schematic top view projection of InSb NW depicting the configuration of substrate and NW with respect to the beam injectors. The crystallographic directions are indicated by [-1-12] (orange arrow), [-12-1] (yellow arrow) and [1-10] (violet arrow) and the orange and blue dashed lines indicate the two side facets directly facing the injectors. The inset shows the top view SEM image of one asymmetric NW in the configuration described. The scale bar of the inset is 50 nm. (b) SEM image of one asymmetric InSb NW tilted 45° around the [-12-1] axis marked in the image. (c) Schematic representation to explain the procedure employed to measure the geometrical parameters (width: W, length: L, and thickness: T) of the asymmetric NWs from the top view and 45°-tilted view images.

The substrate rotation is stopped before starting the InSb growth and the [1-10] direction is aligned parallel to the TMSb injector. At the end of the InSb growth, we found that all the NWs are elongated in the direction forming a 150° angle with respect to the [1-10] direction. The dotted regular hexagonal cross-section in Figure 3.3(a) represents the symmetric InSb NW obtained when the substrate is rotated during the growth, while the elongated hexagon (blue) represents the asymmetric NWs obtained when the rotation is halted. The small green hexagon represents the InAs stem which has six {112} sidewalls and therefore it is rotated by 30° with respect to the InSb. The color-coded substrate crystal directions indicated here are used consistently in all figures of the chapters.

The inset in the top right part of the panel (a) shows the top view SEM image recorded with horizontal [-1-12] as indicated by the orange arrow. It is evident that the InSb is elongated along [-12-1] direction that corresponds to two specific parallel {110} facets (shown with yellow arrows in the schematics). In particular, the two facets better aligned with both the TMSb and TMIn beam directions are elongated.

The reason for the asymmetric growth can be explained by the system geometry itself. Indeed, epitaxial growth techniques are directional, and the substrate is typically rotated to facilitate

uniform growth [92, 93]. When the rotation is stopped, precursor availability on the six NW facets depends strongly on the specific facet. The two facets facing the injectors (marked with orange and blue dashed lines in Figure 3.3 (a)) are reached by both precursors by direct impingement. The two elongated facets are reached only by one of the two precursors and at a reduced rate due to the grazing incidence of the flux. The two bottom facets (opposite to those marked with the orange and blue dashed lines) receive neither In nor Sb precursors directly impinging on them. As a consequence, when the rotation is stopped, the growth rate of the NW sidewalls facing the injectors will be higher compared to the growth rate of the other NW facets that are somehow screened from the direct beams [94].

Panel (b) shows a tilted (45° around the [-12-1] axis) SEM image of a single asymmetric InSb NW. The [-12-1] direction (yellow arrow) is marked in the image. Panel (c) indicates how the geometrical parameters are measured. In particular, from the top view SEM images, the thickness (red arrow) is measured as the distance between the two elongated sidewalls. Then, the microscope sample holder is rotated such that one elongated facet is aligned horizontally, and 45°-tilted images are recorded (like the one shown in panel (b)) to measure the length (green arrow) and width (blue arrow) of the asymmetric InSb NWs. The measured lengths on 45°-tilted images are multiplied by a factor $\sqrt{2}$ to obtain the real NW length. For this sample, measuring 30 randomly selected nanostructures, we obtained an average length, width, and thickness of (1048 ± 108) nm, (112 ± 18) nm, and (87 ± 12) nm, respectively. The uncertainties are standard deviations of the measured values.

3.2.4 Effect of InSb growth temperature

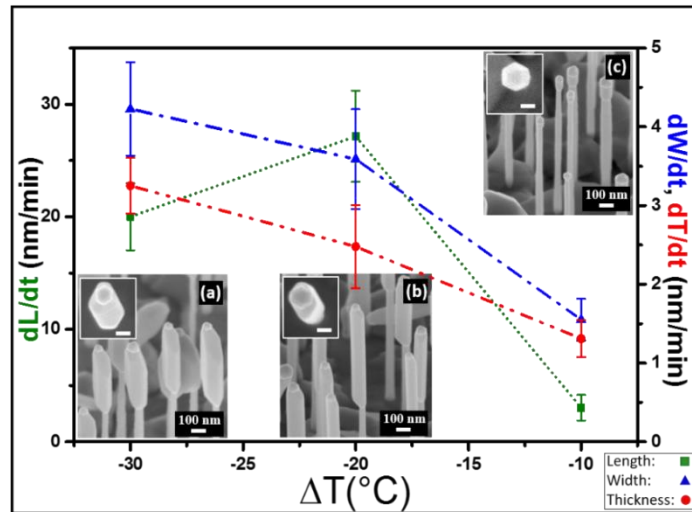**Figure 3.4:** Growth rate of asymmetric InSb NWs versus ΔT. 45°-tilted SEM images of morphologies obtained at ΔT (a) -30°C, (b) -20°C, and (c) -10°C. Insets represent respective top-view SEM images (scale bar: 50 nm).

To evaluate the effect of the growth temperature on the aspect ratio of the asymmetric InSb NWs grown without rotation of the substrate, we grew three samples at ΔT of -30°C, -20°C,

and -10°C and measured the geometrical parameters described above. The results are summarized in Figure 3.4, which shows a plot of the growth rates for length, thickness, and width of the InAs-InSb heterostructured NWs obtained as a function of InSb growth temperature. The growth rate of length, width, and thickness is marked by square, triangle, and circle, respectively (lines are just a guide for the eye). For ΔT=-30°C, InSb morphology is as depicted in panel (a). For ΔT= -20°C (panel (b)), the axial growth rate (length) is enhanced while the radial growth rates (width and thickness) are decreased. Further changing the temperature to ΔT = -10°C (panel (c)) leads to a drastic decrease of both axial and radial growth rates, suggesting that the temperature is too high for the growth of InSb at aforementioned line pressures (see subsection 3.2.2). The rate of desorption is in fact enhanced at higher temperatures, as the InSb sublimation temperature, known to be around 400°C [95], is approached. On the other hand, a much lower growth temperature enhances the radial growth and the system is drifted toward a 3D morphology. Indeed, the best temperature for obtaining the 2D morphology is ΔT= -20°C. The very narrow temperature window available to obtain a substantial difference in axial and radial growth rates makes it challenging to realize and control the 2D morphology and therefore it becomes important to study also the effect of the other growth parameters.

3.2.5 Effect of increasing TMSb flux

To this end, we investigated the shape evolution of the asymmetric NWs obtained at fixed ΔT of – 20°C, by increasing the Sb flux during growth.
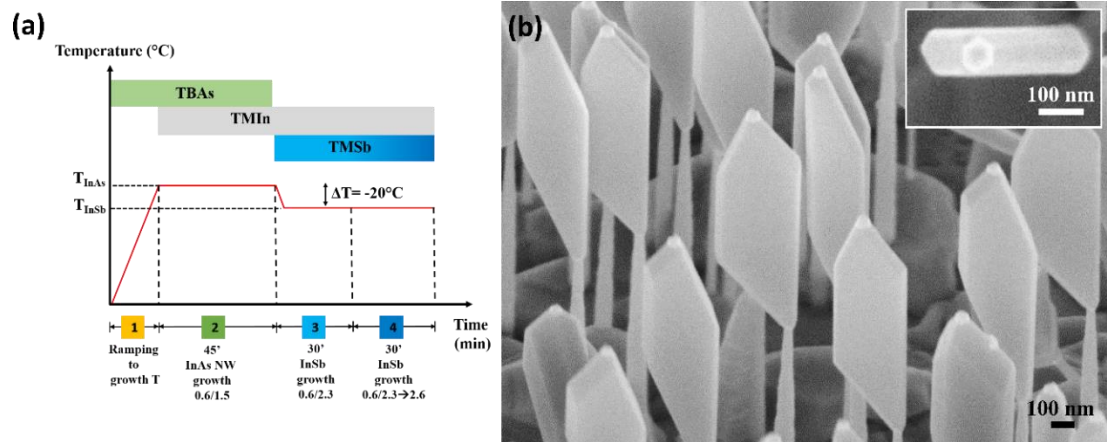
Figure 3.5: InSb NFs (a) Schematic of growth process developed for obtaining InSb NFs. (b) 45°-tilted SEM images of InSb NFs with top view SEM image shown in the inset.

Figure 3.5 shows the growth protocol developed and the InSb NFs obtained. Panel (a) shows the schematics of the growth process that now includes an additional step (labeled n. 4 in the panel) with respect to the asymmetric NWs obtained at ΔT= -20°C (Figure 3.4 panel b): 30 min growth with a linear increase of the TMSb line pressure from 2.3 Torr to 2.6 Torr still without substrate rotation. This additional step enhances only the width growth rate of the NFs, keeping length and thickness growth rate almost unchanged and hence promoting free-standing 2D

morphological growth. Panel (b) shows 45°-tilted and top view (inset) SEM images of the InSb NFs obtained having average length, width and thickness of (1.3 ± 0.1) μm, (282 ± 87) nm and (104 ± 17) nm, respectively. It should be highlighted that we have successfully obtained nearly 100% yield of these NFs. A large-scale SEM image of the as-grown InSb NF sample in Figure 3.6 (a) demonstrates the high yield and the general morphology control of this NF growth protocol. It should be noted that also in this case the direction of elongation of all the NFs is the same.
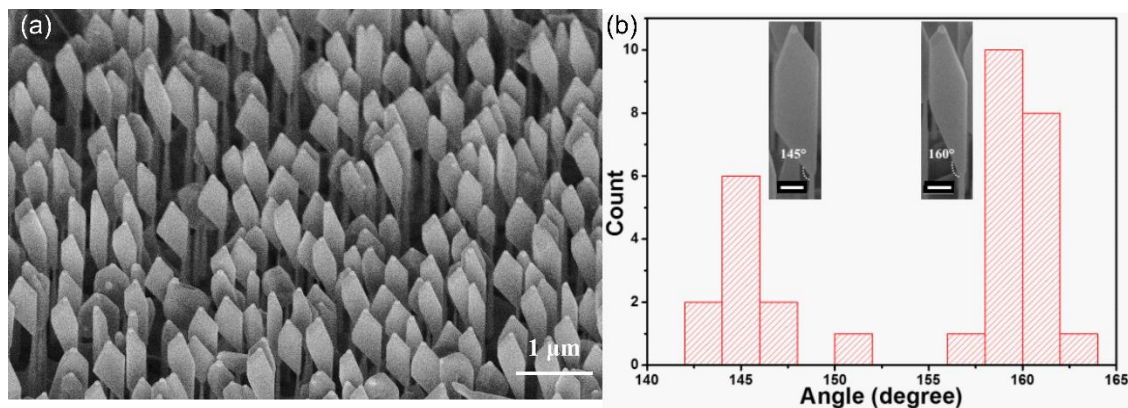
Figure 3.6: (a) Low magnification 45°-tilted SEM image of InSb NFs. (b) Distribution of InSb NFs with aperture angle of 145° and 160°. Insets show NFs with aperture angle of 145° (left) and 160° (right). The scale bar is 200 nm.

By investigating the transferred InSb NFs lying flat onto the substrate, we could image and measure the angles made by the facets via SEM. Interestingly, there are two different morphological families to which the NFs belong. Both families are elongated in the same direction but show a different angle at the base between the InAs stem and the InSb flag in the elongation direction, referred to in what follows as the aperture angle. The value for the aperture angles is about 145° and 160°. The aperture angle is the angle formed by the NF base facet and the InAs stem. The statistics concerning the two families of NFs are shown in Figure 3.6 (b). Further confirmation of aperture angles is provided by viewing the detached NFs in a perpendicular direction to the major {-101} facets from HRTEM images. It was found that the distribution is bimodal and the population of the two families: one with an aperture angle of 145° and the other with 160° is close to 40:60.

The reason for the existence of 145° and 160° aperture angle NF is explained by intrinsic InSb lattice rotation, which is discussed later in the chapter. It is worth mentioning that the final polyhedral shape of the NFs is the result of the complex growth mechanisms, which can be described as an interplay between the VLS axial growth and the asymmetric vapor-solid (VS) radial growth. Indeed, the two mechanisms simultaneously occur, and the final position of the Au nanoparticle differs from the initial one (axially aligned with the InAs stem) due to the asymmetric impingement direction and the width extension of the NFs.

3.3 Characterization of InSb NFs

3.3.1 Crystal structure

To study the crystal quality of the InSb NFs, we mechanically transferred them from the as-grown sample onto carbon-coated copper grids, and the crystal structure and facet orientation were examined by HRTEM. Figures 3.7 and 3.8 reports the TEM analysis of two represe NFs from the family with an aperentative angle of 145° and 160°, respectively. Both NFs have a major (10-1) and (-101) flat facet, bordered by 6 sides, parallel to 3 pairs of directions: [-10-1] (dashed arrows), [-1-2-1] (dotted arrows), and [-1-1-1] (solid arrows, aligned with the growth axis). Electron diffraction patterns (see FFTs in Figures 3.7b and 3.8b) and high-resolution imaging of NF portions (see panels 3.7 (c,d) and 3.8 (c-e)) show that the InSb NFs have a perfect ZB crystal structure free from any stacking faults or twinning defects.
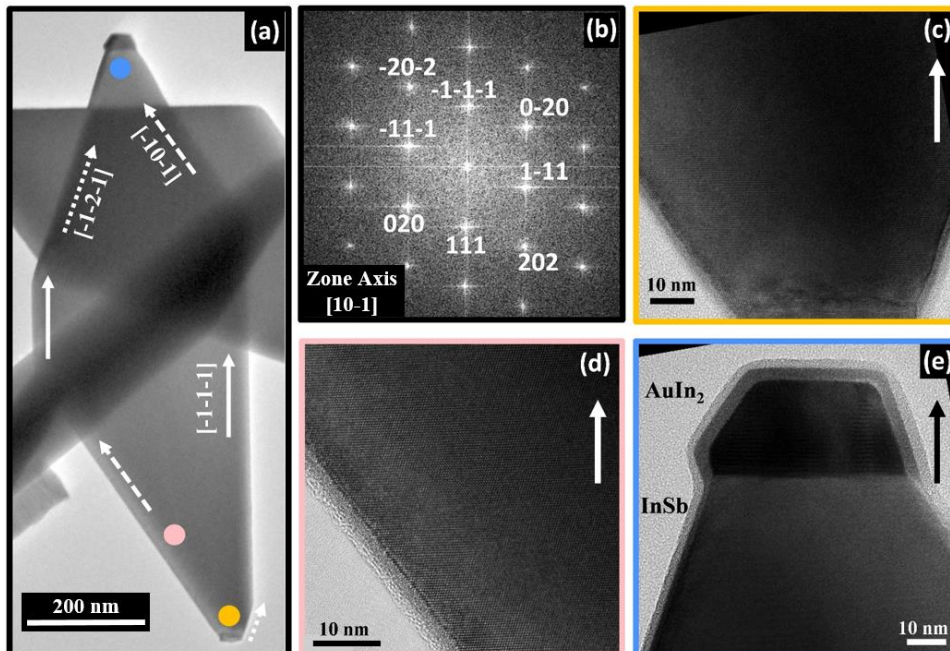
Figure 3.7: Shape and crystal structure of a single InSb NF with an aperture angle of 145°. (a) Low magnification TEM image of the NF, oriented in [10-1] zone axis. The arrows indicate the [-1-1-1] growth direction and the directions of the other flake sides. (b) Corresponding fast Fourier transform (FFT) acquired along [10-1] zone axis. (c-e) High-resolution images of the NF base (yellow region), the lateral lower side (pink region), and the AuIn$_2$ seed particle (blue region). In all the panels the solid arrows indicate the NF growth direction.
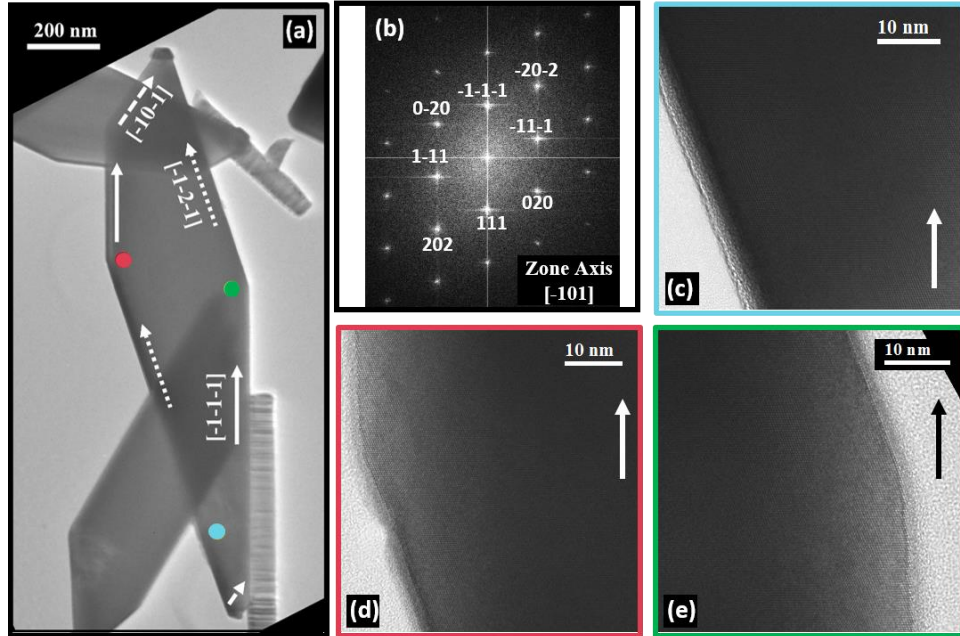
Figure 3.8: Shape and crystal structure of a single InSb NF of the same as-grown sample, with an aperture angle of 160°. (a) Low magnification TEM image of the NF, oriented in [-101] zone axis. The arrows indicate the [-1-1-1] growth direction and the directions of the other flake sides. (b) Corresponding FFT. (c-e) High-resolution images of the lower lateral facet (light blue region), left corner (red region), and right corner (green region) with the solid arrows indicating the NF growth direction.

Not all the NFs obtained in the same as-grown sample show all six well-developed sides. Indeed, we also found five-sided InSb NFs (shown in Figure 3.9). However, all the analyzed NFs show single-crystalline and defect-free ZB crystal structure, regardless of the number of side facets developed and of the aperture angle.

The post-growth chemical composition of various seed particles and InSb NFs were evaluated using EDX point analysis. We analyzed numerous NFs and all the results were found to be consistent. The quantification done by the intensity ratio of M-line of Au and L- line of In suggests that the seed particle is an $AuIn_2$ alloy, similarly to the particles found on the InSb NW tips [67] and that the InSb NF is made of In and Sb in stoichiometric ratio. The heterointerface between the InSb NF and the metal alloy seed particle (see Figure 3.7 e) is sharp and there are no traces of gold diffusion within the NF structure.
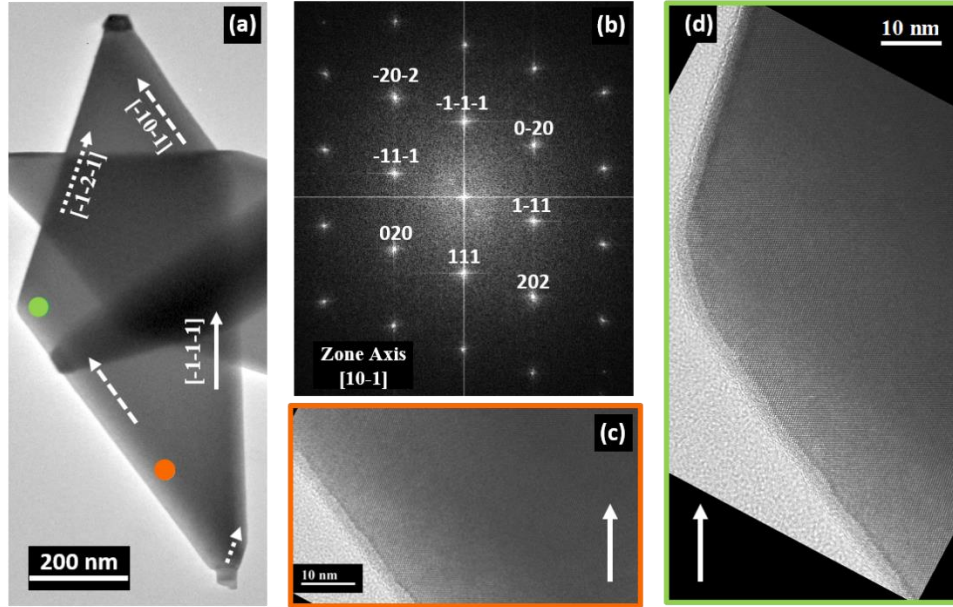
Figure 3.9: Shape and crystal structure of a 5-sided InSb NF obtained in the same as-grown sample. (a) Low magnification TEM image. The arrows indicate the [-1-1-1] growth direction and the directions of the other flake sides. (b) Corresponding FFT acquired along [10-1] zone axis. (c, d) HRTEM images of the lower lateral facet (orange region) and left corner (green region).

3.3.2 Strain mapping

For the detailed strain analysis at the heterointerfaces, a high-resolution TEM image (panel (a) of Figure 3.10) was acquired and processed with the GPA method to extract the local components of the strain in the <121> and <111> directions. In general, strain from the GPA map is defined as $\varepsilon_{GPA} = (d_{loc} - d_{ref})/d_{ref}$, where d_{loc} is the interplanar spacing of the local part and d_{ref} is the interplanar spacing of reference part which is InAs in our case.

Figure 3.10 shows the results of our HRTEM-GPA analysis for the InAs-InSb interface. Panels (b), and (c) are the corresponding GPA maps of ε_{xx} (i.e. variation of the interplanar spacing in the <121> direction, parallel to the interface) and ε_{yy} (i.e. variation of the interplanar spacing in the <111> direction, perpendicular to the interface). Panel (d) shows the averaged line profile of ε_{xx} and ε_{yy} across the InAs-InSb interface heterointerface, respectively. A step-like change from about 0.936 (InAs) to 1.000 (InSb) for ε_{xx} and ε_{yy} is observed, consistently with the 6.4% lattice mismatch between the two materials. A thing worth appreciating, which is also confirmed from these maps, is that the strain or defects in the InAs NW segment are relaxed at the NW sidewall and are not propagated to the InSb segment (or propagated only up to 50 nm from the InAs-InSb interface) leading to strain-less InSb.
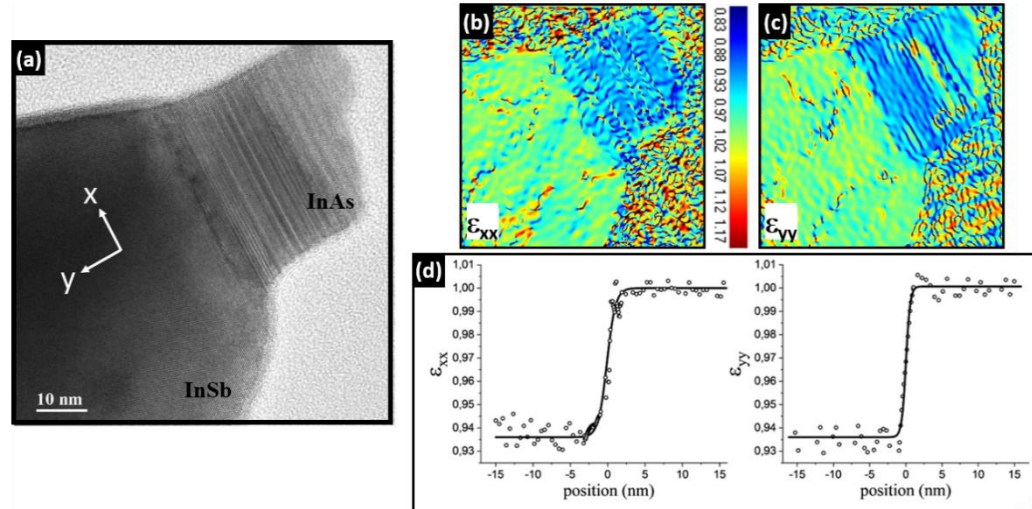
Figure 3.10: Strain analysis. (a) HRTEM image of InAs-InSb interface region of the NF. GPA maps of strain component (b) ε_{xx} and (c) ε_{yy}. (d) Line profile of ε_{xx} and ε_{yy}.

3.3.3 Modelling for InSb NFs

A model to explain the NF structure can be proposed, starting from the development of six additional facets at the InAs-InSb interface, as we previously identified in heterostructured InSb-InAs NWs [89]. This model involves {100}, {110}, and {111} facets, which are low Miller index surfaces and so they have the lowest energy in III-V materials [96] and are often observed in antimony-based NWs [97]. Based on the TEM analysis of the crystal directions of the NFs (Figures 3.7(b) and 3.8(b)), we can observe that the InSb lattice in NFs with 160° aperture angle is rotated by 180° around the growth axis with respect to the NFs with 145° aperture angle. This InSb lattice rotation and the related change of the diffraction pattern are illustrated in Figure 3.11, showing that the [-12-1] horizontal direction and the relevant directions [020] and [1-11] point towards the opposite sides for NFs with the two different aperture angles.

Figure 3.11: Schematic of the electron diffraction patterns in <-101> zone axis of the InSb NFs with an aperture angle of 160° (left) and 145° (right).

The easiest explanation would be that they are simply flipped one with respect to the other on the TEM grid. But this is not the case. The NFs elongate all in the same direction of the substrate, i.e. towards the TMIn and TMSb injectors as previously explained and visible in as grown SEM images (Figure 3.5 (b) and Figure 3.6 (a)). Both NFs of Figures 3.7 and 3.8 have the InAs stem and the corresponding vertical [-1-1-1] oriented side on their right-hand side. Thus, in both NFs the elongation has taken place towards the left, corresponding to the substrate [-12-1] direction as shown in Figure 3.3 (a). The two families of NFs truly have their crystal structure rotated by 180° one with respect to the other. This rotation does not take place in the InSb defect-free cubic crystal but rather stems from unavoidable randomness in stacking sequence when switching from the hexagonal WZ lattice of the InAs stem to the ZB InSb lattice.

Figure 3.12: Model structures of the NFs with aperture angle of 145° (a) and 160° (b).

Based on these considerations, we propose indexing of the facets as outlined in Figure 3.12. The 3D atomic models of NFs are shown in Figure 3.13. From the combination of tilted and top-view SEM and TEM images, a precise 3D atomic model was built. Statistically, we have two kinds of InSb NFs as discussed- with the aperture angle of 145° and 160°. The different structure arises due to a rotation of the InSb lattice. The faceting is visualized in a side-view.

The rotation in the InSb lattice results in the development of six facets with different indexes for systems having the [-12-1] direction pointing towards opposite sides (panel (a) and (b) in Figure 3.12). We can consider first the simpler case of symmetric NWs (depicted in Figure 3.12 on the left, in top view): the 180° InSb rotation around the growth direction produces a reversal in the position of the {100} and {111} facets, which are the facets responsible for the expansion

of the NW diameter from InAs to InSb. The NF geometry can be modeled as the evolution of the symmetric case by elongation along the [-12-1] direction or the [1-21] direction for NFs with 145° and 160° aperture angle, respectively. The major flat facets of the NFs are (10-1) and (-101) and the aperture angle (visualized in the side-view projections) is determined for the two types of flags by (010) facets - forming an angle of ~145° with the vertical (1-21) planes - or by (1-11) facets - forming an angle of 160.5° with the (-12-1) vertical planes.

Figure 3.13: A 3D atomic model representing NF facets and geometry with aperture angle of 145° (a) and 160° (b).
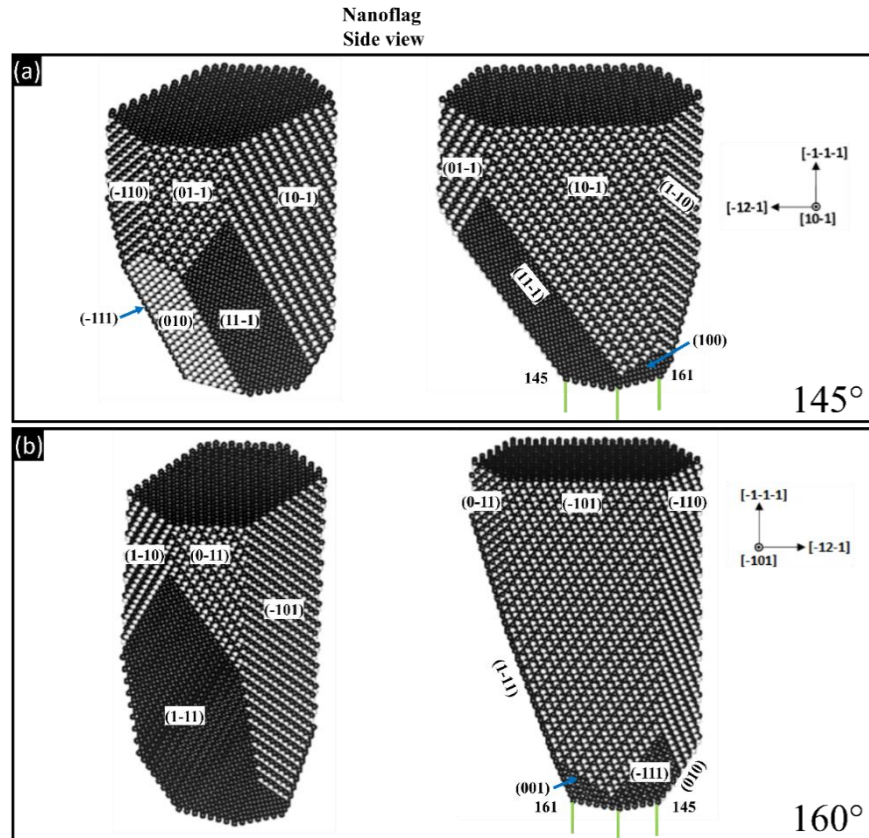
3.4 Conclusions

In conclusion, we optimized the protocols to grow InSb nanostructures with different morphologies with very good crystal quality and high yield on InAs NW stems by precisely tuning the growth parameters. The transition from InSb NWs to NCs is achieved by decreasing the InSb growth temperature by 20°C while keeping the other growth parameters (time and fluxes) fixed. Substrate rotation during the growth ensured the uniformity of the growth rate on all six equivalent NW sidewalls. As a consequence, stopping the rotation triggers asymmetry in shape and the direction of asymmetric growth is towards the impingent-beam fluxes. Moreover, an additional growth step with increased TMSb line pressure (with respect to that used for NWs) boosts the radial (width) growth rate and results in a NF morphology. The existence of two families of NFs, characterized by aperture angles of 145° and 160° at the base,

is observed and modeled. The InSb NFs are pure ZB single crystals without any defect, such as stacking faults or twin planes, regardless of the different final shape (aperture angle and number of sides). Our results provide useful guidelines for the selective growth of high-quality InSb nanostructures of different morphology.

Chapter 4: InSb nanoflags on InP nanowire stems

4.1 Introduction

In the previous chapter, we optimized protocols to grow InSb nanostructures with different morphologies with very good crystal quality and high yield on InAs NW stems by precisely tuning the growth parameters. Particularly, free-standing 2D InSb NFs allow a high degree of freedom in device fabrication and allow exploring new material properties in comparison to the 1D NWs. This motivates for growing even wider NFs but we found that the limitation in achieving larger InSb NFs was the flexibility of the thin untapered InAs NW stems. As the growth time of the asymmetric InSb segment is increased, the InAs stem bends, leading to the loss of the alignment with the precursor fluxes and consequently of the InSb orientation.

We found that a possible solution to avoid this problem is the employment of, tapered NWs to provide more stable support for the InSb NFs. This will keep them well aligned even after long growth durations. Tapered InAs NWs are not so easy to obtain because of their WZ crystal structure that reduces the radial VS growth on the NW sidewalls [98]. Instead, it is known that ZB or mixed WZ/ZB structures in NWs enhance the radial growth rate [98]. InP NWs grown by Au-assisted CBE on InP(111)B substrates have a mixed WZ/ZB crystal structure and tapered morphology [99].

Keeping this into account, in this chapter, we present the growth of InSb NFs on tapered and robust InP NWs. Furthermore, we have employed RHEED, to carefully adjust the substrate orientation with respect to the precursor beam fluxes, which minimizes the thickness of these NFs. Thanks to the larger dimension of the InSb NFs that we have obtained, we were able to realize Hall-bar devices far enough to keep the reasonable length-to-width ratio between longitudinal and transversal contacts, which avoided the presence of mixed components in Hall-bar measurements and allowed one to accurately investigate the electrical properties. The results presented in this chapter are published in Ref. [100].

4.2 InAs vs InP NW stem

Since the asymmetric InSb segment grows larger with an increase in the growth time, the thin untapered InAs stem bends, leading to the loss of the alignment with the precursor fluxes and consequently of the InSb orientation. Therefore, the preferential growth direction vanishes, and 3D-like InSb structures are obtained as shown in Figure 4.1
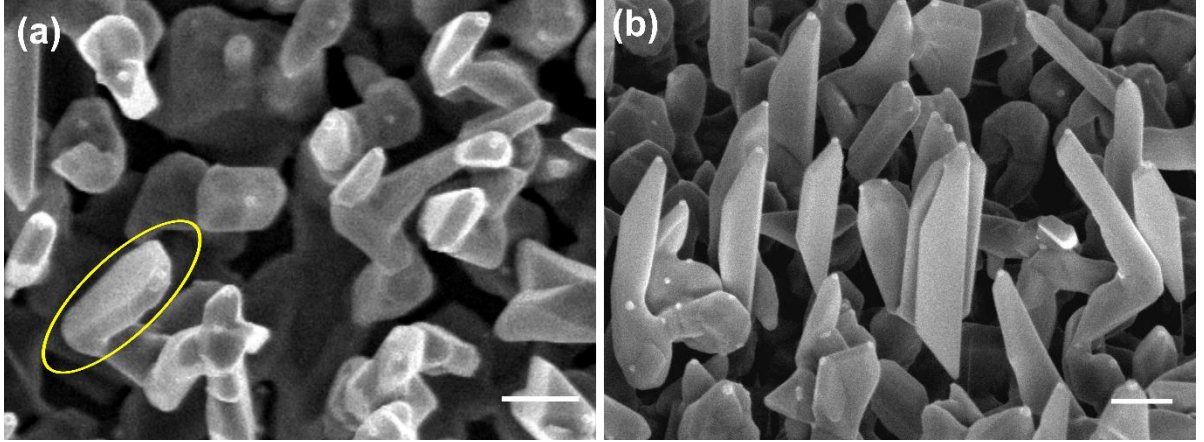
Figure 4.1: InSb NFs on InAs stem. (a) Top view and (b) 45°-tilted view SEM images of InSb NFs on InAs NW stems. Scale bar is 500 nm in all panels. The InSb NFs that have (W/T) ≥ 4 are marked by yellow circles.

Figure 4.1 shows as-grown InSb NFs on InAs stems (top view and 45°-tilted view SEM image in panels (a) and (b), respectively). The growth protocol is the same as illustrated in panel (a) of Figure 3.5 but the additional step (labeled n. 4 in the panel) is for 60 min. The criterium for the selection of preferred InSb NFs for fabricating quantum devices is defined by the following parameter:

$$\frac{Width\ of\ InSb\ NFs}{Thickness\ of\ InSb\ NFs} = \frac{W}{T} \geq 4$$

Counting the NFs satisfying this condition (marked with yellow circles in Figure 4.1), we get a yield of 1% for InSb NFs grown on InAs stems. This demonstrates a need for using more robust NW stems, like tapered InP NWs, instead of thin untapered InAs stems.

4.3 Growth protocol of InP-InSb heterostructures

4.3.1 Experimental details

The InP-InSb NFs were grown on InP(111)B substrates by the Au-assisted growth [89, 90] following a methodology very similar to that reported in Ref 88. We used 30 nm Au colloids drop cast onto the bare substrate as seeds to catalyze the growth and TMIn, TBP, and TMSb as MO precursors.

The growth sequence of the InP−InSb heterostructures consists of the growth of InP stems followed by the InSb segments. We grew InP stems for 60 min at a growth temperature (T_{InP}) of 400 °C using 0.6 and 1.2 Torr of TMIn and TBP line pressures, respectively. Afterward, the substrate temperature was ramped down by ΔT in the presence of TBP flux only to the InSb growth temperature, $T_{InSb} = T_{InP} + \Delta T$ (ΔT is negative here). To initiate InSb growth, group V flux was abruptly switched from TBP to TMSb. For the growth of the InSb segment, we used TMIn line pressures in the 0.3−0.9 Torr range and TMSb line pressures in the 0.8−2.4 Torr range, as described in the following section. At the end of the growth, samples were cooled

down to room temperature in a UHV environment without group V precursor flux to prevent the accumulation of Sb on the heterostructure sidewalls.

4.3.2 Effect of InSb growth temperature

We first studied the effect of InSb growth temperature on the final shape of the InP−InSb heterostructured NWs. Figure 4.2 shows SEM images of three samples grown at different ΔT. For all samples, the growth of the InP NW stems was followed by InSb growth for 30 min using 0.6 Torr of TMIn and 1.2 Torr of TMSb with sample rotation at 5 rpm for the whole growth duration.
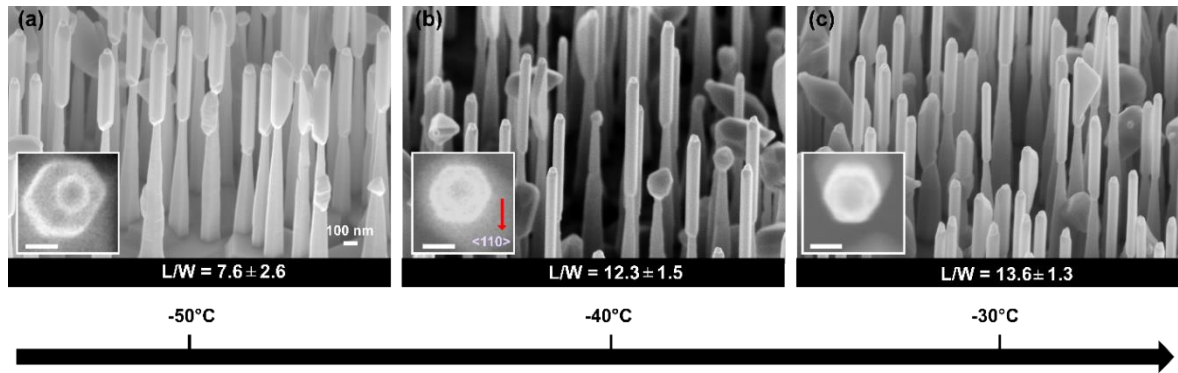

Figure 4.2: InP−InSb heterostructured NWs at different ΔT. 45°-titled SEM images of NWs obtained at (a) ΔT = −50°C, (b) −40°C, and (c) −30°C (scale of all panels is the same as in a). Insets represent respective high-magnification top-view SEM images of one representative NW with the red arrow indicating the ⟨110⟩ substrate direction (inset scale bars: 50 nm). The aspect ratio, L/W, of the InSb NWs is denoted for each ΔT at the bottom of the corresponding SEM image.

The average aspect ratio, that is, length/width (L/W) of the InSb segments, is reported at the bottom of each panel. Larger values of ΔT, corresponding to lower InSb growth temperatures, enhance the InSb radial growth rate (larger diameter) and lower the axial growth rate, altogether decreasing L/W. Increasing the temperature above ΔT = −30°C leads instead to InSb desorption, as in fact the InSb sublimation temperature is known to be around 400°C [95]. Therefore, ΔT = −30°C is the optimal InSb growth temperature to obtain a high aspect ratio InSb NWs on top of InP NW stems. The insets in each panel of Figure 4.2 show top-view SEM images of an individual InP−InSb heterostructured NW with a hexagonal cross-section of the upper InSb segment comprising of six equivalent {110} oriented sidewalls.

4.3.3 Effect of TMIn/TMSb line pressure ratios

To evaluate other growth parameters affecting the growth and the morphology of the InP-InSb heterostructured NWs, we grew the InSb segments at different TMIn/TMSb line pressure ratios.

Figure 4.3 illustrates the morphology of the InP-InSb heterostructured NWs, obtained as a function of TMIn and TMSb line pressure employed for the InSb segment growth. The x- and

y-axes denote TMSb and TMIn line pressures, respectively. All samples are grown at the optimal growth temperature of $\Delta T = -30°C$. We find that the yield (i.e., the ratio between straight InSb nanostructures and a total number of InP-InSb heterostructures, counting all straight, kinked, and non-nucleating InSb) and the heterostructure morphology strongly depends on the precursor line pressures. The InSb segments are grown in two configurations: constant TMIn and varying TMSb, or constant TMSb but varying TMIn line pressure. For the series with constant TMIn line pressure (0.6 Torr) we grew three samples with TMSb line pressure of (a) 0.8, (b) 1.2, and (c) 2.4 Torr. We found that increasing Sb flux increases the aspect ratio of the NWs. The yield is 4% for both the samples grown at lower (TMSb = 0.8 Torr) and at higher (TMSb = 2.4 Torr) Sb flux. Instead, the yield is much higher (around 86%) for the TMSb line pressure of 1.2 Torr.
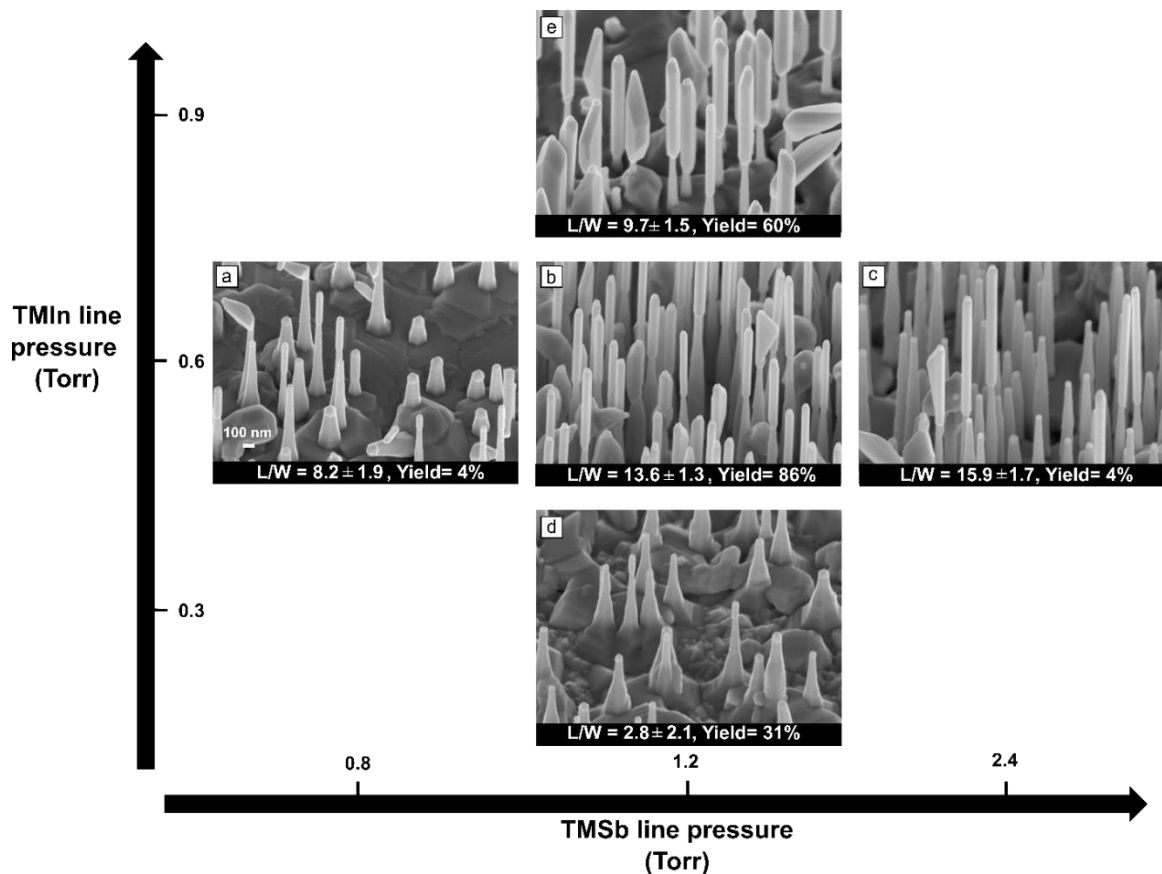
Figure 4.3: Yield and morphology map of InP−InSb heterostructured NWs as a function of the TMIn and TMSb line pressures. The InSb segments are grown in two configurations: constant TMIn but variable TMSb, and constant TMSb but variable TMIn line pressure. (a−c) The 45°-tilted SEM images of InSb segments for constant TMIn line pressure of 0.6 Torr and TMSb line pressure of (a) 0.8, (b) 1.2, and (c) 2.4 Torr. (d,e) The 45°-tilted SEM images of InSb segments for constant TMSb line pressure of 1.2 Torr and TMIn line pressure of (d) 0.3 and (e) 0.9 Torr. All images have the same scale indicated in (a).

Panels d and e of Figure 4.3 show 45°-tilted SEM images of the InP−InSb heterostructured NWs obtained at constant TMSb line pressure of 1.2 Torr and TMIn line pressure of 0.3 and 0.9 Torr, respectively. For constant TMSb line pressure, the highest L/W is obtained for TMIn/TMSb = 0.6/1.2. The InSb growth yield first increases from 31% to 86% by increasing the TMIn line pressure from 0.3 to 0.6 Torr and then drops to 60% for 0.9 Torr of TMIn. Based on the MO line pressure experiment, we found that the maximum yield is obtained at TMIn/TMSb = (0.6/1.2) while the highest L/W of 15.9 is obtained at TMIn/TMSb= (0.6/2.4). Based on these results, we can conclude that the best conditions, at $\Delta T = -30°C$, to obtain both high L/W and good yield for InSb NWs are TMIn line pressure of 0.6 Torr and TMSb line pressure in the range of 1.2−2.4 Torr.

It is worth noting that some elongated structures similar to flags are occasionally observed in the samples. However, these are very few (their occurrence is always <15%) and randomly oriented objects among many NWs with symmetric cross-sections. It might be that these asymmetric structures are formed due to partial shadowing of the beam fluxes by neighboring NWs, or to some other local effects that we did not study in detail.

4.3.4 InSb NFs
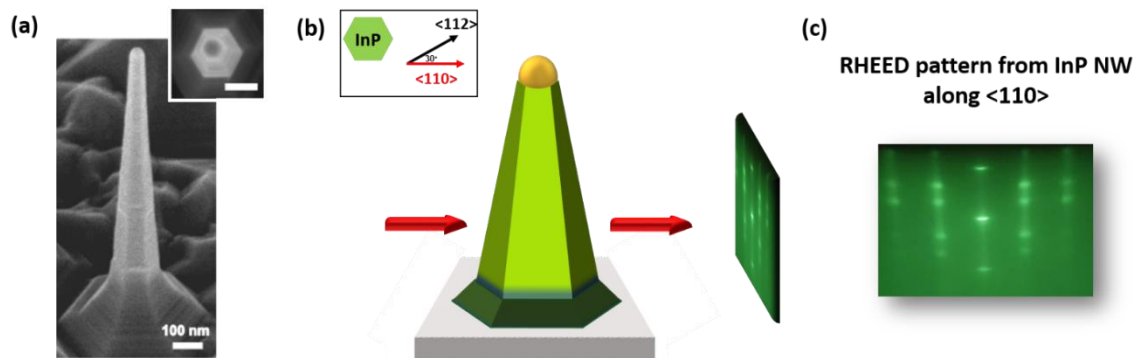
Figure 4.4: (a) A 45°-tilted and top view (inset) SEM images of an InP NW stem (scale bar: 100 nm). (b) Top view (inset) and side view representation of the alignment procedure of InP NWs with their corresponding RHEED pattern along the ⟨110⟩ direction (red arrow). (c) RHEED pattern of mixed WZ/ZB InP NWs in ⟨110⟩ direction.

The InP NW stems and InSb NWs were grown rotating the substrate at 5 rpm for the whole growth time. Conversely, there was no sample rotation during the growth of the InSb NFs, and the orientation was carefully adjusted before starting their growth with the help of the RHEED pattern. Indeed, by stopping the rotation, we trigger asymmetric growth, which is crucial to achieving the NF morphology [88]. The alignment protocol is illustrated in Figure 4.4. InP NWs grown on InP(111)B have a hexagonal cross-section with six equivalent {112} sidewalls, as visible from the SEM image (45°-tilted and top-view) of a representative NW (Figure 4.4a). Panel b shows a schematic view of the InP NW inside the growth chamber (top- and side-view) with respect to the RHEED beam (red arrow). Before initiating the InSb NF growth, the ⟨110⟩

direction was identified using the RHEED pattern as illustrated in Figure 4.4c. Indeed, this is the direction in which we can see the overlap of the WZ and ZB reciprocal lattices on the RHEED screen [92]. The substrate was then rotated by 30° to obtain an alignment with the precursor beam that maximizes the InSb NF elongation, and the InSb NF growth was initiated.

To grow free-standing InSb NFs, we can exploit our knowledge derived from the growth optimization of InSb NW on InP stems and the asymmetric InSb growth and its elongation via substrate orientation and higher Sb flux (from previous work reported in Ref 88). InP NW stems were grown with sample rotation for 90 min to provide more robust support, followed by InSb growth at $\Delta T = -30°C$ without rotation with an abrupt switch in group V flux from TBP to TMSb without variation in the TMIn flux. The growth protocol employed for the growth of InSb NFs is schematically shown in panel (a) of Figure 4.5. The initial InSb growth comprises of 0.6 Torr of TMIn and 2.3 Torr of TMSb to have a high Sb flux but still a good yield, and then an additional 60 min of growth, linearly increasing the TMSb line pressure from 2.3 to 2.6 Torr. Such Sb flux grading helps to enhance the asymmetric growth, increasing the lateral dimensions of the NFs, without compromising too much the yield of the InSb growth on top of the InP NW stems that is known to drop if the growth starts directly with higher Sb flux (see Figure 4.3).
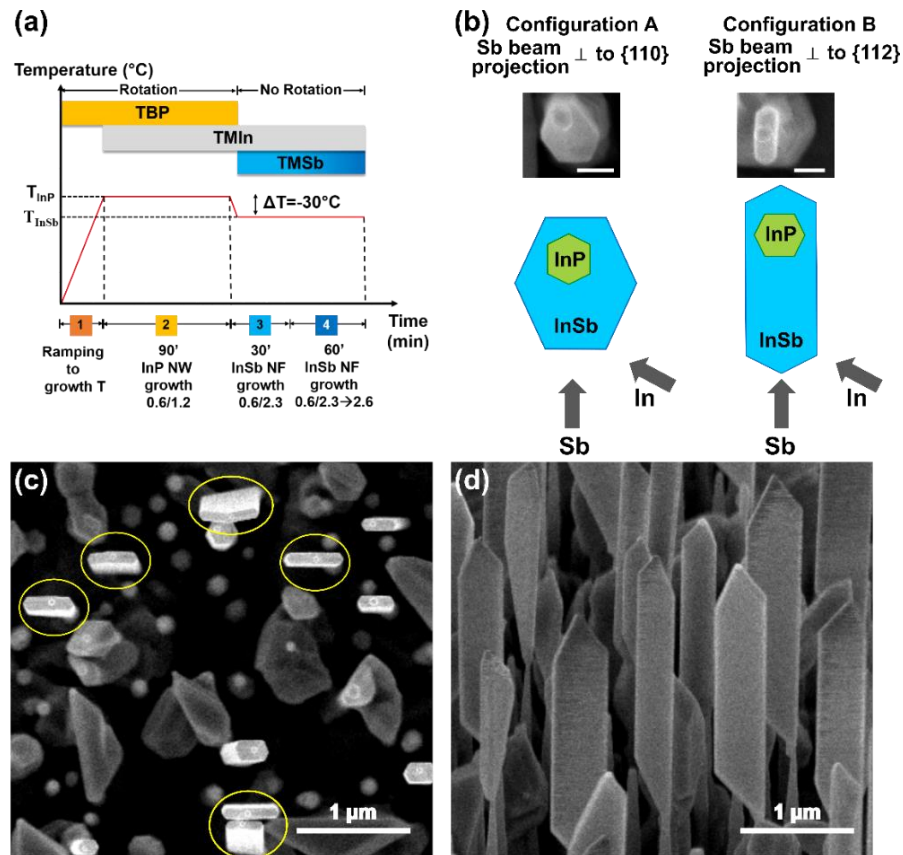

Figure 4.5: Growth and orientation protocol of InSb NFs. (a) Schematics of the growth protocol developed for obtaining InSb NFs. (b) Top-view schematics of the precursor beam

projection with respect to the InP−InSb heterostructure cross-section (bottom) and corresponding SEM images after the first 30 min of InSb growth (top) in the two possible configurations: configuration A with the Sb beam projection perpendicular to a {110} plane, and configuration B with the Sb beam projection perpendicular to a {112} plane. The scale bar is 100 nm. (c) Top view and (d) 45°- tilted SEM image of the InSb NFs obtained in configuration B (scale bar: 1 μm). The InSb NFs which have (W/T) ≥ 4 are marked by yellow circles in panel c.

As aforementioned, before initiating the growth of InSb NFs the substrate rotation was stopped, and the orientation of the NWs was carefully adjusted with the help of the RHEED pattern. Orientation choices are illustrated in panel b of Figure 4.5: the InP NW (represented in green) exhibits a hexagonal cross-section with six equivalent {112} sidewalls. The InSb segments (shown in blue) still have a hexagonal cross-section but with six equivalent {110} sidewalls. A schematic top view of InP−InSb heterostructures is shown for two orientations: configuration A and B. In configuration A, the Sb beam flux projection is perpendicular to a {110} sidewall of the InSb NWs, while in configuration B, the Sb beam projection is perpendicular to a {112} InP NW sidewall. We found that the growth in configuration A leads to thicker InSb NFs, while the growth in configuration B results in thinner NFs for the same growth time. This is explained by considering that the growth of the InSb segment involves two growth mechanisms that simultaneously occur: the VLS axial growth on top of the NW stem and the VS radial growth that is enhanced by high Sb flux [88]. If the sample was rotated, the radial growth would be uniform on the six {110} facets, and we would obtain InSb NWs with symmetric cross-section, showing six sidewalls equivalent in width. Conversely, when we stop the sample rotation and align the substrate in configuration B, there are only two {110} facets facing the Sb injector, that is, reached by direct impingement, so the growth rate on these two facets will be higher compared to the other four sidewalls, and we obtain thinner flags. On the other hand, when the sample is oriented in configuration A, only the three backside InSb facets (opposite to the Sb beam) are totally screened from Sb impingement, while the sidewall perpendicular to the Sb beam projection will receive the direct beam, and the two adjacent inclined facets will be reached by the beam at grazing incidence. So, the NFs will be larger and less elongated. Therefore, once we found the ⟨110⟩ direction with the help of the RHEED pattern at the end of the InP NWs growth (as shown in Figure 4.4), we rotated the substrate by 30° (i.e., to configuration B) and started the InSb growth.

Panel c and d of Figure 4.5 show the top view and 45°-tilted SEM images of a sample grown in configuration B. The yield of the NFs, that is, nanostructures showing a width-to-thickness ratio (W/T) ≥ 4 (marked with yellow circles in panel c) is 40%, and they have an average length, width, and thickness of (2.8 ± 0.2) μm, (470 ± 80) nm, and (105 ± 20) nm, respectively. With the appropriate parameters (growth temperature and precursor fluxes), robust InP stems, and precise substrate orientation, we could grow the InSb NFs for a longer time, obtaining larger InSb NFs with similar thickness, compared with the InSb NFs obtained on InAs NW stems [88]

(compare Figure 4.1 and Figure 4.5 panel c and d), which are suitable for making electronic devices, as demonstrated later.

Furthermore, to improve the morphology and hence obtain wider NFs, the growth temperature of InP was decreased by 20°C i.e. at $T_{InP} = 380$°C, keeping constant $\Delta T = -30$°C, in comparison to the NFs shown in Figure 4.5 panel c and d. Lower growth temperature enhances radial VS growth while suppressing VLS axial growth. This allows to modify axial and radial growth rates resulting in InSb NFs that are (2.0 ± 0.1) μm long, (660 ± 165) nm wide, and (130 ± 17) nm thick (as shown in figure 4.6). The yield of the as-grown NFs decreases because of low growth temperature, but the yield of NFs with merit ratio W/T $\geq$ 4 increases up to 53% which is higher than NFs shown in figure 4.5.
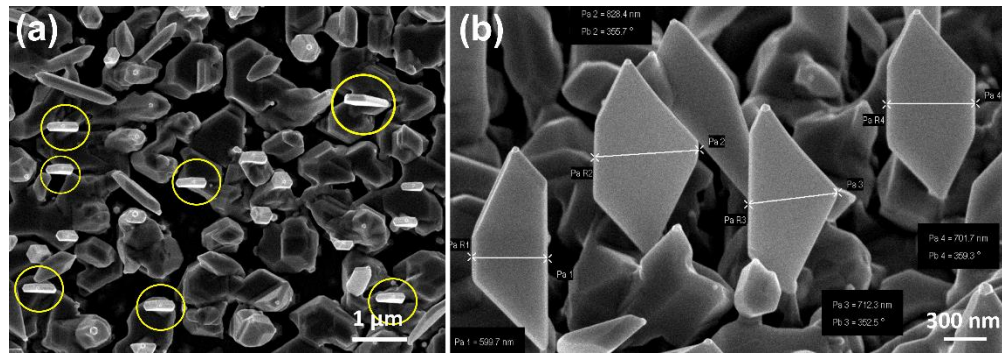

Figure 4.6: (a) Top view and (b) 45°-tilted SEM image of the InSb NFs obtained by decreasing overall growth temperature of InP-InSb heterostructure system by 20°C in comparison to NFs shown in figure 4.5. Scale bar in (a) and (b) is 1μm and 300 nm, respectively. The InSb NFs have (W/T) $\geq$ 4.

Another way to obtain much wider free-standing InSb NFs with respectable yield is to exploit our knowledge derived from the growth optimization of InSb NW on InP stems shown in figure 4.3. We observed a higher yield for InSb NWs for TMIn/TMSb = 0.6/1.2 with respectable aspect ratio. The InSb NFs are grown for 90 min with flux ratio TMIn/TMSb = 0.6/1.2 at $\Delta T = -30$°C. The resulting NFs have an average length, width, and thickness of (1.5 ± 0.2) μm, (410 ± 50) nm, and (117 ± 12) nm, respectively. Keeping lower TMSb flux leads to a lower aspect ratio and to counterbalance this problem, an additional step of 60 min keeping the same flux ratio is added with InSb temperature ramp of 0.5°C/min to have control on the morphology of the NFs. The growth protocol is shown in figure 4.7 panel (a). As a result, we succeed in growing InSb NFs that are (2.9 ± 0.3) μm long, (850 ± 190) nm wide, and (200 ± 25) nm thick, as shown in figure 4.7 (b) and (c). The yield of NFs with (W/T) $\geq$ 4 is 73% for this sample.

The point to note is that by changing any growth parameter, whether adjusting TMIn and TMSb fluxes or growth temperature, we can play with axial (length) and radial (width and thickness) growth rates. The width and thickness growth rates are coupled and hence we have wider but thicker NFs. This poses a problem in the fabrication of InSb-based devices as contact deposition and lift-off procedures get tricky with the increased thickness of NF. To understand the growth

mechanism and shape evolution of these NFs, we propose a growth model described in chapter 5.
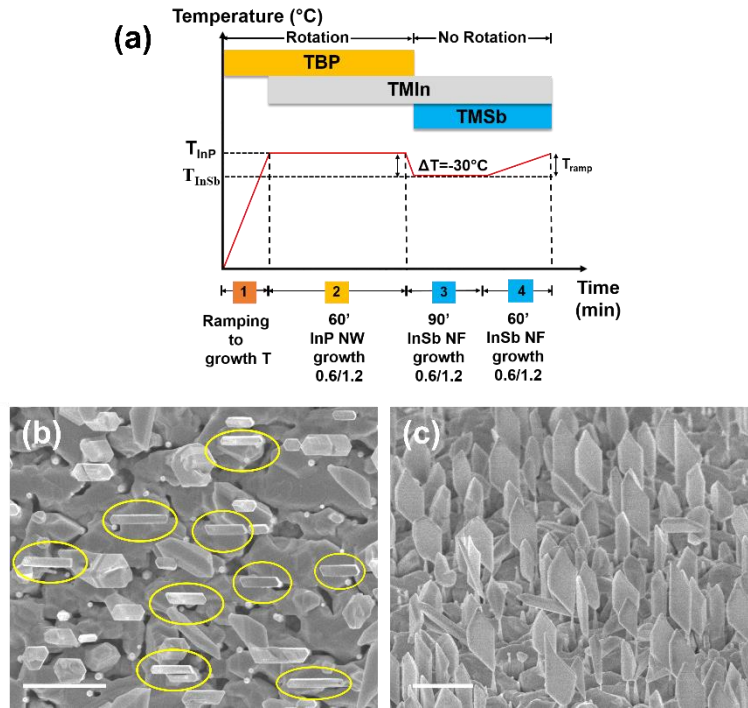

Figure 4.7: (a) Schematics of the growth protocol developed for obtaining InSb NFs. (b) Top view and (c) 45°- tilted SEM image of the InSb NFs obtained in configuration B (scale bar: 2 μm). The InSb NFs which have (W/T) ≥ 4 are marked by yellow circles in panel b.

4.4 Characterization of InSb NFs

4.4.1 Crystal structure

To determine the crystal quality of the NFs, their structure was analyzed by TEM (Figure 4.8). A STEM- HAADF overview of a single InSb NF with a short segment of its InP stem and the catalyst particle at the tip is shown in Figure 4.8a. The corresponding HRTEM images acquired at the three NF corners (purple-, green-, and yellow-framed panels) show the defect-free InSb ZB lattice. The lattice spacing and the interplanar angles (see also the FFT in Figure 4.8b) match those of relaxed ZB InSb (JCPDS card 6-208). The analysis of the NFs faceting confirms the indexing observed in our previously grown samples described in detail in ref 88. The major flat facets are of the type $(10\bar{1})$ and $(\bar{1}01)$, bordered by sides parallel to three pairs of directions: $[\bar{1}0\bar{1}]$ (dashed arrows), $[\bar{1}2\bar{1}]$ (dotted arrows), and $[\bar{1}\bar{1}\bar{1}]$ (solid arrows, aligned with the growth axis).

At the NF tip, a sharp interface between InSb and the metal alloy seed particle is observed (Figure 4.8c). EDX spectroscopy performed in STEM spot mode on several NFs allowed us to identify the metal alloy components as Au and In and to quantify an atom gold content of 34 ± 2%, consistent with $AuIn_2$.
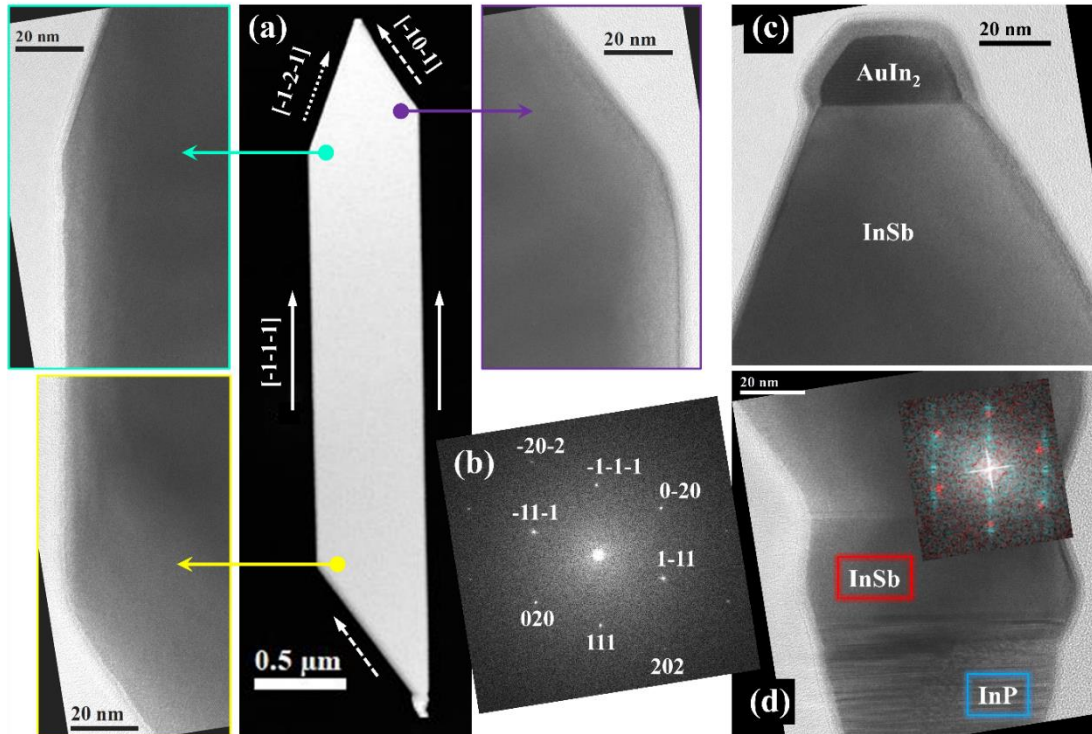
Figure 4.8: (a) STEM-HAADF image and corresponding HRTEM images acquired at the NF corners in $[10\bar{1}]$ zone axis; (b) indexed FFT of the HRTEM image framed in yellow in panel (a). (c,d) HRTEM images were acquired at the NF tip and base, respectively. The inset to (d) shows the FFT obtained by color mixing the FFTs of a small square region in InP (blue color) and InSb (red).

At the NF base, both an axial and radial growth of InSb on InP are observed, as shown in Figure 4.8d and in Figure 4.9. As seen in these HRTEM images, the InP crystal structure is highly defected with a mixed WZ/ZB stacking. Indeed, the energetic differences for hexagonal or cubic stacking sequences in the $\langle 111 \rangle$ direction are very small [101]. As a consequence, stacking faults easily occur in InP NWs vertically grown on (111)B substrates, resulting in NWs with alternating WZ/ZB segments [99]. The radially grown InSb, which was observed to be either asymmetric or symmetric around the InP stem, as shown in Figure 4.9 from panels a-c, also appears defected, showing several stacking faults and twins in its ZB lattice long the stem length. On the contrary, the axially grown InSb shows such a defected structure only in its initial layers, but after the first 10 nm the stacking becomes regular and a perfect ZB structure is recovered. After that, only a twin is observed occasionally within the first 50 nm (as shown in Figure 4.9a,c). FFT analysis performed on the axial InSb close to the InP interface (Figure 4.8d, indicated in red with respect to the blue InP) shows that it reaches a complete relaxation. EDX maps (as shown in Figure 4.9) confirm the purity (50 at% each for indium and antimony) and homogeneity of InSb.
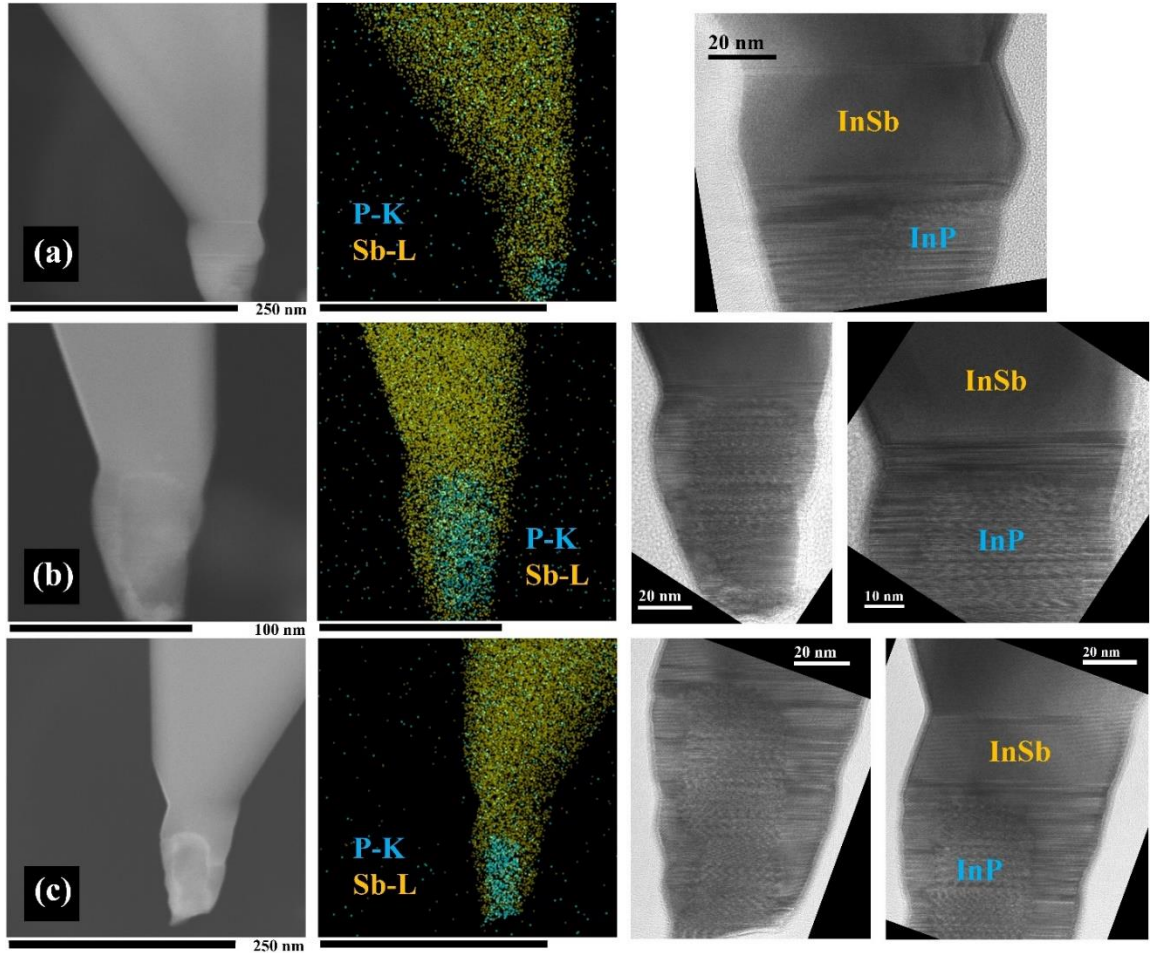
Figure 4.9: (a-c) EDX and HRTEM analysis of the basal region of three representative nanoflags, showing both axial and radial growth of InSb on the InP NW stem. From left to right: STEM-HAADF image, corresponding EDX map of the Sb (dark yellow) and P (blue) distributions, and HRTEM images of the interface.

4.5 Electronic properties of InSb NFs

4.5.1 Four-probe measurements

To investigate the electronic properties of the InSb NFs, we performed low-temperature (at 4.2 K) magnetoresistance measurements on Hall-bar devices. A SEM image of a representative Hall-bar device is shown in Figure 4.10a. Figure 4.10b shows current−voltage (I_{SD}−V_{SD}) curves of the source-drain (S-D) channel at 4.2 K as a function of back gate voltage V_{BG}. The linear I_{SD}−V_{SD} curves together with the low resistance values indicate the presence of good Ohmic contacts between the InSb NFs and the metal contacts, and the absence of a Schottky barrier. Increasing the back gate voltage, the source drain resistance $R_{SD} = V_{SD}/I_{SD}$ decreases from 25 kΩ for $V_{BG} = 10$ V to 2.7 kΩ for $V_{BG} = 50$ V. In a measurement under constant AC voltage bias of 1 mV at 4.2 K, the variation of the injected current as a function of back gate voltage was measured and is shown in Figure 4.10 c. A voltage bias is necessary here since in the depletion

region (negative gate voltages), the sample is insulating and a constant current could not flow. In other words, in the range of back gate voltages that we explored, we did not observe ambipolar behavior. The longitudinal voltage drop V_{xx} is measured simultaneously in a four-probe configuration. We performed back gate sweeps for both V_{xx} contact combinations [(1−2) and (3−4)], and both showed consistent results.
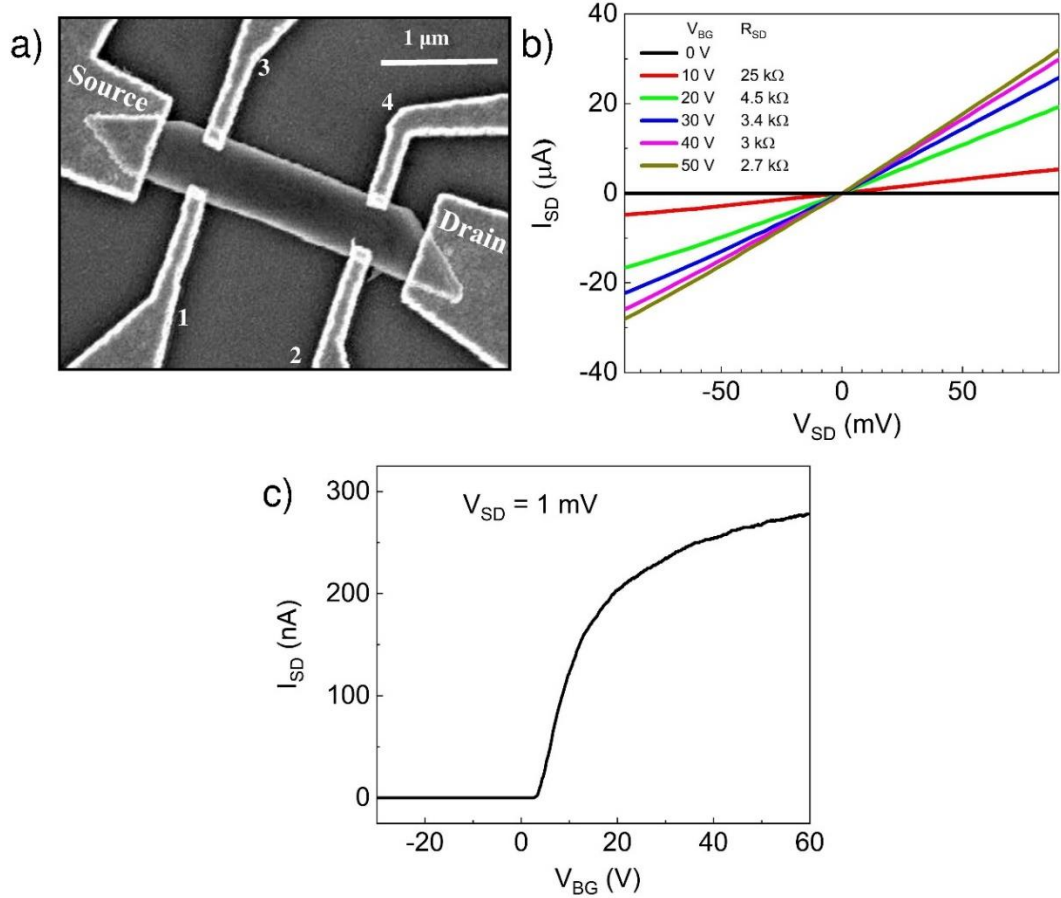
Figure 4.10: (a) SEM image of an InSb NF Hall-bar device with corresponding numbers for Hall-bar contacts. (b) Two-probe I_{SD}−V_{SD} curves as a function of back gate voltage V_{BG}. (c) Source-drain current versus back gate voltage, measured under 1 mV constant AC voltage bias. All measurements are performed at a temperature of 4.2 K.

This allows calculating the conductance $G = I_{SD}/V_{xx}$ as shown in Figure 4.11. The four-probe field effect mobility is then obtained using the formula:

$$\mu_{4p\,FE} = \frac{L}{WC_{ox}}\left(\frac{dG}{dV_{BG}}\right) \tag{4.1}$$

with L/W = 4.6 and C_{ox} = 10 nF/cm². The four-probe field effect mobility obtained is 28000 cm²/Vs. The charge carrier modulation shows an increasing conductance with increasingly

positive back gate voltage, consistent with an n-type behavior of the InSb NFs and in agreement with the data shown in Figure 4.10b.
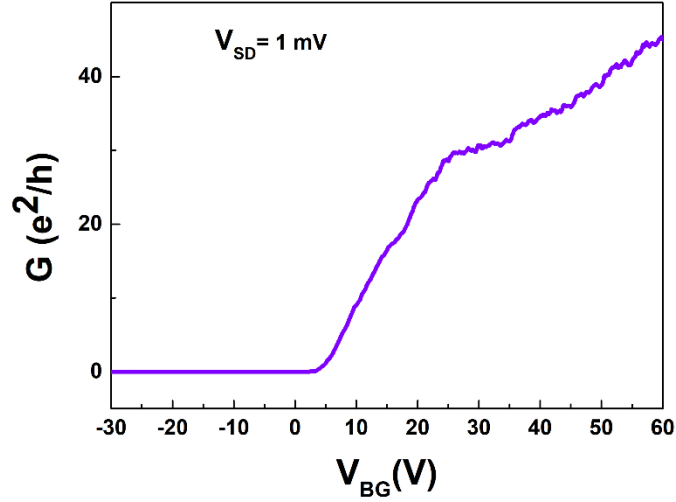
Figure 4.11: Conductance G versus back gate voltage. The measurement was performed at a temperature of 4.2 K.

4.5.2 Hall-effect measurements

In addition to field-effect measurements, we performed low-field Hall measurements on the same InSb- based devices shown in panel (a) Figure 4.10, with the channel width (width between contacts 1-3 and 2-4) of 325 nm and the channel length (1-2 and 3-4) of 1.5 μm. The NF thickness is ~100 nm. The Hall-effect measurements were performed using a constant AC bias of 100 nA at 4.2 K. Since these measurements were performed in current bias, they start at a back gate voltage of 15 V at which the channel is already well open. Figure 4.12a shows the resulting Hall- voltage curves as a function of magnetic field for different back-gate voltages V_{BG}. The corresponding charge-carrier densities and Hall-mobilities for various back-gate voltages are shown in Figure 4.12b.

Hall mobility increases with increasing back gate voltage and shows a maximum of about 29500 $cm^2/(V\ s)$ at $V_{BG} = 25$ V, with a corresponding electron density of $8.5 \times 10^{11}\ cm^{-2}$. For even higher carrier concentrations, mobility slightly drops again due to additional carrier scattering induced by Coulomb interactions. Hence, Hall mobility is in good agreement with the four-probe field effect mobility, and higher than in previous studies, [47, 84, 85] which reported at most 20000 $cm^2/(V\ s)$. We attribute this higher mobility to the fact that our flags are slightly thicker (100 nm) than the flakes reported previously that ranged from 50 to 80 nm, which reduces the contribution of surface- and interface-scattering. Figure 4.12b also shows that charge-carrier density increases with increasing back-gate voltage, as expected.

Furthermore, we estimated the electron mean free path λ_e, using $\lambda_e = (\hbar\mu/e)(2\pi n)^{1/2}$, Ref 102, with $\hbar$ the reduced Planck's constant and n the 2D electron density from the Hall measurements

(cf. Figure 4.12b). As shown in Figure 4.12c, λ_e reaches values of ~500 nm for $V_{BG} \geq 25$ V, which compares favorably with the literature [47,51, 85].
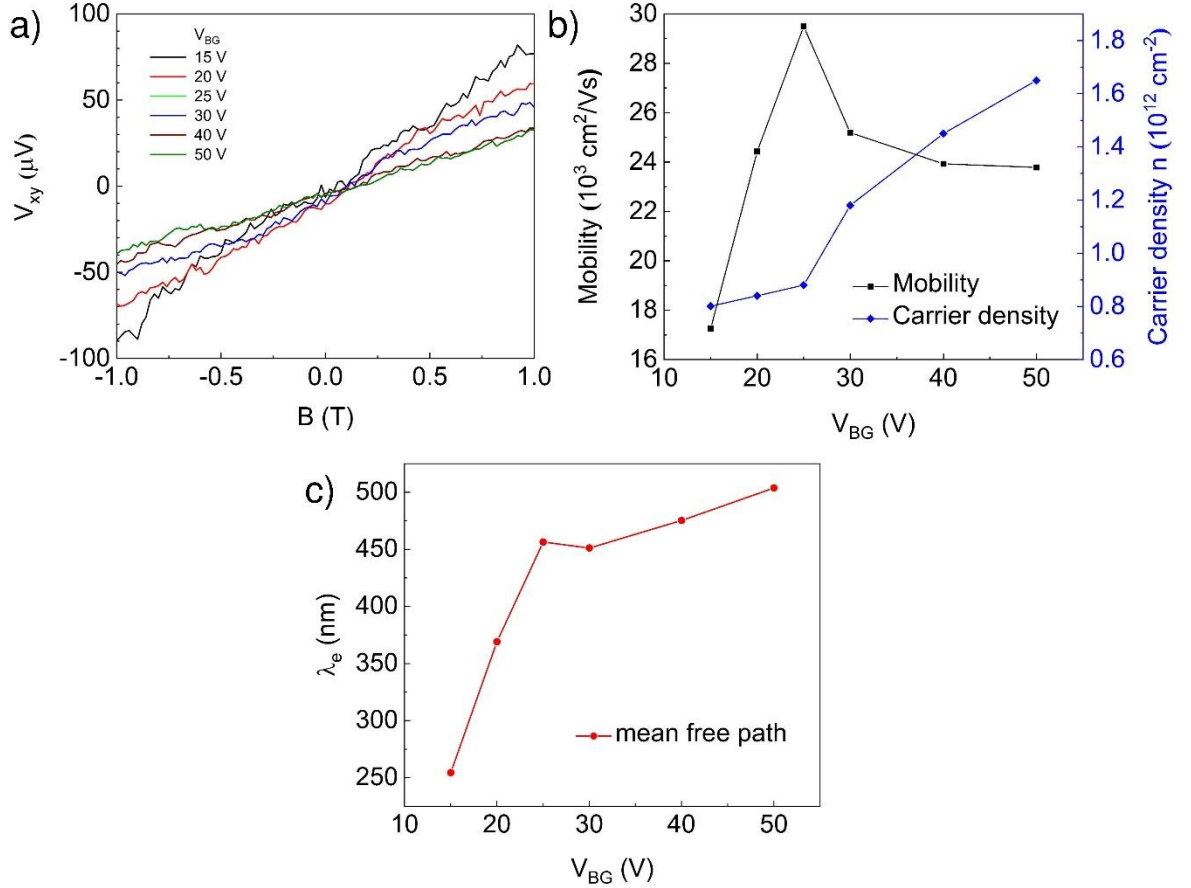
Figure 4.12: (a) Hall measurements on InSb NFs: V_{xy} as a function of magnetic field B for different back gate voltages V_{BG} at 4.2 K. (b) Mobility and charge carrier density obtained from the Hall measurements shown in (a). (c) Elastic mean free path λ_e as a function of back gate voltage V_{BG}.

We measured the Hall voltages as a function of magnetic field ranging from -1T to +1T under constant AC bias of 100 nA for different back gate voltages. An example in Figure 4.13 shows V_{xy} for $V_{BG} = 40$ V. The figure shows the forward and backward sweep of the magnetic field, to demonstrate the reproducibility of the measurement, plus the fit to the experimental data, from which the carrier concentration is obtained. In detail, carrier concentration n and Hall mobility μ_H for each back gate voltage is calculated using the formulas:

$$\mu_H = \frac{L}{W \langle V_{xx} \rangle} \left(\frac{V_{xy}}{B} \right) \qquad (4.2)$$

$$n = \frac{1}{e} \left(\frac{B}{V_{xy}} \right) \qquad (4.3)$$

with e the elementary charge.
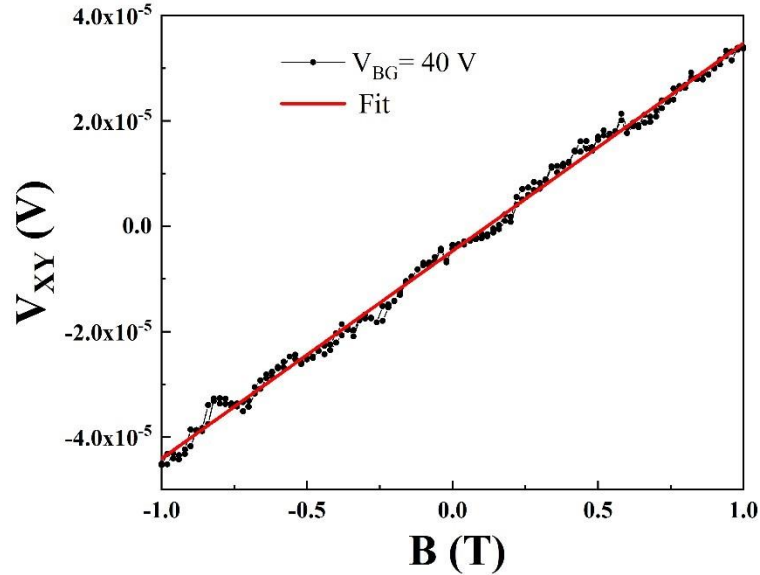
Figure 4.13: The transversal voltage drop V_{xy} as a function of magnetic field B at $V_{BG} = 40$ V and T = 4.2 K.

4.6 Conclusions

In conclusion, we have realized free-standing 2D InSb NFs on InP NW stems exhibiting the electron mobility of about 29500 $cm^2/(V\ s)$ at $V_{BG} = 25$ V, with a corresponding electron density of $8.5 \times 10^{11}\ cm^{-2}$, which is highest compared to other similar 2D InSb nanostructures reported in the literature. The electron mean free path reaches values of ~500 nm for $V_{BG} \geq 25$ V. This was possible by carefully choosing a robust supportive stem, tapered InP NWs, by optimizing the growth parameters leading to the growth of InSb NWs with high yield and high aspect ratio, and by aligning the samples with RHEED in the direction that maximizes the NF elongation keeping the NF thickness at a minimum. This strategy allowed us to obtain InSb NFs of (2.8 ± 0.2) μm length, (470 ± 80) nm width, and (105 ± 20) nm thickness with defect-free ZB crystal structure, stoichiometric composition, and relaxed lattice parameters. In addition, we speculate that similar morphologies might be achieved by adopting this directional growth approach for other materials if they show a consistent radial growth together with the axial elongation. We were further able to obtain larger InSb NFs that are (2.9 ± 0.3) μm long, (850 ± 190) nm wide, and (200 ± 25) nm thick by exploiting our knowledge derived from the growth optimization of InSb NW on InP stems. We also observe that the width and thickness growth rates are coupled and to have wider but thinner is very difficult. We strongly believe that these NFs can serve for the realization of exotic bound states at the semiconductor interface with superconductors, paving the way for the development of topological quantum computation technologies.

Chapter 5: Growth modeling of InSb nanoflags

5.1 Introduction

In the previous chapter, we have described the realization of free-standing 2D InSb NFs on InP NW stems exhibiting superior electronic properties. In fact, InSb NF-based devices have been proven appropriate for studies of novel quantum phenomena, the development of scalable topological superconducting devices based on strong spin−orbit coupling [103-105], and infrared (IR) photodetectors exhibiting a broad spectral detection range [106]. These devices require high crystal quality and dimensional precision. Therefore, a deep understanding of the growth mechanisms and the morphology evolution of such NFs is crucial. Growth modeling is also fundamental for the controlled growth of NFs with the desired morphological properties and crystal structure, similarly to the growth theory of III-V NWs [33, 107-115]. However, due to the complexity of the NF morphology, detailed growth modeling has not been achieved so far.

Recently, Gazibegovic et al [85] and De La Mata et al [47] reported that a single twin plane drives the crystal to change its geometry and expand, leading to 2D NF morphology, while Pan et al [84] attributed the NF formation mechanism to a combination of the VLS axial growth and the VS lateral growth. However, the main focus of these works was more in tailoring the growth parameters to obtain the maximized lateral dimension, rather than in understanding the morphology evolution of the NFs.

In this chapter, we discuss the growth mechanisms of InSb NFs in more detail. We analyze the shape evolution of Au-catalyzed InSb NFs on InP NW stems grown in regular arrays on lithographically patterned InP(111)B substrates using a combined SAE growth and VLS growth. We propose a model describing the InSb NF growth and morphology as a function of the time and pitch of the NW/NF array. By fitting the experimental data, we can deduce the most important parameters influencing the width and thickness of InSb NFs. The modeling presented in this work is done in collaboration with Prof. Vladimir G. Dubrovskii from the Faculty of Physics, St. Petersburg State University, Russia. The results presented in this chapter are submitted to MDPI Nanomaterials.

5.2 Experimental details

The InP-InSb NFs of the present study were grown on InP (111)B substrates via Au-assisted SAE growth. A 20 nm-thick sputtered SiO_2 was used as a mask on InP (111)B to suppress the parasitic growth on the substrate surface. The openings in the SiO_2 mask were made by wet etching (HF) on hexagonal arrays of the lithographically patterned substrate with different spacing in the horizontal direction, which we refer to as the pitch a, followed by 6 nm-thick Au evaporation and lift-off. This resulted in a hexagonal array of Au discs of 30 ± 3 nm in diameter, inside the SiO_2 mask openings of 153 ± 7 nm in diameter, positioned at a fixed distance (200

nm) in one direction, and different pitches from 500 nm to 1500 nm in the other (perpendicular) direction. The corresponding range of Au disc density varied from 3.6 to 12.3 μm^{-2}. These Au discs catalyzed the CBE growth of NWs and NFs. TMIn, TBP, and TMSb were used as MO precursors.

InP NW stems were grown for 60 min under TMIn and TBP line pressures of 0.6 and 1.2 Torr respectively, at a growth temperature T_{InP} of 405° ± 5°C, as measured by a pyrometer. For InP NW growth, the sample was rotated at 5 rpm. The InSb segments were grown on top of these InP stems without rotation of the substrate. The alignment of InSb NFs was achieved using the RHEED pattern, following the same procedure as reported in Ref. 100. The substrate was aligned in such a way that the pitch direction is parallel to the projection of the Sb beam. Afterward, the substrate temperature was ramped down under TBP flux, to the optimized InSb growth temperature (ΔT=-40°C with respect tod T_{InP}).

For initiation of InSb growth, group V flux was abruptly switched from TBP to TMSb. InSb NFs were grown at a constant temperature, a TMIn line pressure of 0.6 Torr and TMSb line pressure of 1.2 Torr, for different times. At the end of growth, the samples were cooled down to room temperature in UHV environment in the absence of group V flux, to prevent the accumulation of Sb on the sidewalls of InP-InSb heterostructures.

5.3 Results and discussion

5.3.1 SA growth of InP-InSb heterostructures

In order to study the effect of the pitch on the morphology of InP-InSb heterostructured NFs, we fabricated many patterns with different pitches (a) on the same substrate. Hence, the same growth occurred simultaneously on the patterns with different densities of Au discs corresponding to the pitches of 500, 700, 900, 1100, and 1500 nm. Using SEM images, we measured the L, W, and T of InSb NFs obtained on the patterns with different pitches and after different InSb deposition times t.

Figure 5.1 (a) shows a top-view SEM image of a patterned substrate with a 700 nm pitch. InP NWs were grown in a regular array on the lithographically defined substrate as shown in Figures 5.1 (b) and (c). These NWs have a length of 1.2 ± 0.1 μm, a tip diameter of 46 ± 5 nm, a base diameter of 238 ± 35 nm, and an Au NP diameter of 38 ± 2 nm. The dimensions mentioned are the average values and the standard deviations. InSb NFs were grown on top of the InP NW stems. The top view and 45°-tilted SEM images of InSb NFs are shown in Figures 5.1 (d) and (e), respectively. Figure 5.1 (f) shows the magnified image of a representative NF.

It is worth mentioning that even with the use of SiO_2 mask for SA CBE growth, nucleation and growth of parasitic islands is observed on the mask surface for all growth times. We assume this to be due to a non-perfectly homogeneous SiO_2 layer. However, the yield of NWs or NFs is not compromised.
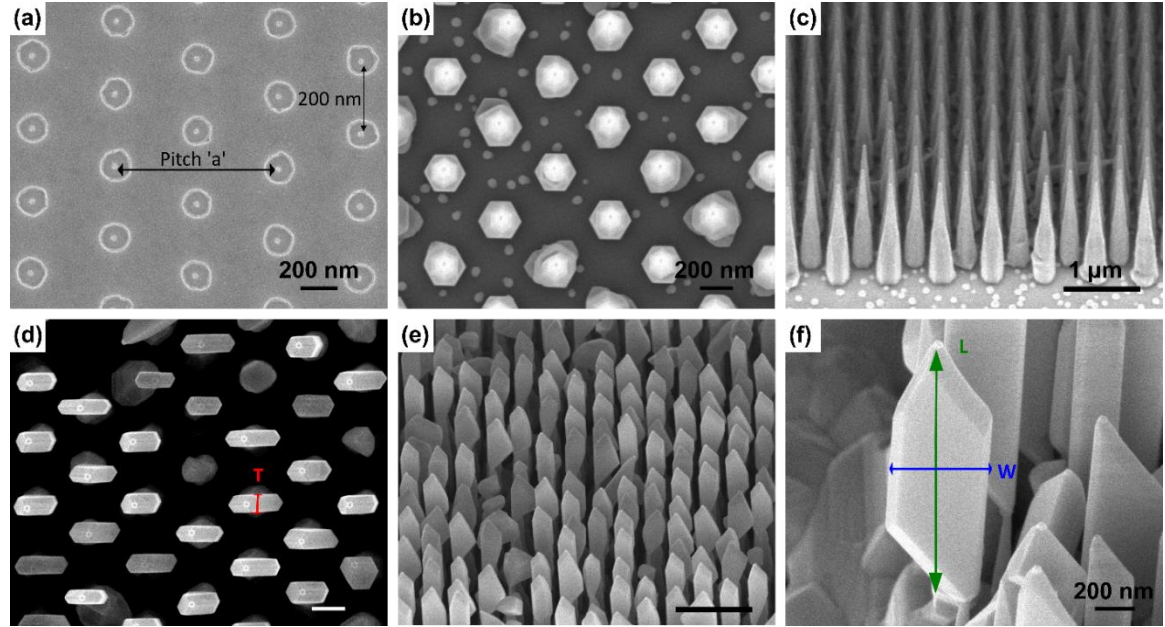
Figure 5.1: (a) Top-view SEM image of a lithographically patterned InP(111)B substrate with 20 nm-thick SiO_2 mask and Au discsThe scaleng a pitch a of 700 nm. Scale bar is 200 nm. (b) Topimages and (c) 45°-tilted SEM image of InP NW stems grown on the substrate shown in panel (a) for 60 min. (d) Top-view and (e) 45°-tilted SEM image of InP-InSb heterostructured NFs obtained after 60 min growth of InSb. (f) Magnified 45°-tilted SEM image of an individual InSb NF. Panels (d) and (f) show the measured geometrical parameters of InSb NFs. Thickness T was measured using top-view images, width W and length L were measured using tilted images and corrected by the geometrical factor due to the tilt angle. Scale bars in (b), (d), (f) and (c), (e) are 200 nm and 1μm, respectively.

5.3.2 InSb NF evolution with time and pitch

The measured dependences of the L, W, and T of InSb NFs on the pitch are shown in Figure 5.2 for InSb growth times of 30 min, 60 min, and 90 min. Shorter NF lengths are systematically observed for smaller pitches regardless of the growth time. Lower growth rates of the length for smaller pitches should be due to shadowing or competition between the neighboring NFs for the material flux. Above a certain threshold, corresponding to a pitch of 700 nm, the lengths become almost independent of the pitch, indicating no competition for larger pitches. The NF length evolution can be qualitatively explained by considering the In-limited VLS axial growth rate containing two contributions: (1) the direct impingement and (2) In adatom diffusion on the NF sidewalls. Surface diffusion of In adatoms from the substrate surface can be safely neglected because the InP NW stem is around 1.2 μm long. According to Figure 5.2 (a), the length growth rate is higher (around 28 nm/min) for the shortest growth time of 30 min, and decreases to nearly 15 nm/min for 60 min and 90 min. The direct impingement is constant throughout the InSb growth, hence a faster elongation at the beginning of growth can be associated with a larger diffusion flux of In adatoms probably from both InP and InSb sidewalls. The latter is characterized by an effective diffusion length λ_{In}. When the length of the InSb

segment becomes greater than λ_{In}, the contribution from surface diffusion decreases [108]. The diffusivity of In adatoms on the InSb sidewalls is expected to be very low due to significant radial growth. Therefore, after a certain critical length, the axial growth rate is limited by the direct impingement of In atoms and independent of the growth time.
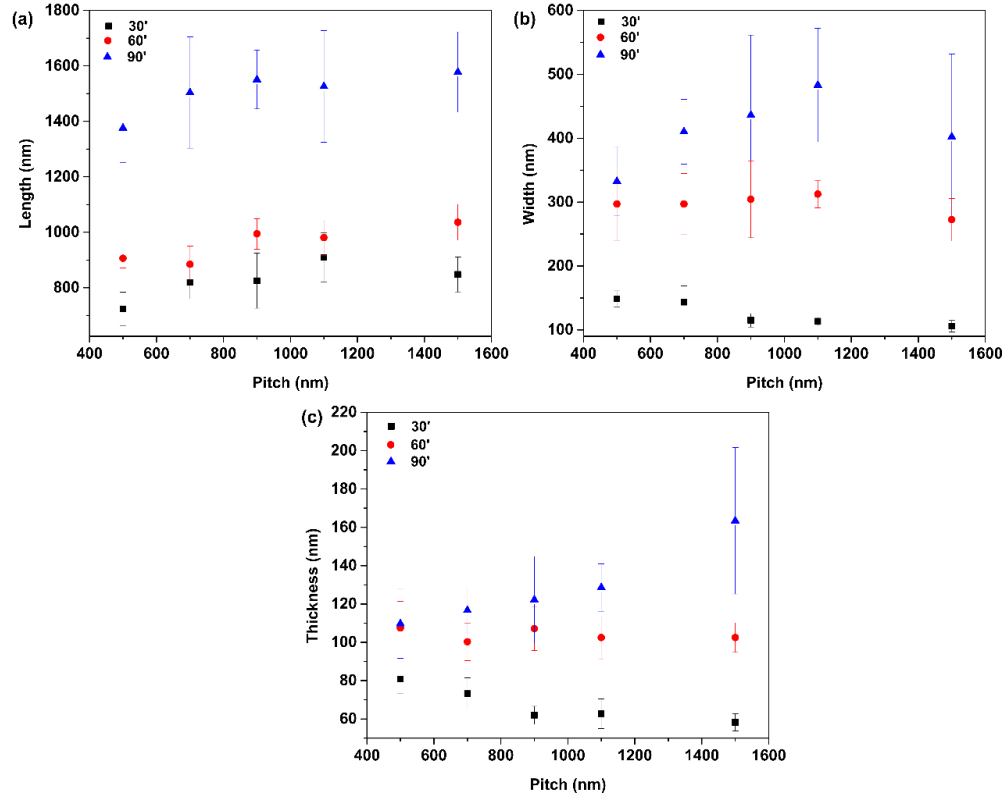
Figure 5.2: Dependences of (a) length, (b) width, and (c) thickness of InSb NFs on the pitches for 30 min (black squares), 60 min (red circles), and 90 min (blue triangles) InSb growth times.

The VS radial growth rate of the InSb NFs, which controls the NF width and thickness, is 10 times lower than the VLS axial growth rate. According to Figures 5.2 (b) and (c), *W* and *T* show a dependence on the pitch and growth saturation above the threshold pitch as in the case of *L* (Figure 5.2 (a)). Unlike for the length, the trend is different for different growth times. In fact, for shorter InSb growth times (black squares for 30 min), the radial growth is higher for smaller pitches (500 and 700 nm) than for larger ones (> 700 nm). For longer growth times (red circles for 60 min and blue triangles for 90 min), the trend is inverted, that is, lower radial growth rates are observed for smaller pitches. Overall, the scattered data can be better understood if replotted as functions of time, as in Figures 5.3 (a) and (b). It can be seen that the VS growth rate of thickness and width is more sublinear for the smallest pitch of 500 nm, in which case the thickness is almost constant after 60 min. For the largest pitch of 1500 nm, both thickness and width increase almost linearly with time.

5.3.3 Growth model for VS radial InSb NF

To understand these trends, we propose a model which takes into account the direct and re-emitted fluxes of Sb and the shadowing effect [112]. The re-emitted flux originates from the scattering of Sb atoms from the mask surface and NF/NW sidewalls, as in Ref. [116] for As. We assume that (i) a certain amount of Sb atoms will contribute to the width growth at any time from the direct flux; (ii) the re-emitted Sb flux can be almost fully shadowed; (iii) the re-emitted flux is not directional; and (iv) the shadowing effect increases for smaller pitches.
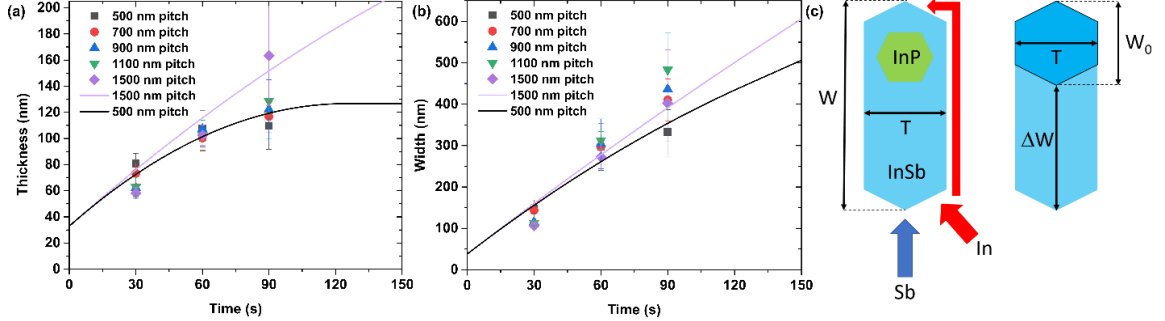
Figure 5.3: (a) Width W and (b) thickness T of InSb NFs versus time for different pitches a shown in the legend. (c) Illustration of the NF geometrical parameters from top-view used in the model. Lines in (a) and (b) show the fits for pitches $a = 1500$ and 500 nm obtained within the model.

The model geometry is shown in Figure 5.3 (c). If the substrate were rotated during growth of NFs, the width W_0 and thickness T would be related simply as $W_0 = (2/\sqrt{3})T$ from regular hexahedral geometry. Without substrate rotation, the width becomes greater,

$$W = \frac{2}{\sqrt{3}}T + \Delta W \tag{5.1}$$

where ΔW is the additional width of a NF due to the direct Sb flux impinging only two of the six side facets (see Figure 5.3 (c)). Diffusive In atoms can reach the back side of the NF by surface diffusion, while Sb atoms can impinge only from re-emitted flux. We can therefore write

$$\frac{dT}{dt} = v_r \tag{5.2}$$

where v_r is the re-emitted flux of Sb atoms. According to Eq. (5.2), the NF thickness increases only due to re-emitted flux, which is not directional but rather originates from Sb vapor surrounding the NFs. Using Eq. (5.2) in Eq. (5.1) along with $d\Delta W/dt = v$, with v as the direct flux of Sb atoms, we obtain

$$\frac{dW}{dt} = \frac{2}{\sqrt{3}}v_r + v \tag{5.3}$$

The re-emitted flux of Sb is shadowed by the neighboring NF/NW structures. The shadowing effect must increase for smaller pitches a and longer growth times t [117, 118]. In the first approximation, the re-emitted flux can be put as

$$v_r = \varepsilon v \left(1 - \frac{kt}{a}\right), \quad \frac{kt}{a} < 1 \text{, or } 0, \quad \frac{kt}{a} \geq 1 \qquad (5.4)$$

where ε gives the ratio of re-emitted over direct flux in the absence of shadowing and k is a constant. The re-emitted flux becomes fully shadowed after a certain time corresponding to saturation of the NF thickness. Using Eq. (5.4) in Eqs. (5.2) and (5.3) and integrating, we get

$$T = T_0 + \varepsilon v t - \frac{k\varepsilon v}{2a} t^2, \ t < \frac{a}{k}; \ \ T = T_0 + \frac{\varepsilon v a}{2k} = T_*, \ t \geq \frac{a}{k},$$

$$W = \frac{2}{\sqrt{3}} T + vt, \ t < \frac{a}{k}; \ \ W = \frac{2}{\sqrt{3}} T_* + \frac{va}{k} + v\left(t - \frac{a}{k}\right), \ t \geq \frac{a}{k}. \qquad (5.5)$$

Lines in Figures 5.3 (a) and (b) show the fits for the largest and smallest pitches, a =1500 nm and 500 nm, obtained from Eqs. (5.5) at $D_0 = W_0$ =38 nm, v =2.4 nm/min according to the data, ε =0.625, and k =4 nm/min. With these fitting parameters, we are able to reproduce the main trends such as saturation of the NF thickness for the smallest pitch and gradual increase of the NF width regardless of the pitch. The fits are not perfect and cannot be better due to the scattered data. However, we can expect that the aspect ratio W/T will increase for longer growth times and that T growth can be decoupled from W growth as soon as the re-emitted flux is completely suppressed, yielding a more pronounced 2D geometry of InSb NFs.

5.4 Conclusions

In conclusion, 2D InSb NFs have been grown by CBE in regular arrays using InP NW templates synthesized on patterned SiO$_2$/InP(111)B substrates. 2D geometry of the NFs has been achieved by stopping the substrate rotation and properly aligning the sample with the impingent beam. A growth model has been presented which allows for a semi-quantitative description of the NF morphology as a function of the growth time and pitch. The pitch-dependent shadowing effect for the re-emitted Sb flux has been identified as the key process influencing the morphological evolution, in particular the with-over-thickness ratio. Overall, these findings can be used for tuning the InSb NF morphology and probably extended to other material systems. More experiments and modeling to access the NF morphology for longer growth times and develop a more detailed understanding of the entire growth process is planned and particularly the regimes corresponding to the highest aspect ratios of the NFs.

Chapter 6: InSb Nanoflag Josephson Junctions

6.1 Introduction

Today a great interest revolves around the possibility to create and manipulate new states of matter with topological properties. This stems mostly from the intrinsic robustness of topological states against local perturbation and the ensuing relevance for quantum computing architectures [22, 23]. Hybrid superconductor-semiconductor heterostructures represent a promising platform in which topological properties can emerge [24].

In this context, InSb has attracted much attention due to its intrinsic properties which are both important requirements for high-speed and low-power electronic devices. Besides 1D NWs, 2D InSb structures also attract great attention, owing to their inherent design flexibility [51, 105, 123]. Indeed, the InSb NFs grown on robust tapered InP nanowires, which did not bend and allowed to grow larger NFs of (2.8 ± 0.2) µm length, (470 ± 80) nm width, and (105 ± 20) nm thickness is large enough to fabricate Hall bars with length-to-width ratios enabling precise electrical characterization [100]. Electron mobility of 29500 cm^2/ (V s) was measured at a carrier concentration n = 8.5×10^{11} cm^{-2} at 4.2 K. The electron elastic mean free path λ_e reached values of 500 nm, which favorably compares with present literature [47, 51, 85].

In this chapter, we report on the fabrication and characterization of Josephson Junction (JJ) devices based on these InSb NFs and provide evidence of ballistic superconductivity. We employ Ti/Nb contacts on InSb JJ devices and show gate-tunable proximity-induced supercurrent at 250 mK and a sizable excess current. The devices also show clear signatures of subharmonic gap structures, indicating phase-coherent transport in the junction and highly transparent interfaces. Our results indicate InSb NF as a promising platform for the study of topological superconductivity. The device fabrication and measurements were performed in collaboration with Dr. Sedighe Salimian and Prof. Stefan Heun at NEST laboratory. The results are published in Ref. [105].

6.2 Experimental details

6.2.1 Measurement setup

All devices in this work were measured in a four-terminal configuration at 250 mK using a ^{3}He cryostat equipped with RC- and π-filters. Signals were registered via room-temperature preamplifiers. In most cases (Figures. 6.1, 6.2, 6.4, 6.5, 6.6, 6.7), data were measured in DC + AC configuration, in which the DC setup allowed to measure I − V curves, while a small AC component was added to the DC bias allowed to measure the differential resistance with a lock-in amplifier, with current excitation in the range 5 − 10 nA. On the other hand, the data shown in Fig. 6.3 were measured just in DC, without the AC component. The differential resistance was in this case obtained by numerical differentiation. Except for Fig. 6.3, all measurements

were performed at a small magnetic field of $B_0 = 6$ mT used to compensate for the residual magnetization of the cryostat.

For the analysis of the experimental conductance traces, we follow the approach of Ref. 24. We calculate the total conductance G of a multimode Josephson junction as the sum of N_i single-mode contributions resulting from the transverse quantization, contained in M families, where modes in each family are characterized by their transmission probability Tr_i [119]. We obtain N_i, Tr_i, and the induced superconducting gap Δ^* by optimizing the numerically calculated conductance to the experimental one by the least-squares fit. M is a free parameter of the fitting procedure and is chosen as the smallest number for which at least one of the parameters Tr_i is zero.

6.2.2 Device fabrication and architecture

To fabricate the devices, the as-grown InSb NFs were dry transferred onto a pre-patterned highly conductive p-type Si(100) substrate, covered with a 285 nm-thick SiO_2 layer, which serves as a global back gate. During the mechanical transfer, the InSb NFs are detached from the InP NW stems, so that well-isolated InSb NFs were found lying randomly distributed on the substrate. The position of selected InSb NFs was determined relative to predefined alignment markers using SEM images. Considering the thickness and the edge geometry of the InSb NFs, electrodes were patterned on a 400 nm thick layer of AR-P 679.04 resist with standard EBL. Before metal deposition, the native oxide was removed using a sulfur-based cleaning method which results also in a smoother InSb surface [10]. To this end, the native oxide was etched for 1 min in an optimized sulfur solution of $(NH_4)_2S_x$ (1:9 $(NH_4)_2S_x$: DI water at 40°C). Then the samples were rinsed in DI water for 30 s. Next, a 10/150 nm Ti/Nb film was deposited with a high deposition rate after an intense pre-sputtering of each target, followed by lift-off in hot acetone.

The panel (a) of Figure 6.1 shows a SEM image of the device investigated in this work. In brief, a 100 nm-thick InSb NF was transferred mechanically on a SiO_2/Si substrate and contacted with 10/150 nm Ti/Nb. The interelectrode spacing between the two superconductors, i.e., the length of the normal (N) region, is L = 200 nm, while its width is W = 700 nm. Standard transport characterization yields a mean-free path of $\lambda_e \sim 500$ nm [100] for the N region, greater than the junction length L. These numbers place the device in the ballistic regime.

6.3 Electronic properties of ballistic Josephson junction devices

To measure the properties of a JJ device, one must cool a sample below critical temperature T_c and apply a magnetic field, electric current, or other stimulus. For this, we had to determine T_c. There are various methods for measuring T_c including resistive, magnetic and thermal methods. The magnetic method requires expensive and complicated superconducting quantum interference device (SQUID) magnetometer or vibrating sample magnetometer (VSM). The thermal method is also complicated as specific heat has to be measured and with high accuracy

which is not good in comparison to magnetic and restive methods. However, resistive method is simpler and more practical than the aforementioned methods.

Therefore, we employed resistive method in which T_c is determined as the mid-point of resistive transition from normal state to superconducting state with a small DC + AC current in zero magnetic field. All the measurements are done on the as-fabricated device as shown in figure 6.1 (a) and is consistent with the data acquired from other two devices.
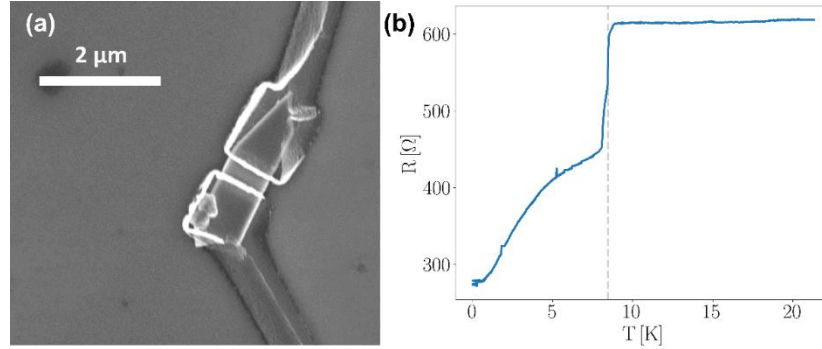
Figure 6.1: (a) SEM image of the Josephson junction device. Scale bar 2 μm. (b) Electrical resistance of the Nb contacts from the device as a function of temperature.

The critical temperature of the superconducting leads was determined to be $T_c = 8.44$ K, from which the bulk gap can be computed using the theory by Bardeen, Cooper, and Schrieffer (BCS) [120]: $\Delta = 1.76k_BT_c = 1.28$ meV, consistent with values of Nb superconducting contacts previously reported in literature [121-127]. The induced superconducting coherence length [51, 128-130] is $\xi_S = \hbar v_F /\Delta$, with v_F the Fermi velocity in the N region ($v_F = 1.5\times10^6$ m/s) and Δ the gap in the superconductor. Here, $\xi_S \sim 750$ nm $> L$, so the device is in the short junction regime. Equivalently, the Thouless energy [129, 131] $E_{Th} = \hbar v_F /L = 4.9$ meV $> \Delta$.
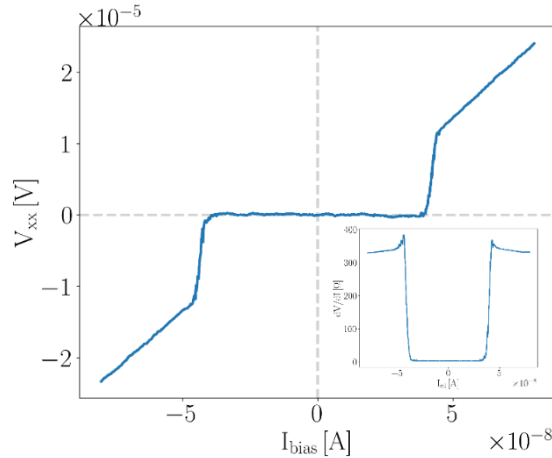
Figure 6.2: DC voltage drop V_{sd} as a function of bias current I_{sd}. A supercurrent of ~ 50 nA is observed. The lower right inset shows the differential resistance dV/dI measured

simultaneously by lock-in technique. V_{bg} = 30 V, T = 250 mK. B = 6 mT applied to compensate for the residual magnetization of the cryostat.

Figure 6.2 shows a typical voltage - current (V −I) characteristics obtained at T = 250 mK and V_{bg} = 30 V. The device displays well-developed dissipationless transport thus demonstrating proximity-induced superconductivity in the InSb NF. As the bias current exceeds the critical value of ∼ 50 nA, a sudden jump in the measured voltage to a dissipative quasiparticle branch is observed, indicating that the JJ switches from the superconducting to the normal state, with a resistance of ∼ 330 Ω. Current sweeps in opposite directions show negligible hysteresis, i.e., switching and retrapping current are the same, so that in the following, we shall use switching current and critical current as synonyms. Consistently, the switching current is larger than the intrinsic thermal current noise δI_{th} of the junction [128, 132] $\delta I_{th} = 2ek_BT/\hbar$; here δI_{th} = 10.5 nA. The lower right inset to Figure 6.2 shows the differential resistance dV/dI measured using a lock-in amplifier together with the V − I curve. Data clearly show that the differential resistance is zero in the supercurrent branch of the device. Zhi et al. report a supercurrent of 20 nA at 10 mK in Nb/InSb NF SNS junctions [128]. We attribute the improved numbers reported here mainly to a higher mobility of the NFs and progress in device fabrication.

Superconducting quantum interference was observed in the dependence of the supercurrent on a magnetic field applied perpendicularly to the sample plane (Figure 6.3). Supercurrent maximum is obtained for B_0 = 6 mT instead of the expected maximum at zero B field. This small offset can be attributed to a residual magnetization in the cryostat. Applying higher or lower magnetic fields, the suppercurrent symmetrically decreases, until for $|B − B_0|$ > 5.2 mT it is suppressed. The modulation of the critical current by quantum interference is one of the hallmarks of the Josephson effect. The shape of the curve resembles a Fraunhofer pattern with only the central lobe, i.e., without side-lobes. We have verified that in a magnetic field range of B ≤ 50 mT, no side-lobes appear. De Vries et al. have studied similar InSb NF JJ and report an even-odd Fraunhofer pattern [51]. Thus, the intensity of the first side-lobes might be anomalously small which precludes their observation in our experiment.

On the other hand, such anomalous magnetic interference patterns, with a monotonous decay, were reported previously in similar geometries [122, 123, 133, 134] and were attributed to geometric factors [122, 133, 135-140]. Besides, the magnetic flux through the junction is Φ = B · A, with A the junction area, A = W (L + 2λ_L) [141]. Here λ_L is the London penetration depth of Nb. Thus, the smaller the channel width W, the higher the value of B required to reach Φ = Φ_0. According to Rohlfing et al., [122] larger values of B more strongly suppress I_c (B) via a dramatic reduction of the amplitude of Andreev reflections. Future measurements on devices with larger W/L ratio might help to clarify whether the missing lobes in Fig. 6.3 are due to geometric factors.
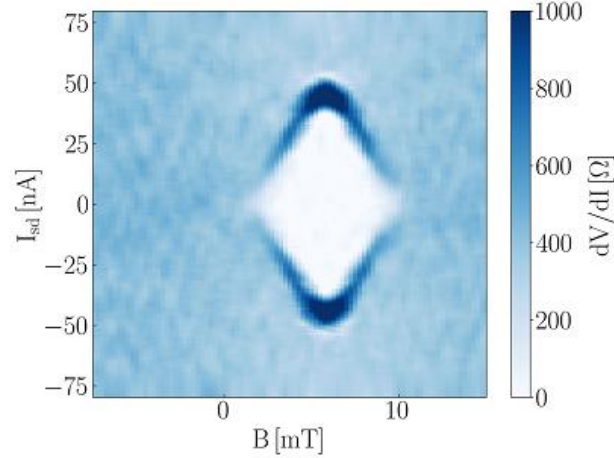
Figure 6.3: 2D colormap of differential resistance dV/dI, obtained by numerical derivation of measured DC V − I curves, plotted vs. current bias I_{sd} and magnetic field B, measured at $V_{bg} = 40$ V and T = 250 mK.
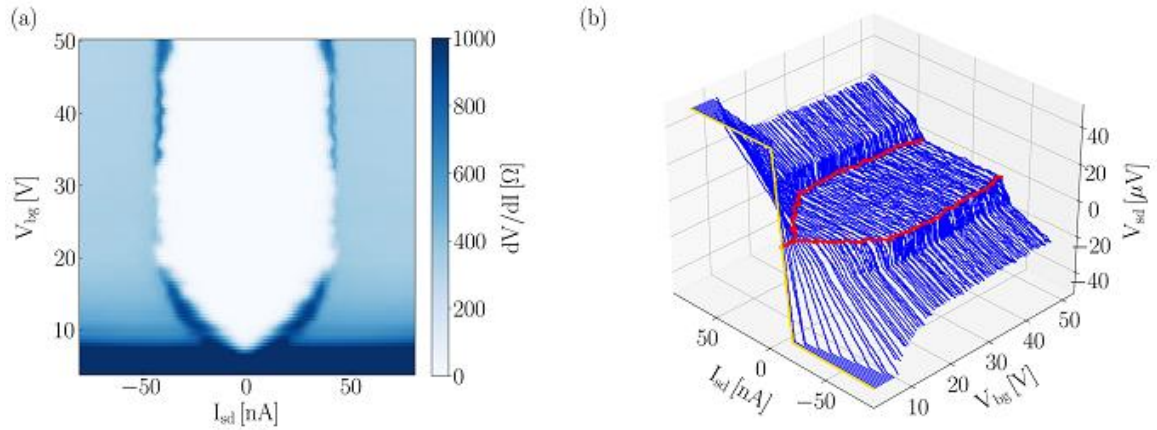
Figure 6.4: (a) Color-scale plot of differential resistance dV/dI, measured by lock-in technique, as a function of current bias I_{sd} and back gate voltage V_{bg}. (b) 3D plot shows the trend of simultaneously measured DC V − I curves at different back gate voltages. The first curve (at lowest back gate voltage) is highlighted in yellow. Red lines indicate the transition between the superconductive and the dissipative regime. The supercurrent increases with increasing back gate voltage above pinch off. T = 250 mK. B = 6 mT applied to compensate for the residual magnetization of the cryostat.

InSb NFs are n-type semiconductors, and the carrier concentration in the NF can be tuned by an applied gate voltage [100]. Figure 6.4(a) shows that global gate modulation can also be employed to control the magnitude of the supercurrent maximum. The figure shows the differential resistance dV/dI of the device as a function of current bias I_{sd} and back gate voltage V_{bg}. The central white region represents the zero- resistance supercurrent branch. In a range of gate voltages from 20 to 50 V, the supercurrent is approximately constant at ∼ 50 nA. Decreasing gate voltage below 20 V, the supercurrent decreases, until it disappears for ∼ 5 V. This demonstrates the gate voltage control of the supercurrent magnitude and that the device

implements a JoFET [142-146]. The corresponding V – I curves as a function of back gate voltage are shown in Fig. 6.4(b) as line plots. While the V − I curve for V_{bg} = 10 V still shows a zero slope at the origin, already for V_{bg} = 7 V the V − I curve is essentially linear with an Ohmic behavior. The gate voltage dependence of the switching current is shown in Fig. 6.4(b) as red line and confirms that below V_{bg} = 20 V the switching current decreases. The normal resistance (the slope of the V − I curves in the normal branch) displays an opposite behavior: below V_{bg} = 20 V it increases significantly, from $\sim$ 330 Ω to above 10 kΩ. The product of switching current and normal resistance, $I_{sw} \cdot R_n$, is approximately constant at 15 μV in a wide range from V_{bg} = 10 V to 50 V (see Fig. 6.5), while it drops to zero when the switching current becomes zero. Similar results were reported by Zhi et al. [128].
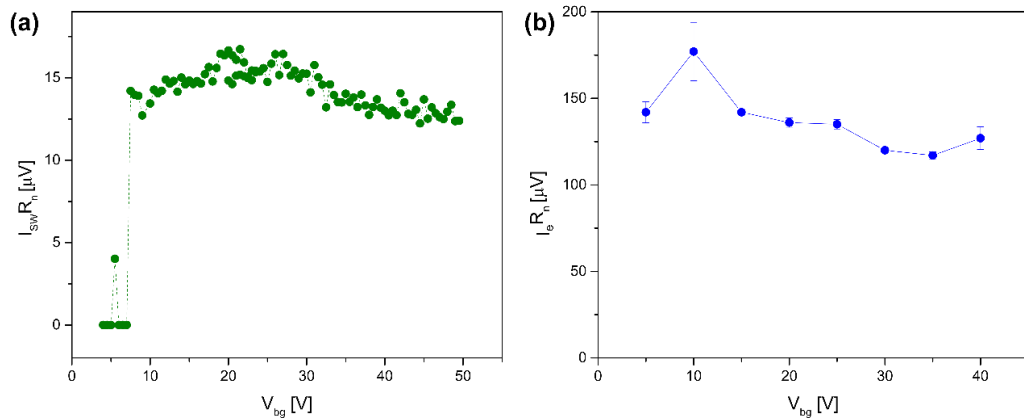
Figure 6.5: (a) Switching current I_{sw} times normal resistance R_n versus back gate voltage V_{bg}, obtained by analysis from the data shown in Fig. 6.3. The product $I_{sw}R_n$ remains nearly constant at 15 μV for a wide range of back gate voltages. (b) Excess current I_e times normal resistance R_n versus back gate voltage V_{bg}. Error bars are the standard deviation of the measured data. The product I_eR_n remains nearly constant at (137 ± 19) μV for a wide range of back gate voltages.

Next, we characterize the dissipative regime. Figure 6.6(a) shows subharmonic gap structures in the differential conductance that can be attributed to multiple Andreev reflections (MARs). The peak present at V_{sd} = 0 V corresponds to the superconductive state. On the other hand, above $V_{sd} \sim \pm 0.8$ mV, the differential conductance becomes constant and is equal to the inverse of the normal resistance, R_n^{-1}. Between these two extrema, the differential conductance dI/dV displays characteristic singularities (minima and maxima), which represent the subharmonic gap structures [147-150]. Their presence is a signature of the high transparency of the interfaces between S and N regions. The positions of these MAR singularities follow the equation $eV_n = 2\Delta^*/n$, with n = 1, 2, 3 ... and Δ^* the induced gap in the N region. Most commonly, the position of the maxima in the differential conductance has been analyzed, [26, 50, 51, 55, 59, 121, 122,

127, 128, 151] but recently it was pointed out that for highly transparent junctions, the MAR resonances appear as minima in the differential conductance [152].

In order to estimate the junction transparency and the induced gap, a simple scattering model that assumes fully-coherent transport across a multimode JJ (see Ref.119 and the figure 6.6) has been used and that has been applied to reproduce MAR traces of nanowire junctions [153]. Thus, the experimental curves were compared to optimized theoretical MAR conductance traces. One example is shown in Fig. 6.6(b) at back gate voltage of 15V. The best agreement between experiment and theory is obtained for a junction model with 40 modes of transparency $T_r = 0.94$ and an induced gap of $\Delta^* = 160$ µeV [154]. The dashed vertical lines in Fig. 6.6 highlight the series from $n = \pm 1$ to $n = \pm 5$, showing an excellent agreement with the predicted behavior for the minima in differential conductance in a highly transparent junction [152]. Results of the analysis for the other back gate voltages are very similar. Consistently, while the transparency of the modes and the induced gap do not change with back gate voltage, the number of modes does: from less than 30 at $V_{bg} = 10$ V to more than 50 at $V_{bg} = 30$ V. The obtained value of the induced gap, $\Delta^* = 160$ µeV, is smaller than the value extracted from the measurement of the critical temperature. We note that similar values for the induced gap Δ^* have been reported for InSb nanowires proximitized by Nb [55] and by NbTiN [54].
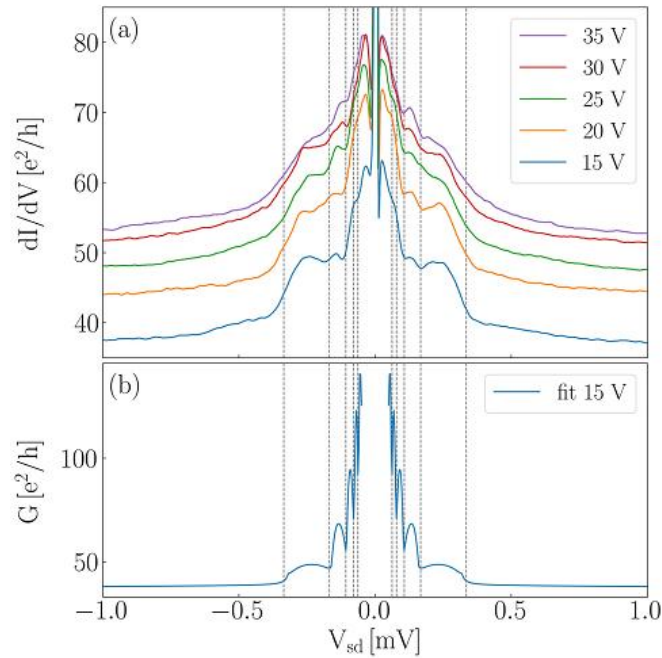
Figure 6.6: (a) Differential conductance dI/dV , measured by lock-in technique at 250 mK, as a function of source drain voltage V_{sd} for several back gate voltages V_{bg}, as indicated in the legend. The dashed lines indicate minima in differential conductance caused by MARs ($n = \pm 1$ to $n = \pm 5$). B = 6 mT applied to compensate for the residual magnetization of the cryostat. (b) Conductance line trace obtained from a coherent scattering model versus source-

drain voltage V_{sd}. The theoretical fit of the data for $V_{bg} = 15$ V yields a transmission $T_r = 0.94$ and a value of the induced gap of $\Delta^* = 160$ μeV.

Besides differential conductance data, we recorded also DC traces (I−V curves). Figure 6.7 shows representative example obtained with $V_{bg} = 40$ V. From a linear fit of the part of the curve at high bias, with $|V_{sd}| \geq 2\Delta^*$, where Andreev reflections are completely suppressed, we obtain an excess current of $I_e = 265 \pm 12$ nA and a normal resistance of $R_n = 481 \pm 3$ Ω. We add that the results do not change significantly if we consider only the voltage range $|V_{sd}| \geq 2$ meV. These numbers result in a product $I_e \cdot R_n = 127 \pm 7$ μV, an important figure of merit for weak links [155]. From $V_{bg} = 40$ V to 20 V, the excess current is almost constant, while it decreases for smaller back gate values, to ∼ 50 nA at $V_{bg} = 5$ V. The normal resistance displays the opposite behavior: below $V_{bg} = 20$ V it increases significantly to about 3.1 kΩ at $V_{bg} = 5$ V. As shown in the fig. 6.5(b), the product of excess current and normal resistance, $I_e \cdot R_n$, remains approximately constant at 137 ± 19 μV over the whole range of back gate voltages explored, i.e., from $V_{bg} = 5$ V to 40 V.

We should like to analyse the superconducting-gap values as obtained from the critical temperature of the superconductor and the observed multiple Andreev-reflection features. The measured critical temperature $T_c = 8.44$ K is close to the reported value for bulk Nb and the resulting value of the gap $\Delta = 1.28$ meV is in good agreement with values reported for JJs with Nb contacts [121-127, 151]. Thus, we attribute the observed critical temperature to a switching of the Nb film from the superconducting to the normal state.

On the other hand, several groups reported gap values extracted from an analysis of MAR features that were smaller than the BCS-like gap of the superconducting leads [50, 64, 132]. Kjaergaard et al. investigated multiple Andreev reflections in an InAs quantum-well heterostructure with epitaxial Al [152]. From an analysis of the MAR features, authors obtained a gap value smaller than the BCS-like gap Δ of Al, and showed that this is due to an induced gap $\Delta^* < \Delta$ in the quantum well covered by Al. Andreev reflections of particles in the uncovered region occur at the (vertical) effective interface to the covered region with gap Δ^* in the quantum well. Since these reflections occur within the InSb crystal, the transparency of the process is high (here $T_r = 0.94$).

Another relevant effect is the proximity-effect transfer from the Nb into InSb via the thin Ti film. Drachmann et al. studied the proximity-effect transfer from a NbTi film into an InAs quantum well via a thin epitaxial Al layer [156]. They found that the induced gap Δ^* was increased by the NbTi film compared to samples with just the Al film, but it was still smaller than the BCS-like gap of NbTi. This implies that the proximity effect transfer can be weakened by an intermediate superconducting layer with smaller T_c. We recall that the reported T_c value for bulk Ti is ∼ 0.5 K, [157, 158] i.e., much smaller than the T_c of Nb. The combination of both effects is likely able to explain the observed value of the induced gap in our experiments.
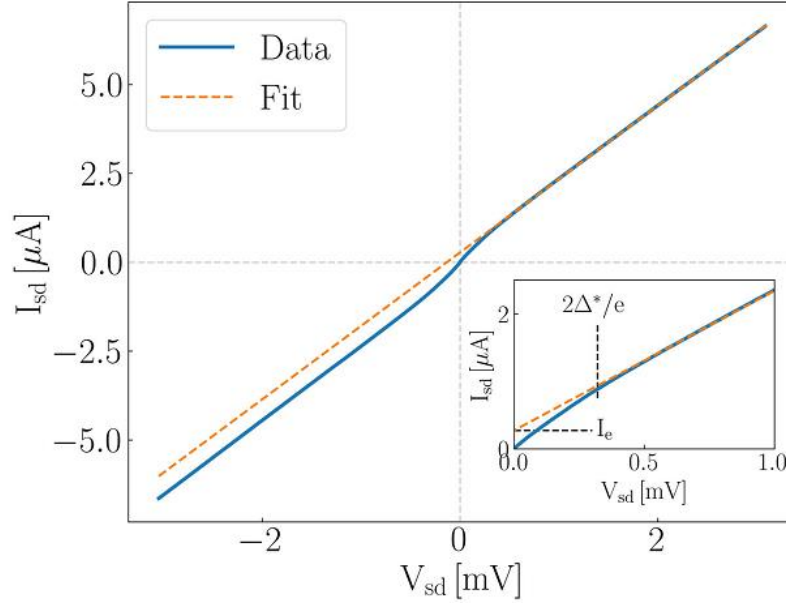
Figure 6.7: $I − V$ characteristics measured in DC. The linear fit (dashed line) of the $I − V$ curve for $V_{sd} > 2\Delta^*/e$ gives the excess current I_e as the intercept at zero bias voltage. The inset displays the excess current in a smaller bias voltage range. $T = 250$ mK and $V_{bg} = 40$ V. $B = 6$ mT applied to compensate for the residual magnetization of the cryostat.

The transparency of the (horizontal) interfaces between the superconducting electrodes and the InSb can be estimated using the theory of Aminov et al., [159] which measures the transparency via the dimensionless parameter γ_B ($\gamma_B = 0$ for perfectly transparent interfaces, larger γ_B for larger barriers). Using the BCS gap of Nb, we obtain $\gamma_B = 12.5$. Considering that the presence of the Ti film will slightly reduce the gap by an (unknown) amount, $\gamma_B \approx 10$. This indicates a small transparency of the interface, consistent with the fact that the induced gap is much smaller than the BCS gap of Nb. On the other hand, Kjaergaard et al. [152] and Baumgartner et al. [160] report $\gamma_B \sim 1$, consistent with their use of epitaxial Al/InAs heterostructures, which are known to have highly transparent interfaces. Theory predicts for JJ at $T = 0$ that the product $I_c \cdot R_n$ is constant proportional to the gap, $I_c \cdot R_n = \alpha\Delta^*/e$, with the prefactor α a constant of order unity [132, 161-165]. Here $I_c \cdot R_n = 15$ µV is only about 10% of $\Delta^*/e = 160$ µV. Such a reduction is frequently observed in experiment [59, 128, 166] and has been attributed to a premature switching of the junction due to thermal activation [161, 167]. On the other hand, excess current is due to Andreev reflections and thus depends primarily on the transparency of the (vertical) interface between the covered and uncovered parts of the semiconductor, [165] which is high. Consequently, a large product $I_e \cdot R_n \approx \Delta^*/e$ is observed, close to the theoretical value of 8/3 Δ^*/e for ballistic junctions [150, 165].

6.4 Conclusions

In summary, we have fabricated JJ devices with InSb NFs as normal region and Ti/Nb as superconducting contacts. The high electron mobility and large mean free path of the InSb NFs

yielded ballistic transport across the normal region of the junction. We showed Josephson coupling between superconductor and semiconductor, as demonstrated by the zero-resistance supercurrent of ~ 50 nA and the observation of MARs. Analysis of the MAR traces indicates a very high transparency of the interfaces. We also observe a sizable excess current. Our results show that free-standing 2D InSb NF on InP stems, thanks to their defect-free ZB crystal structure, are a suitable material platform for fabrication of quantum devices. Considering also their strong spin-orbit interaction and their large Land´e g-factor, we envision the use of these structures in future studies towards topological superconductivity.

Chapter 7: Summary and Outlook

7.1 Summary

A crucial milestone of this activity was the growth of high-quality InSb nanostructures via Au-assisted CBE, in particular NFs that demonstrate superior electronic properties. Their superconductive devices providing evidence of induced zero-resistance supercurrent, indicating phase-coherent transport in the junction and high transparency of the interfaces

In this work, we optimized the growth protocols for the realization of free-standing InSb nanostructures with different morphologies, like NWs, NFs, and NCs, with high crystal quality and nearly 100% yield on InAs NW stems by precisely tuning the growth parameters. The transition from InSb NWs to NCs is achieved by decreasing the InSb growth temperature by 20°C while keeping the other growth parameters (time and fluxes) fixed. By stopping the substrate rotation, asymmetry in shape was triggered and the direction of asymmetric growth is towards the impingent-beam fluxes. Moreover, an additional growth step with increased TMSb line pressure (with respect to that used for NWs) boosts the radial (width) growth rate and results in a NF morphology. The InSb NFs obtained have an average length, width, and thickness of (1.3 ± 0.1) μm, (282 ± 87) nm and (104 ± 17) nm, respectively The existence of two families of NFs, characterized by aperture angles of 145° and 160° at the base, is observed and modeled. The InSb NFs are pure ZB single crystals without any defect, such as stacking faults or twin planes, regardless of the different final shape (aperture angle and number of sides). Our results provide useful guidelines for the selective growth of high-quality InSb nanostructures of different morphology.

Since a larger 2D InSb NF morphology would provide flexibility in fabrication and more accurate electronic measurements, we modified our heterostructured system and growth parameters. This was possible by carefully choosing a robust supportive stem, tapered InP NWs, by optimizing the growth parameters leading to the growth of InSb NWs with high yield and high aspect ratio, and by aligning the samples with the aid of RHEED in the direction that maximizes the NF elongation keeping the NF thickness at a minimum. This strategy allowed us to obtain InSb NFs of (2.8 ± 0.2) μm length, (470 ± 80) nm width, and (105 ± 20) nm thickness with defect-free ZB crystal structure, stoichiometric composition, and relaxed lattice parameters. In addition, we speculate that similar morphologies might be achieved by adopting this directional growth approach for other materials if they show a consistent radial growth together with the axial elongation. We were further able to obtain larger InSb NFs that are (2.9 ± 0.3) μm long, (850 ± 190) nm wide, and (200 ± 25) nm thick by exploiting our knowledge derived from the growth optimization of InSb NWs on InP stems and 2D InSb NFs grown in regular arrays using InP NW templates synthesized on patterned SiO_2/InP(111)B substrates.

Furthermore, we presented a growth model which allows for the semi-quantitative description of the NF morphology as a function of the growth time and pitch. The NF length evolution can be qualitatively explained by considering the In-limited VLS axial growth rate containing two contributions: (1) the direct impingement and (2) In adatom diffusion on the NF sidewalls. In particular, the with-over-thickness ratio has been identified by the pitch-dependent shadowing effect for the re-emitted Sb flux. Overall, these findings can be used for tuning the InSb NF morphology and probably extended to other material systems.

To investigate the electronic properties of the InSb NFs, we were able to realize Hall-bar devices far enough to keep the reasonable length-to-width ratio between longitudinal and transversal contacts, which avoided the presence of mixed components in Hall-bar measurements and allowed us to accurately investigate the electrical properties. The presence of good Ohmic contacts between the InSb NFs and the metal contacts and the absence of a Schottky barrier were confirmed from the linear I-V plots. The charge carrier modulation shows an increasing conductance with increasingly positive back gate voltage, consistent with an n-type behavior of the InSb NFs. We performed low-temperature (at 4.2 K) four-probe measurements and low-field Hall effect on these Hall-bar devices. We measured the electron mobility of about 29500 cm^2/(V s) at $V_{BG} = 25$ V, with a corresponding electron density of 8.5 $\times 10^{11}$ cm^{-2}, which is highest compared to other similar 2D InSb nanostructures reported in the literature. The electron mean free path reaches values of ~500 nm for $V_{BG} \geq 25$ V.

We also fabricated Josephson junction devices based on these InSb NFs by employing Ti/Nb contacts. The high electron mobility and large mean free path of the InSb NFs yielded ballistic transport across the normal region of the junction. The devices show gate-tunable proximity-induced supercurrent of 50 nA at 250 mK and a sizable excess current. The devices also show clear signatures of subharmonic gap structures, indicating phase-coherent transport in the junction and highly transparent interfaces. Our results indicate InSb NFs as a promising platform for the study of topological superconductivity.

7.2 Future outlook

As a "grower", I have always appreciated the power of feedback from our collaborators. It is a continuous loop in which we both improve. So first future outlook in this scope would be to perform more experiments and modeling to access the NF morphology for longer growth times and develop a more detailed understanding of the entire growth process, particularly in the regimes corresponding to the highest aspect ratios (W/T) of the NFs.

This work on the free-standing 2D InSb NFs and electrical transport properties of NF and NF-based devices lends itself to further, interesting investigation directions. The JoFET in this study has a channel width of 200 nm which can be safely increased up to 500 nm as the mean free path lengths would ensure ballistic transport. It would be important to see if the phase-coherent transport will be extended for these channel widths.

Another bottleneck in the current JoFET device is the intermediate Ti film. The proximity effect transfer can be weakened by an intermediate superconducting layer with smaller Tc. So in future, we would like to fabricate and measure devices without Ti film between InSb NF and Nb contact. But it would be challenging as Nb doesn't adhere well to the InSb and calls for special treatment of the interface to make it adhesive without degrading the carrier transmission probability.

And eventually, our final aim would be to see if these NFs can serve for the realization of exotic bound states at the semiconductor interface with superconductors, paving the way for the development of topological quantum computation technologies.

Appendix

Appendix A: List of recurring abbreviations

1D- one-dimensional

2D- two-dimensional

3D- three-dimesional

ADF- annular dark field

Ag- Silver

Ar- Argon

AsB- angle selective backscatter

Au- Gold

BCS- Bardeen, Cooper, and Schrieffer

BF- bright field

BG- back gate

BR- Bragg reflections

CAD- computer-aided design

CBE- chemical beam epitaxy

CEO- cleave edge overgrowth

CMOS- complementary metal oxide semiconductor

CVD- chemical vapor deposition

D- drain

DF- dark field

DIL- dual in-line

DI water- deionized water

DtBSe- ditertiarybutyl selenide

EBL- electron-beam lithography

EDX- energy dispersive X-ray

EsB- energy selective backscatter

FFT- fast Fourier transform

GPA- geometrical phase analysis

HAADF- high angle annular dark field

HF- hydrofluoride

HRTEM- high-resolution transmission electron microscopy

HT- high temperature

IC- integrated circuit

InAs- indium arsenide

InP- indium phosphide

InSb- indium antimonide

IR- infrared

JJ- Josephson junction

JoFET- Josephson field effect transistor

L- length

LT- low temperature

MAR- multiple Andreev reflection

MBE- molecular beam epitaxy

MO- metal-organics

MOVPE- metal-organic vapor phase epitaxy

MZM- Majorana zero modes

Nb- niobium

NC- nanocube

NEMS- nanoelectromechanical switches

NF- nanoflag

nm- nanometer

NP- nanoparticle

NW- nanowire

OVC- outer vacuum chamber

PMMA- poly-methyl-meth-acrylate

RF- radio frequency

RHEED- reflection high-energy electron diffraction

rpm- rotations per minute

S- source

SAE- selective area epitaxy

sccm- standard cubic centimeter per minute

SQUID- superconducting quantum interference device

SEM- scanning electron microscopy

STEM- scanning transmission electron microscopy

T- thickness

TBAs- tertiarybutylarsine

TBP- tertiarybutylphosphine

TDMASb- tris(dimethylamino)antimony

TEGa- triethylgallium

TEM- transmission electron microscopy

Ti- titanium

TMAl- trimethylaluminum

TMIn- trimethylindium

TMSb- trimethylantimony

TPB- three phase boundary

UHV- ultra-high vacuum

VLS- vapour-liquid-solid

VS- vapor-solid

VSM- vibrating sample magnetometer

VSS- vapor-solid-solid

W- width

WZ- wurtzite

ZB- zinc blend

Bibliography

[1]   G. E. Moore, "Cramming More Components onto Integrated Circuits," *Electronics*, vol. 38, no. 8, pp. 114–117, 1965.

[2]   H. Radamson and L. Thylén, *Monolithic Nanoscale Photonics-Electronics Integration in Silicon and Other Group IV Elements*, 2014.

[3]   S.W. King, H. Simka, D. Herr, H. Akinaga, and M. Garner, "Research updates: the three M's (materials, metrology, and modeling) together pave the path to future nanoelectronic technologies," *APL Materials*, 1, , 2013, doi: 10.1063/1.4822437.

[4]   P. Benioff, "The computer as a physical system: A microscopic quantum mechanical Hamiltonian model of computers as represented by Turing machines," *J. Stat. Phys.*, vol. 22, no. 5, pp. 563–591, 1980, doi: 10.1007/BF01011339.

[5]   R. P. Feynman, "Simulating physics with computers," *Int. J. Theor. Phys.*, vol. 21, no. 6–7, pp. 467–488, 1982, doi: 10.1007/BF02650179.

[6]   Microsoft. Microsoft Quantum: Research, https://azure.microsoft.com/en-us/solutions/quantum-computing/#news-blogs.

[7]   Google. Quantum - Google AI, https://quantumai.google.

[8]   IBM. IBM Q, https://www.ibm.com/quantum-computing/.

[9]   Intel. Quantum Computing, https://www.intel.com/content/www/us/en/newsroom/resources/press-kits-quantum-computing.html#gs.muppa8

[10]   DWave. DWave The Quantum Computing Company, https://www.dwavesys.com.

[11]   IONQ. A true quantum leap, https://ionq.com/?/home

[12]   Baidu Research. http://research.baidu.com/Index

[13]   Tencent. https://www.tencent.com/en-us/

[13]   J. Preskill, "Quantum computing and the entanglement frontier," pp. 1–18, 2012, [Online]. Available: http://arxiv.org/abs/1203.5813

[14]   L. K. Grover, "A fast quantum mechanical algorithm for database search", Proceedings of the twenty-eighth annual ACM symposium on Theory of Computing, pp 212–219, 1996, doi: 10.1145/237814.237866.

[15]   T. D. Ladd, F. Jelezko, R. Laflamme, Y. Nakamura, C. Monroe, and J. L. O'Brien, "Quantum computers," *Nature*, vol. 464, no. 7285, pp. 45–53, 2010, doi: 10.1038/nature08812.

[16]   R. J. Hughes, "Quantum computation," *Feynman Comput.*, pp. 191–221, 2018, doi: 10.1201/9780429500459.

[17]   A. Stern, "Non-Abelian states of matter," *Nature*, vol. 464, no. 7286, pp. 187–193, 2010, doi: 10.1038/nature08915.

[18]   A. Stern and N. H. Lindner, "Topological quantum computation - From basic concepts to first experiments," *Science (80-.).*, vol. 339, no. 6124, pp. 1179–1184, 2013, doi: 10.1126/science.1231473.

[19]   D. Leibfried, R. Blatt, C. Monroe, and D. Wineland, "Quantum dynamics of single trapped ions," *Rev. Mod. Phys.*, vol. 75, no. 1, pp. 281–324, 2003, doi: 10.1103/RevModPhys.75.281.

[20]   M. H. Devoret and R. J. Schoelkopf, "Superconducting circuits for quantum information: An outlook," *Science (80-.).*, vol. 339, no. 6124, pp. 1169–1174, 2013, doi: 10.1126/science.1231930.

[21]   R. Hanson and D. D. Awschalom, "Coherent manipulation of single spins in semiconductors," *Nature*, vol. 453, no. 7198, pp. 1043–1049, 2008, doi: 10.1038/nature07129.

[22]   F. D. M. Haldane, "Nobel lecture: Topological quantum matter," *Rev. Mod. Phys.*, vol. 89, no. 4, pp. 1–10, 2017, doi: 10.1103/RevModPhys.89.040502.

[23]   C. Nayak, S. H. Simon, A. Stern, M. Freedman, and S. Das Sarma, "Non-Abelian anyons and topological quantum computation," *Rev. Mod. Phys.*, vol. 80, no. 3, pp. 1083–1159, 2008, doi: 10.1103/RevModPhys.80.1083.

[24]   E. Prada *et al.*, "From Andreev to Majorana bound states in hybrid superconductor–semiconductor nanowires," *Nat. Rev. Phys.*, vol. 2, no. 10, pp. 575–594, 2020, doi: 10.1038/s42254-020-0228-y.

[25]   A. Fornieri *et al.*, "Evidence of topological superconductivity in planar Josephson junctions," *Nature*, vol. 569, no. 7754, pp. 89–92, 2019, doi: 10.1038/s41586-019-1068-8.

[26]   C. M. Moehle *et al.*, "InSbAs Two-Dimensional Electron Gases as a Platform for Topological Superconductivity," *Nano Lett.*, vol. 21, no. 23, pp. 9990–9996, 2021, doi: 10.1021/acs.nanolett.1c03520.

[27]   M. S. Gudiksen, L. J. Lauhon, J. Wang, D. C. Smith, and C. M. Lieber, "Growth of nanowire superlattice structures for nanoscale photonics and electronics," *Nature*, vol. 415, no. February, p. 617, 2002.

[28]   X. Zhou, S. A. Dayeh, D. Aplin, D. Wang, and E. T. Yu, "Direct observation of ballistic and drift carrier transport regimes in InAs nanowires," *Appl. Phys. Lett.*, vol. 89, no. 5, 2006, doi: 10.1063/1.2236589.

[29]   M. T. Björk *et al.*, "Nanowire resonant tunneling diodes," *Appl. Phys. Lett.*, vol. 81, no. 23, pp. 4458–4460, 2002, doi: 10.1063/1.1527995.

[30]   H. J. Joyce *et al.*, "<IEEESelTopQuantElectron_2010_Joyce_TailoringGaAsInAsInGaAs.pdf>," vol. 17, no. 4, pp. 766–778, 2011.

[31] H. J. Joyce, J. Wong-Leung, Q. Gao, H. Hoe Tan, and C. Jagadish, "Phase perfection in zinc blende and wurtzite III- V nanowires using basic growth parameters," *Nano Lett.*, vol. 10, no. 3, pp. 908–915, 2010, doi: 10.1021/nl903688v.

[32] H. J. Joyce *et al.*, "Unexpected benefits of rapid growth rate for III-V nanowires," *Nano Lett.*, vol. 9, no. 2, pp. 695–701, 2009, doi: 10.1021/nl803182c.

[33] K. A. Dick *et al.*, "Control of III-V nanowire crystal structure by growth parameter tuning," *Semicond. Sci. Technol.*, vol. 25, no. 2, 2010, doi: 10.1088/0268-1242/25/2/024009.

[34] A. Li, J. Zou, and X. Han, "Growth of III-V semiconductor nanowires and their heterostructures," *Sci. China Mater.*, vol. 59, no. 1, pp. 51–91, 2016, doi: 10.1007/s40843-016-0119-9.

[35] Z. Zhang *et al.*, "In Situ TEM Observation of Crystal Structure Transformation in InAs Nanowires on Atomic Scale," *Nano Lett.*, vol. 18, no. 10, pp. 6597–6603, 2018, doi: 10.1021/acs.nanolett.8b03231.

[36] B. A. Wacaser, K. A. Dick, J. Johansson, M. T. Borgström, K. Deppert, and L. Samuelson, "Preferential interface nucleation: An expansion of the VLS growth mechanism for nanowires," *Adv. Mater.*, vol. 21, no. 2, pp. 153–165, 2009, doi: 10.1002/adma.200800440.

[37] C. T. Foxon and B. Joyce, "Interaction kinetics of As4 and Ga on {100} surfaces," *Surf. Sci.*, vol. 50, p. 434, 1977.

[38] Y. Yamamoto and K. G. Stephens, "A metallurgical investigation of the AuSb and AuAs systems," *Thin Solid Films*, vol. 60, no. 1, pp. 123–131, 1979, doi: 10.1016/0040-6090(79)90356-0.

[39] I. V. Markov, "Nucleation 2.1.," *Cryst. Growth Beginners*, vol. 1, no. 1927, pp. 77–179, 2003.

[40] L. E. Fröberg *et al.*, "Transients in the formation of nanowire heterostructures," *Nano Lett.*, vol. 8, no. 11, pp. 3815–3818, 2008, doi: 10.1021/nl802149v.

[41] H. Heinecke, "III—v crystal growth of novel layered structures using metalorganic molecular beam epitaxy," *Phys. Scr.*, vol. 1993, no. T49B, pp. 742–747, 1993, doi: 10.1088/0031-8949/1993/T49B/062.

[42] R. M. Lutchyn, J. D. Sau, and S. Das Sarma, "Majorana fermions and a topological phase transition in semiconductor-superconductor heterostructures," *Phys. Rev. Lett.*, vol. 105, no. 7, pp. 1–4, 2010, doi: 10.1103/PhysRevLett.105.077001.

[43] Y. Oreg, G. Refael, and F. Von Oppen, "Helical liquids and Majorana bound states in quantum wires," *Phys. Rev. Lett.*, vol. 105, no. 17, pp. 1–4, 2010, doi: 10.1103/PhysRevLett.105.177002.

[44] R. M. Lutchyn, E. P. A. M. Bakkers, L. P. Kouwenhoven, P. Krogstrup, C. M. Marcus, and Y. Oreg, "Majorana zero modes in superconductor-semiconductor heterostructures," *Nat. Rev. Mater.*, vol. 3, no. 5, pp. 52–68, 2018, doi:

10.1038/s41578-018-0003-1.

[45] Y. Chen, S. Huang, J. Mu, D. Pan, J. Zhao, and H. Q. Xu, "A double quantum dot defined by top gates in a single crystalline InSb nanosheet," *Chinese Phys. B*, vol. 30, no. 12, 2021, doi: 10.1088/1674-1056/abff2e.

[46] F. Qu *et al.*, "Quantized Conductance and Large g-Factor Anisotropy in InSb Quantum Point Contacts," *Nano Lett.*, vol. 16, no. 12, pp. 7509–7513, 2016, doi: 10.1021/acs.nanolett.6b03297.

[47] M. De La Mata *et al.*, "Twin-Induced InSb Nanosails: A Convenient High Mobility Quantum System," *Nano Lett.*, vol. 16, no. 2, pp. 825–833, 2016, doi: 10.1021/acs.nanolett.5b05125.

[48] T. Ashley, A. B. Dean, and C. T. Elliott, "Uncooled high-speed InSb field-effect transistors," vol. 481, no. November 1994, 2019.

[49] R. J. Sladek, "Effective Masses of Electrons in Indium Arsenide and Indium Antimonide," *Phys. Rev.*, vol. 105, pp. 460–464, 1957.

[50] C. T. Ke *et al.*, "Ballistic superconductivity and tunable π–junctions in InSb quantum wells," *Nat. Commun.*, vol. 10, no. 1, pp. 1–6, 2019, doi: 10.1038/s41467-019-11742-4.

[51] F. K. De Vries *et al.*, "Crossed Andreev reflection in InSb flake Josephson junctions," *Phys. Rev. Res.*, vol. 1, no. 3, pp. 1–5, 2019, doi: 10.1103/PhysRevResearch.1.032031.

[52] Z. Lei *et al.*, "Gate-defined quantum point contact in an InSb two-dimensional electron gas," *Phys. Rev. Res.*, vol. 3, no. 2, 2021, doi: 10.1103/PhysRevResearch.3.023042.

[53] I. Zutic, J. Fabian, S. D. Sharma, "Spintronics: Fundamentals and applications," *Rev. Mod. Phys*, vol. 76, no. 2, 2004.

[54] V. Mourik, K. Zuo, S. M. Frolov, S. R. Plissard, E. P. A. M. Bakkers, and L. P. Kouwenhoven, "Signatures of majorana fermions in hybrid superconductor-semiconductor nanowire devices," *Science (80-.)*, vol. 336, no. 6084, pp. 1003–1007, 2012, doi: 10.1126/science.1222360.

[55] M. T. Deng, C. L. Yu, G. Y. Huang, M. Larsson, P. Caroff, and H. Q. Xu, "Anomalous zero-bias conductance peak in a Nb-InSb nanowire-Nb hybrid device," *Nano Lett.*, vol. 12, no. 12, pp. 6414–6419, 2012, doi: 10.1021/nl303758w.

[56] H. Zhang *et al.*, "Ballistic superconductivity in semiconductor nanowires," *Nat. Commun.*, vol. 8, no. May, 2017, doi: 10.1038/ncomms16025.

[57] Ö. Gül *et al.*, "Hard Superconducting Gap in InSb Nanowires," *Nano Lett.*, vol. 17, no. 4, pp. 2690–2696, 2017, doi: 10.1021/acs.nanolett.7b00540.

[58] H. A. Nilsson, P. Samuelsson, P. Caroff, and H. Q. Xu, "Supercurrent and multiple Andreev reflections in an InSb nanowire Josephson junction," *Nano Lett.*, vol. 12, no. 1, pp. 228–233, 2012, doi: 10.1021/nl203380w.

[59] S. Li *et al.*, "Coherent Charge Transport in Ballistic InSb Nanowire Josephson Junctions," *Sci. Rep.*, vol. 6, no. April, pp. 1–8, 2016, doi: 10.1038/srep24822.

[60] S. Gazibegovic *et al.*, "Epitaxy of advanced nanowire quantum devices," *Nature*, vol. 548, no. 7668, pp. 434–438, 2017, doi: 10.1038/nature23468.

[61] Ö. Gül *et al.*, "Ballistic Majorana nanowire devices," *Nat. Nanotechnol.*, vol. 13, no. 3, pp. 192–197, 2018, doi: 10.1038/s41565-017-0032-8.

[62] S. T. Gill *et al.*, "Selective-Area Superconductor Epitaxy to Ballistic Semiconductor Nanowires," *Nano Lett.*, vol. 18, no. 10, pp. 6121–6128, 2018, doi: 10.1021/acs.nanolett.8b01534.

[63] J. E. Sestoft *et al.*, "Engineering hybrid epitaxial InAsSb/Al nanowires for stronger topological protection," *Phys. Rev. Mater.*, vol. 2, no. 4, pp. 1–8, 2018, doi: 10.1103/PhysRevMaterials.2.044202.

[64] M. Pendharkar *et al.*, "Parity-preserving and magnetic field–resilient superconductivity in InSb nanowires with Sn shells," *Science (80-.).*, vol. 372, no. 6541, pp. 508–511, 2021, doi: 10.1126/science.aba5211.

[65] C. Downs and T. E. Vandervelde, *Progress in infrared photodetectors since 2000*, vol. 13, no. 4. 2013.

[66] M. De La Mata, C. Magén, P. Caroff, and J. Arbiol, "Atomic scale strain relaxation in axial semiconductor III-V nanowire heterostructures," *Nano Lett.*, vol. 14, no. 11, pp. 6614–6620, 2014, doi: 10.1021/nl503273j.

[67] D. Ercolani *et al.*, "InAs/InSb nanowire heterostructures grown by chemical beam epitaxy," *Nanotechnology*, vol. 20, no. 50, 2009, doi: 10.1088/0957-4484/20/50/505605.

[68] M. B. Borg and L. E. Wernersson, "Synthesis and properties of antimonide nanowires," *Nanotechnology*, vol. 24, no. 20, 2013, doi: 10.1088/0957-4484/24/20/202001.

[69] S. Yip, L. Shen, and J. C. Ho, "Recent advances in III-Sb nanowires: From synthesis to applications," *Nanotechnology*, vol. 30, no. 20, 2019, doi: 10.1088/1361-6528/aafcce.

[70] P. Krogstrup *et al.*, "Epitaxy of semiconductor-superconductor nanowires," *Nat. Mater.*, vol. 14, no. 4, pp. 400–406, 2015, doi: 10.1038/nmat4176.

[71] Ralph E. Williams. Modern GaAs Processing Methods. Artech House microwave library, 1990.

[72] W. T. Tsang, "Chemical beam epitaxy of InP and GaAs," *Appl. Phys. Lett.*, vol. 45, no. 11, pp. 1234–1236, 1984, doi: 10.1063/1.95075.

[73] W. T. Tsang, "Ga$_{0.47}$In$_{0.53}$As/InP multiquantum well heterostructure lasers grown by molecular beam epitaxy operating at 1.53 μm," *Appl. Phys. Lett.*, vol. 44, pp. 288–290, 1984.

[74] W. T. Tsang, "From chemical vapor epitaxy to chemical beam epitaxy," *J. Cryst. Growth*, vol. 95, pp. 121, 1989, doi: https://doi.org/10.1016/0022-0248(89)90364-3.

[75] H. Lüth, "Chemical beam epitaxy - a child of surface science," *Surf. Sci.*, vol. 299–300, no. C, pp. 867–877, 1994, doi: 10.1016/0039-6028(94)90703-X.

[76] S. Ino, "Experimental overview of surface structure determination by RHEED. In Reflection High-Energy Electron Diffraction and Reflection Electron Imaging of Surfaces", *Nato a S I Series Series B, Physics*, pp. 3–28. Plenum Press, 1988.

[77] A. Ichimiya, and P. I. Cohen, "Reflection high-energy electron diffraction", *Cambridge University Press*.Cambridge, UK, 2004.

[78] L. M. Peng, S. L.Dudarev, and M. J. Whelan, "High energy electron diffraction and microscopy (monographs on the physics and chemistry of materials)", *Oxford Science Pr.*, Oxford, UK, 2011.

[79] J. Jo, Y. Tchoe, G. C. Yi, and M. Kim, "Real-Time Characterization Using in situ RHEED Transmission Mode and TEM for Investigation of the Growth Behaviour of Nanomaterials," *Sci. Rep.*, vol. 8, no. 1, pp. 1–10, 2018, doi: 10.1038/s41598-018-19857-2.

[80] R. F. Egerton, "Physical Principles of Electron Microscopy: An Introduction to TEM, SEM, and AFM", In: *chemistry and Materials Science, Springer,* Boston, MA, 2005

[81] R. Wirth, "Focused Ion Beam (FIB) combined with SEM and TEM: Advanced analytical tools for studies of chemical composition, microstructure and crystal structure in geomaterials on a nanometre scale," *Chem. Geol.*, vol. 261, no. 3–4, pp. 217–229, 2009, doi: 10.1016/j.chemgeo.2008.05.019.

[82] M. J. Hÿtch, E. Snoeck, and R. Kilaas, "Quantitative measurement of displacement and strain fields from HREM micrographs," *Ultramicroscopy*, vol. 74, no. 3, pp. 131–146, 1998, doi: 10.1016/S0304-3991(98)00035-7.

[83] V. Grillo and F. Rossi, "STEM_CELL: A software tool for electron microscopy. Part 2 analysis of crystalline materials," *Ultramicroscopy*, vol. 125, pp. 112–129, 2013, doi: 10.1016/j.ultramic.2012.10.009.

[84] D. Pan *et al.*, "Free-Standing Two-Dimensional Single-Crystalline InSb Nanosheets," *Nano Lett.*, vol. 16, no. 2, pp. 834–841, 2016, doi: 10.1021/acs.nanolett.5b04845.

[85] S. Gazibegovic *et al.*, "Bottom-Up Grown 2D InSb Nanostructures," *Adv. Mater.*, vol. 31, no. 14, 2019, doi: 10.1002/adma.201808181.

[86] S. R. Plissard *et al.*, "From InSb nanowires to nanocubes: Looking for the sweet spot," *Nano Lett.*, vol. 12, no. 4, pp. 1794–1798, 2012, doi: 10.1021/nl203846g.

[87] D. Car, J. Wang, M. A. Verheijen, E. P. A. M. Bakkers, and S. R. Plissard, "Rationally designed single-crystalline nanowire networks," *Adv. Mater.*, vol. 26, no. 28, pp. 4875–4879, 2014, doi: 10.1002/adma.201400924.

[88] I. Verma, V. Zannier, F. Rossi, D. Ercolani, F. Beltram, and L. Sorba, "Morphology control of single-crystal InSb nanostructures by tuning the growth parameters," *Nanotechnology*, vol. 31, no. 38, 2020, doi: 10.1088/1361-6528/ab9aee.

[89] L. Lugani, D. Ercolani, F. Rossi, G. Salviati, F. Beltram, and L. Sorba, "Faceting of InAs-InSb heterostructured nanowires," *Cryst. Growth Des.*, vol. 10, no. 9, pp. 4038–4042, 2010, doi: 10.1021/cg1006814.

[90]   U. P. Gomes, D. Ercolani, V. Zannier, F. Beltram, and L. Sorba, "Controlling the diameter distribution and density of InAs nanowires grown by Au-assisted methods," *Semicond. Sci. Technol.*, vol. 30, no. 11, 2015, doi: 10.1088/0268-1242/30/11/115012.

[91]   L. Lugani, D. Ercolani, L. Sorba, N. V. Sibirev, M. A. Timofeeva, and V. G. Dubrovskii, "Modeling of InAsInSb nanowires grown by Au-assisted chemical beam epitaxy," *Nanotechnology*, vol. 23, no. 9, 2012, doi: 10.1088/0957-4484/23/9/095602.

[92]   A. Y. Cho and K. Y. Cheng, "Growth of extremely uniform layers by rotating substrate holder with molecular beam epitaxy for applications to electro-optic and microwave devices," *Appl. Phys. Lett.*, vol. 38, no. 5, pp. 360–362, 1981, doi: 10.1063/1.92377.

[93]   C. T. Foxon, "MBE GROWTH OF GaAs AND III-V ALLOYS.," *J. Vac. Sci. Technol. B Microelectron. Nanom. Struct.*, vol. 1, no. 2, pp. 293–297, 1982, doi: 10.1116/1.582505.

[94]   P. Frigeri, L. Seravalli, G. Trevisi, and S. Franchi, "Molecular Beam Epitaxy: An Overview," *Compr. Semicond. Sci. Technol.*, vol. 1–6, no. 1, pp. 480–522, 2011, doi: 10.1016/B978-0-44-453153-7.00099-7.

[95]   B. R. Bennett, R. Magno, and B. V. Shanabrook, "Molecular beam epitaxial growth of InSb, GaSb, and AlSb nanometer-scale dots on GaAs," *Appl. Phys. Lett.*, vol. 505, no. 1996, p. 505, 1995, doi: 10.1063/1.116381.

[96]   N. Moll, A. Kley, E. Pehlke, "GaAs equilibrium crystal shape from first principles," *Phys. Rev. B*, vol. 54, no. 12, 1996.

[97]   S. Gorji Ghalamestani *et al.*, "Demonstration of defect-free and composition tunable Ga xIn 1-xSb nanowires," *Nano Lett.*, vol. 12, no. 9, pp. 4914–4919, 2012, doi: 10.1021/nl302497r.

[98]   L. Namazi, M. Nilsson, S. Lehmann, C. Thelander, and K. A. Dick, "Selective GaSb radial growth on crystal phase engineered InAs nanowires," *Nanoscale*, vol. 7, no. 23, pp. 10472–10481, 2015, doi: 10.1039/c5nr01165e.

[99]   S. Battiato *et al.*, "Polychromatic emission in a wide energy range from InP-InAs-InP multi-shell nanowires," *Nanotechnology*, vol. 30, no. 19, 2019, doi: 10.1088/1361-6528/aafde4.

[100] I. Verma, S. Salimian, V. Zannier, S. Heun, F. Rossi, D. Ercolani, F. Beltram, and L. Sorba, "High-Mobility Free-Standing InSb Nanoflags Grown on InP Nanowire Stems for Quantum Devices," *ACS Appl. Nano Mater.*, vol. 4, no. 6, pp. 5825–5833, 2021, doi: 10.1021/acsanm.1c00734.

[101] U. Krishnamachari *et al.*, "Defect-free InP nanowires grown in [001] direction on InP (001)," *Appl. Phys. Lett.*, vol. 85, no. 11, pp. 2077–2079, 2004, doi: 10.1063/1.1784548.

[102] T. Ando, A. B. Fowler, and F. Stern, "Electronic properties of two-dimensional systems," *Rev. Mod. Phys.*, vol. 54, no. 2, pp. 437–672, 1982, doi: 10.1103/RevModPhys.54.437.

[103] N. Kang *et al.*, "Two-Dimensional Quantum Transport in Free-Standing InSb Nanosheets," *Nano Lett.*, vol. 19, no. 1, pp. 561–569, 2019, doi: 10.1021/acs.nanolett.8b04556.

[104] Y. Chen *et al.*, "Strong and tunable spin–orbit interaction in a single crystalline InSb nanosheet," *npj 2D Mater. Appl.*, vol. 5, no. 1, pp. 1–8, 2021, doi: 10.1038/s41699-020-00184-y.

[105] S. Salimian, M. Carrega, I. Verma, V. Zannier, M. P. Nowk, F. Beltram, L. Sorba and S. Heun, "Gate-controlled supercurrent in ballistic InSb nanoflag Josephson junctions," *Appl. Phys. Lett.*, vol. 119, no. 21, 2021, doi: 10.1063/5.0071218.

[106] J. Jiang *et al.*, "Recent Advances in 2D Materials for Photodetectors," *Adv. Electron. Mater.*, vol. 7, no. 7, pp. 1–27, 2021, doi: 10.1002/aelm.202001125.

[107] V. G. Dubrovskii and N. V. Sibirev, "Growth rate of a crystal facet of arbitrary size and growth kinetics of vertical nanowires," *Phys. Rev. E - Stat. Physics, Plasmas, Fluids, Relat. Interdiscip. Top.*, vol. 70, no. 3, p. 7, 2004, doi: 10.1103/PhysRevE.70.031604.

[108] V. G. Dubrovskii, N. V. Sibirev, R. A. Suris, G. E. Cirlin, J. C. Harmand, and V. M. Ustinov, "Diffusion-controlled growth of semiconductor nanowires: Vapor pressure versus high vacuum deposition," *Surf. Sci.*, vol. 601, no. 18, pp. 4395–4401, 2007, doi: 10.1016/j.susc.2007.04.122.

[109] L. E. Fröberg, W. Seifert, and J. Johansson, "Diameter-dependent growth rate of InAs nanowires," *Phys. Rev. B*, vol. 76, no. 15, pp. 1–4, 2007, doi: 10.1103/physrevb.76.153401.

[110] V. G. Dubrovskii *et al.*, "Gibbs-Thomson and diffusion-induced contributions to the growth rate of Si, InP, and GaAs nanowires," *Phys. Rev. B - Condens. Matter Mater. Phys.*, vol. 79, no. 20, pp. 1–7, 2009, doi: 10.1103/PhysRevB.79.205316.

[111] F. Glas, J. C. Harmand, and G. Patriarche, "Why does wurtzite form in nanowires of III-V zinc blende semiconductors?," *Phys. Rev. Lett.*, vol. 99, no. 14, pp. 3–6, 2007, doi: 10.1103/PhysRevLett.99.146101.

[112] N. V. Sibirev, M. Tchernycheva, M. A. Timofeeva, J. C. Harmand, G. E. Cirlin, and V. G. Dubrovskii, "Influence of shadow effect on the growth and shape of InAs nanowires," *J. Appl. Phys.*, vol. 111, no. 10, 2012, doi: 10.1063/1.4718434.

[113] V. G. Dubrovskii, N. V. Sibirev, J. C. Harmand, and F. Glas, "Growth kinetics and crystal structure of semiconductor nanowires," *Phys. Rev. B - Condens. Matter Mater. Phys.*, vol. 78, no. 23, pp. 1–10, 2008, doi: 10.1103/PhysRevB.78.235301.

[114] V. G. Dubrovskii *et al.*, "Role of nonlinear effects in nanowire growth and crystal phase," *Phys. Rev. B - Condens. Matter Mater. Phys.*, vol. 80, no. 20, pp. 1–8, 2009, doi: 10.1103/PhysRevB.80.205305.

[115] J. Johansson *et al.*, "Effects of supersaturation on the crystal structure of gold seeded III-V nanowires," *Cryst. Growth Des.*, vol. 9, no. 2, pp. 766–773, 2009, doi: 10.1021/cg800270q.

[116] M. R. Ramdani, J. C. Harmand, F. Glas, G. Patriarche, and L. Travers, "Arsenic pathways in self-catalyzed growth of GaAs nanowires," *Cryst. Growth Des.*, vol. 13, no. 1, pp. 91–96, 2013, doi: 10.1021/cg301167g.

[117] F. Oehler, A. Cattoni, A. Scaccabarozzi, G. Patriarche, F. Glas, and J. C. Harmand, "Measuring and Modeling the Growth Dynamics of Self-Catalyzed GaP Nanowire Arrays," *Nano Lett.*, vol. 18, no. 2, pp. 701–708, 2018, doi: 10.1021/acs.nanolett.7b03695.

[118] V. G. Dubrovskii, "Theory of MBE Growth of Nanowires on Reflecting Substrates," *Nanomaterials*, vol. 12, no. 2, 2022, doi: 10.3390/nano12020253.

[119] A. Bardas and D. V. Averin, "Electron transport in mesoscopic disordered superconductor-normal-metal-superconductor junctions," *Phys. Rev. B - Condens. Matter Mater. Phys.*, vol. 56, no. 14, pp. R8518–R8521, 1997, doi: 10.1103/PhysRevB.56.R8518.

[120] G. Grosso and G. P. Parravicini, Solid State Physics (Academic Press, 2000).

[121] J. Zhi et al., "Coexistence of induced superconductivity and quantum Hall states in InSb nanosheets," *Phys. Rev. B*, vol. 99, no. 24, pp. 1–8, 2019, doi: 10.1103/PhysRevB.99.245302.

[122] F. Rohlfing et al., "Doppler shift in Andreev reflection from a moving superconducting condensate in Nb/InAs Josephson junctions," *Phys. Rev. B - Condens. Matter Mater. Phys.*, vol. 80, no. 22, pp. 10–13, 2009, doi: 10.1103/PhysRevB.80.220507.

[123] M. Amado et al., "Electrostatic tailoring of magnetic interference in quantum point contact ballistic Josephson junctions," *Phys. Rev. B - Condens. Matter Mater. Phys.*, vol. 87, no. 13, pp. 1–5, 2013, doi: 10.1103/PhysRevB.87.134506.

[124] H. Y. Günel et al., "Crossover from josephson effect to single interface andreev reflection in asymmetric superconductor/nanowire junctions," *Nano Lett.*, vol. 14, no. 9, pp. 4977–4981, 2014, doi: 10.1021/nl501350v.

[125] S. Guiducci et al., "Full electrostatic control of quantum interference in an extended trenched Josephson junction," *Phys. Rev. B*, vol. 99, no. 23, p. 235419, 2019, doi: 10.1103/PhysRevB.99.235419.

[126] S. Guiducci, M. Carrega, G. Biasiol, L. Sorba, F. Beltram, and S. Heun, "Toward Quantum Hall Effect in a Josephson Junction," *Phys. Status Solidi - Rapid Res. Lett.*, vol. 13, no. 1, pp. 13–17, 2019, doi: 10.1002/pssr.201800222.

[127] M. Carrega et al., "Investigation of InAs–based devices for topological applications," no. September, p. 144, 2019, doi: 10.1117/12.2527754.

[128] J. Zhi et al., "Supercurrent and Multiple Andreev Reflections in InSb Nanosheet SNS Junctions," *Phys. Status Solidi Basic Res.*, vol. 256, no. 6, pp. 1–5, 2019, doi: 10.1002/pssb.201800538.

[129] G.H. Lee and H.J. Lee, "Proximity coupling in superconductor-graphene heterostructures," *Rep. Prog. Phys.* 81, 056502, 2018.

[130] L. Banszerus *et al.*, "Minigap and Andreev bound states in ballistic graphene," 2020, [Online]. Available: http://arxiv.org/abs/2011.11471.

[131] J. K. Freericks, A. N. Tahvildar-Zadeh, and B. K. Nikolić, "Use of a generalized thouless energy in describing transport properties of Josephson junctions," *IEEE Trans. Appl. Supercond.*, vol. 15, no. 2 PART I, pp. 896–899, 2005, doi: 10.1109/TASC.2005.850107.

[132] K. K. Likharev, "PIIS0896627311008725.pdf," vol. 51, no. 1, 1979.

[133] J. Heida, B. van Wees, T. Klapwijk, and G. Borghs, "Nonlocal supercurrent in mesoscopic Josephson junctions," *Phys. Rev. B - Condens. Matter Mater. Phys.*, vol. 57, no. 10, pp. R5618–R5621, 1998, doi: 10.1103/PhysRevB.57.R5618.

[134] N. H. Kim, B. K. Kim, H. S. Kim, and Y. J. Doh, "Fabrication and characterization of PbIn-Au-PbIn superconducting junctions," *Prog. Supercond. Cryog.*, vol. 18, no. 4, pp. 5–8, 2016, doi: 10.9714/psac.2016.18.4.005.

[135] V. Barzykin and A. M. Zagoskin, "Coherent transport and nonlocality in mesoscopic SNS junctions: Anomalous magnetic interference patterns," *Superlattices Microstruct.*, vol. 25, no. 5, pp. 797–807, 1999, doi: 10.1006/spmi.1999.0731.

[136] D. E. Sheehy and A. M. Zagoskin, "Theory of anomalous magnetic interference pattern in mesoscopic superconducting/normal/superconducting Josephson junctions," *Phys. Rev. B - Condens. Matter Mater. Phys.*, vol. 68, no. 14, pp. 1–6, 2003, doi: 10.1103/PhysRevB.68.144514.

[137] J. C. Cuevas, J. Hammer, J. Kopu, J. K. Viljas, and M. Eschrig, "Proximity effect and multiple Andreev reflections in diffusive superconductor-normal-metal-superconductor junctions," *Phys. Rev. B - Condens. Matter Mater. Phys.*, vol. 73, no. 18, pp. 1–6, 2006, doi: 10.1103/PhysRevB.73.184505.

[138] J. C. Cuevas and F. S. Bergeret, "Magnetic Interference Patterns and Vortices in Diffusive SNS Junctions," *Phys. Rev. Lett.* 99, 217002 ,2007.

[139] F. S. Bergeret and J. C. Cuevas, "The vortex state and Josephson critical current of a diffusive SNS junction," *J. Low Temp. Phys.*, vol. 153, no. 5–6, pp. 304–324, 2008, doi: 10.1007/s10909-008-9826-2.

[140] F. Carillo *et al.*, "Relevant energy scale in hybrid mesoscopic Josephson junctions," *Phys. Rev. B - Condens. Matter Mater. Phys.*, vol. 78, no. 5, pp. 8–11, 2008, doi: 10.1103/PhysRevB.78.052506.

[141] F. Chiodi *et al.*, "Geometry-related magnetic interference patterns in long SNS Josephson junctions," *Phys. Rev. B - Condens. Matter Mater. Phys.*, vol. 86, no. 6, pp. 1–5, 2012, doi: 10.1103/PhysRevB.86.064510.

[142] T. D. Clark, R. J. Prance, and A. D. C. Grassie, "Feasibility of hybrid Josephson field effect transistors," *J. Appl. Phys.*, vol. 51, no. 5, pp. 2736–2743, 1980, doi: 10.1063/1.327935.

[143] A. Chrestin, T. Matsuyama, and U. Merkt, "Critical currents and supercurrent

oscillations in Josephson field-effect transistors," *Phys. Rev. B*, vol. 49, no. 1, pp. 498–504, 1994, doi: 10.1103/PhysRevB.49.498.

[144] T. Akazaki, H. Takayanagi, J. Nitta, and T. Enoki, "A Josephson field effect transistor using an InAs-inserted-channel In 0.52Al0.48As/In0.53Ga0.47As inverted modulation-doped structure," *Appl. Phys. Lett.*, p. 418, 1995, doi: 10.1063/1.116704.

[145] E. V. Bezuglyi, E. N. Bratus, and V. S. Shumeiko, "Resonant subgap current transport in Josephson field effect transistor," *Phys. Rev. B*, vol. 95, no. 1, pp. 1–10, 2017, doi: 10.1103/PhysRevB.95.014522.

[146] F. Wen, J. Shabani, and E. Tutuc, "Josephson Junction Field-Effect Transistors for Boolean Logic Cryogenic Applications," *IEEE Trans. Electron Devices*, vol. 66, no. 12, pp. 5367–5374, 2019, doi: 10.1109/TED.2019.2951634.

[147] G. E. Blonder, M. Tinkham, and T. M. Klapwijk, "Transition from metallic to tunnelling regimes in superconducting microconstrictions: Excess current, charge imbalance, and supercurrent conversion," *Phys. Rev. B,* 25, 4515–4532 , 1982.

[148] T. M. Klapwijk, G. E. Blonder, and M. Tinkham, "Explanation of subharmonic energy gap structure in superconducting contacts," *Phys. B+C*, vol. 109–110, no. C, pp. 1657–1664, 1982, doi: 10.1016/0378-4363(82)90189-9.

[149] M. Octavio, M. Tinkham, G. E. Blonder, and T. M. Klapwijk, "Subharmonic energy-gap structure in superconducting constrictions," *Phys. Rev. B*, vol. 27, no. 11, pp. 6739–6746, 1983, doi: 10.1103/PhysRevB.27.6739.

[150] K. Flensberg, J. B. Hansen, and M. Octavio, "Subharmonic energy-gap structure in superconducting weak links," *Phys. Rev. B*, vol. 38, no. 13, pp. 8707–8711, 1988, doi: 10.1103/PhysRevB.38.8707.

[151] K. Gharavi, G. W. Holloway, R. R. LaPierre, and J. Baugh, "Nb/InAs nanowire proximity junctions from Josephson to quantum dot regimes," *Nanotechnology*, vol. 28, no. 8, 2017, doi: 10.1088/1361-6528/aa5643.

[152] M. Kjaergaard *et al.*, "Transparent Semiconductor-Superconductor Interface and Induced Gap in an Epitaxial Heterostructure Josephson Junction," *Phys. Rev. Appl.*, vol. 7, no. 3, pp. 1–9, 2017, doi: 10.1103/PhysRevApplied.7.034029.

[153] S. Heedt *et al.*, "Shadow-wall lithography of ballistic superconductor–semiconductor quantum devices," *Nat. Commun.*, vol. 12, no. 1, pp. 1–9, 2021, doi: 10.1038/s41467-021-25100-w.

[154] The next mode in the fit, the 41st mode, has Tr = 0.15 and thus does not contribute to the transport.

[155] A. M. Marsh, D. A. Williams, and H. Ahmed, "Supercurrent transport through a high-mobility two-dimensional electron gas," *Phys. Rev. B*, vol. 50, no. 11, pp. 8118–8121, 1994, doi: 10.1103/PhysRevB.50.8118.

[156] A. C. C. Drachmann *et al.*, "Proximity Effect Transfer from NbTi into a Semiconductor Heterostructure via Epitaxial Aluminum," *Nano Lett.*, vol. 17, no. 2, pp. 1200–1203,

2017, doi: 10.1021/acs.nanolett.6b04964.

[157]   G. W. Webb, F. Marsiglio, and J. E. Hirsch, "Superconductivity in the elements, alloys and simple compounds," *Phys. C Supercond. its Appl.*, vol. 514, pp. 17–27, 2015, doi: 10.1016/j.physc.2015.02.037.

[158]   J. Rumble, ed., CRC Handbook of Chemistry and Physics, 101st ed. (CRC Press, 2020).

[159]   B. Aminov, A. Golubov, and M. Y. Kupriyanov, "Quasiparticle current in ballistic constrictions with finite transparencies of interfaces," *Phys. Rev. B - Condens. Matter Mater. Phys.*, vol. 53, no. 1, pp. 365–373, 1996, doi: 10.1103/PhysRevB.53.365.

[160]   C. Baumgartner *et al.*, "Josephson Inductance as a Probe for Highly Ballistic Semiconductor-Superconductor Weak Links," *Phys. Rev. Lett.*, vol. 126, no. 3, pp. 1–6, 2021, doi: 10.1103/PhysRevLett.126.037001.

[161]   M. Tinkham, Introduction to superconductivity (McGraw-Hill, 1996).

[162]   V. Ambegaokar and A. Baratoff, "Tunneling between superconductors," *Phys. Rev. Lett.*, vol. 11, no. 2, p. 104, 1963, doi: 10.1103/PhysRevLett.11.104.

[163]   I. O. Kulik and A. N. Omel'yanchuk, "Contribution to the microscopic theory of the Josephson effect in superconducting bridges," *JETP Lett.* 21, 96–97 ,1975.

[164]   C. W. J. Beenakker, "Universal Limit of Critical-Current Fluctuations in Mesoscopic Josephson Junctions," *Phys. Rev. Lett.*, vol. 67, no. 27, pp. 3836–3839, 1991.

[165]   W. Mayer, J. Yuan, K. S. Wickramasinghe, T. Nguyen, M. C. Dartiailh, and J. Shabani, "Superconducting proximity effect in epitaxial Al-InAs heterostructures," *Appl. Phys. Lett.*, vol. 114, no. 10, 2019, doi: 10.1063/1.5067363.

[166]   Y. J. Doh, J. A. Van Dam, A. L. Roest, E. P. A. M. Bakkers, L. P. Kouwenhoven, and S. De Franceschi, "Applied physics: Tunable supercurrent through semiconductor nanowires," *Science (80-.).*, vol. 309, no. 5732, pp. 272–275, 2005, doi: 10.1126/science.1113523.

[167   J. Xiang, A. Vidan, M. Tinkham, R. M. Westervelt, and C. M. Lieber, "Ge/si nanowire mesoscopic josephson junctions," *Nat. Nanotechnol.*, vol. 1, no. 3, pp. 208–213, 2006, doi: 10.1038/nnano.2006.140.